Titre: Title:	Experimental Study of Low Density Micro Jets in Crossflow for Hydrogen Injection in Gas Turbines
Auteur: Author:	Gabriel Dodier
Date:	2024
Type:	Mémoire ou thèse / Dissertation or Thesis
Référence: Citation:	Dodier, G. (2024). Experimental Study of Low Density Micro Jets in Crossflow for Hydrogen Injection in Gas Turbines [Mémoire de maîtrise, Polytechnique Montréal]. PolyPublie. https://publications.polymtl.ca/61617/

URL de PolyPublie: PolyPublie URL:	https://publications.polymtl.ca/61617/
Directeurs de recherche: Advisors:	Étienne Robert
Programme: Program:	Génie mécanique

POLYTECHNIQUE MONTRÉAL
affiliée à l'Université de Montréal

Experimental Study of Low Density Micro Jets in Crossflow for Hydrogen Injection in Gas Turbines

GABRIEL DODIER
Département de génie mécanique

Mémoire présenté en vue de l'obtention du diplôme de *Maîtrise ès sciences appliquées*
Génie mécanique

Décembre 2024

POLYTECHNIQUE MONTRÉAL
affiliée à l'Université de Montréal

Ce mémoire intitulé :

Experimental Study of Low Density Micro Jets in Crossflow for Hydrogen Injection in Gas Turbines

présenté par **Gabriel DODIER**
en vue de l'obtention du diplôme de *Maîtrise ès sciences appliquées*
a été dûment accepté par le jury d'examen constitué de :

Bianca VIGGIANO, présidente
Etienne ROBERT, membre et directeur de recherche
Ekow ESSEL, membre

DEDICATION

À Léa et mes parents,
Merci . . .

ACKNOWLEDGEMENTS

First and foremost, I am sincerely thankful to my research supervisor, Professor Etienne Robert, for his valuable guidance during my studies. He not only provided a truly interesting research project with real industrial applications, but also trusted me with considerable freedom to explore solutions and ideas. This project would not have been possible without his knowledge and generous support.

I extend my deepest thanks to Philippe Versailles, PhD and Minchao Han, PhD who spent time with me in the lab, teaching me without hesitation, discussing ideas and reviewing my work in the most constructive and helpful ways. I am truly grateful for these two years of learning experience alongside world-caliber experts.

I am also grateful to everyone from the micromix NSERC alliance project; Professor Swetaprovo Chaudhuri (University of Toronto), Professor Jeffrey Bergthorson (McGill), Gilles Bourques, PhD (McGill), Professor Bruno Savard (PolyMtl) for always asking thought-provoking questions and organizing our biweekly meetings and workshops from which I learned a great deal. This extends to Patrizio Vena, PhD and his colleagues at NRC Canada and Marc Furi, PhD at Siemens Energy, for inviting our team to an amazing lab visit, sponsoring this research and sharing their insights.

I also express my gratitude to Professor Jérôme Vettel for allowing me to spend so much time in his lab, sharing his equipment and answering my not always smart questions.

To every colleague who became friends at the LEMUR lab; thank you for creating such a fun working atmosphere and for our crazy discussions around coffee.

Je remercie mes parents pour leur support inconditionnel, mes frères et ma soeur pour les weekends passés ensemble qui permettent de décrocher.

Finalement, je remercie Léa de tout mon coeur pour son soutien et sa patience depuis tout ce temps, Merci!

RÉSUMÉ

L'hydrogène se présente comme un carburant alternatif convaincant pour les systèmes de turbines à gaz en raison de sa combustion sans carbone. Cela s'aligne avec les efforts mondiaux de décarbonation de l'énergie. Plusieurs géométries de brûleurs à hydrogène développés récemment utilisent des micro-jets submillimétriques pour injecter ce carburant dans un flux d'oxydant transverse. Cette configuration «micromix» permet non seulement de réduire les probabilités de retour de flamme, mais bénéficie du mélange intense causé par de multiples jets en écoulement transverses. Cela réduit le temps de résidence du mélange à hautes températures, aidant à réduire les émissions nocives de NO_x.

Les jets en écoulement transverse provoquent des structures d'écoulement complexes et instationnaires. Les études antérieures sur ce type d'écoulement se concentrent sur un jet unique, et non sur l'injection de gaz peu dense à travers plusieurs microjets en série. Pour mieux comprendre cette technique novatrice d'injection d'hydrogène, ce projet de recherche utilise la vélocimétrie par images de particules pour obtenir des champs de vitesse et de concentration de particules ensemencées sur trois plans de mesure. La campagne expérimentale utilise un banc d'essai à écoulement transverse de vitesse $U_\infty = 2$ m/s, avec un à huit jets de 0.8 mm de diamètre, caractérisé par un nombre de Reynolds entre $Re_j = 30$ et 300. L'objectif principal est d'étudier l'effet de la géométrie et de la vitesse des jets sur l'écoulement. À cette fin, des enregistrements à une fréquence d'acquisition de 10 kHz sont effectués avec des vitesses de jets entre 5 et 50 m/s, un ratio de densité de $S = 0.14$ et un espacement adimensionnel entre les jets de $l/d = 1.5$, 2.12 et 5.25.

Les résultats principaux montrent que de fortes instabilités sont générées dans l'écoulement lorsque la vitesse des jets augmente. Des images dans le plan transversal montrent également l'évolution de paires de vortex contrarotatifs (CVP) qui interagissent ensemble, et s'étirent verticalement quand l'espacement est réduit entre les jets. Pour un rapport de densité fixe, les trajectoires de micro-jets en série sont bien modélisées avec le rapport de vitesse R. Les champs de vecteurs PIV moyens montrent également une zone de recirculation derrière les jets. Cette zone à faible vitesse s'agrandit pour des séries de jets plus rapprochées. La position des instabilités est aussi suivie dans le temps, permettant une analyse fréquentielle. Les jets uniques ont une fréquence d'oscillation plus basse que les séries de jets à espacement réduit, qui se mélangent et décomposent les structures cohérentes. Les séries de jets compactes défavorisent les modes globalement instables, ce qui améliore le mélange, mais ils créent une zone de recirculation défavorable dans les chambres à combustion des turbines à gaz.

ABSTRACT

Hydrogen emerges as a compelling alternative fuel for power generation in gas turbine systems due to its carbon free combustion, aligning with global efforts to reduce fossil fuel consumption. Recently developed burner geometries often employ sub millimeter diameter jets in crossflow to inject gaseous hydrogen into the oxidizer stream. This "Micromix" configuration not only aids in reducing the likelihood of flame flashback, but also benefits from the intense mixing caused by multiple jets in crossflow. This lowers the mixture residence time at high temperatures, helping to reduce harmful NO_x emissions.

The jet in crossflow (JICF) configuration plays an important role in the design of Micromix combustors and causes complex flow structures downstream of the injection point. Studies of jets in crossflow mostly focus on single jet geometries and not on low density gas injection through multiple micro jets. To better understand this novel Micromix fuel injection technique, the present research utilizes high-speed particle image velocimetry (PIV) and Mie scattering based image analysis to obtain velocity and mixing fields over three measuring planes. The experimental campaign takes place in a 50 by 50 mm square cross-section channel, featuring one to eight jets of 0.8 mm diameter, enabling a crossflow Reynolds number of $Re_\infty = 7000$ and jet Reynolds number from $Re_j = 15$ to 300. The main objective is to investigate the effect of jet velocity and jet array spacing on the flow field. To this end, 10 kHz recordings of the particle seeded flow are taken with different jet velocities, a low density ratio of 0.14 and jet-to-jet spacing of $l = 1.5$, 2.12 and 5.25.

Key results show that as the jet-to-crossflow momentum flux ratio increases, shear layer instabilities start to develop and increase in size. Measurements in the transverse plane also show the evolution of counter-rotating vortex pairs (CVPs) interacting together, which grow in size as the jet spacing is reduced and are stretched vertically compared to single JICF recordings. For a fixed low density ratio of $S = 0.14$, modeling micro jet array trajectories is best done with R scaling. The time-averaged PIV vector fields also show a recirculation zone behind the array of jets. This low velocity flow reversal zone increases in size with higher jet-to-crossflow velocity ratios and more closely spaced arrays. The shear layer position is tracked in time, enabling frequency analysis and comparison between test cases. Single low density jets show lower near-field shear layer oscillation frequency compared to closely spaced arrays that mix together and break coherent structures easily. Tightly spaced arrays of JICF help the shear layer vortices to escape globally unstable modes to improve mixing, but also create a strong recirculation zone, which is detrimental in gas turbine combustors.

TABLE OF CONTENTS

LIST OF TABLES

LIST OF FIGURES

LIST OF SYMBOLS AND ACRONYMS

Acronyms

CVP	Counter rotating vortex pair
CO_2	Carbon dioxide
DNS	Direct numerical simulation
FWHM	Full width half maximum
He	Helium
H_2	Hydrogen
JICF	Jet in crossflow
LDA	Laser doppler anemometer
LIF	Laser induced fluorescence
Nd:YLF	Neodymium-doped yttrium lithium fluoride
NO_x	Nitrogen oxides
NTP	Normal temperature and pressure
N_2	Nitrogen
O_2	Oxygen
POD	Proper Orthogonal decomposition
PIV	Particle image velocimetry
STP	Standard temperature and pressure

Symbols

d	Jet nozzle diameter
d_p	Diameter of seeding particles
Δy	Spread of the JICF along the vertical plane
I	Pixel intensity
J	Jet to crossflow momentum flux ratio
k	Turbulent kinetic energy
l	Center-to-center spacing between jets
λ	Wavelength of the laser
μ	Dynamic viscosity
ν	Kinematic viscosity
R	Jet to crossflow velocity ratio
R_e	Equivalent jet to crossflow velocity ratio
Re_j	Reynolds number based on the jet diameter
Re_∞	Reynolds number based on the crossflow rig geometry
S	Jet to crossflow density ratio
Sk	Stokes number
St	Strouhal number
t	Time
τ_p	Particle response time in the flow
U_∞	Crossflow velocity
U_j	Jet velocity
$\mathbf{U} = (U, V, W)$	Velocity field
$\mathbf{u'} = (u', v', w')$	Velocity fluctuation field
$\mathbf{x} = (x, y, z)$	Spatial cartesian coordinates
$\xi = (\xi, \eta, \zeta)$	Spatial natural coordinates along the jet centerline
δt	Time interval between two laser pulses
η	Kolmogorov scale
ρ_j	Jet Density
ρ_∞	Crossflow Density

Mathematical Operators

$\bar{x}$	Average (mean) of x
$\|x\|$	Norm of x
$\mathcal{F}$	Fourier transform
$\cdot$	Scalar product
∇	Nabla operator (gradient)
∂	Partial derivative
$\int$	Integral
$\sum$	Summation
$\prod$	Product

LIST OF APPENDICES

CHAPTER 1 INTRODUCTION

1.1 The energy landscape and hydrogen as a fuel

Fossil fuels have played a key role in driving economic growth and enhancing quality of life across the globe. Yet their extensive use have led to significant increase in pollutant emissions, such as CO_2, NO_x and fine particulate matter, thus posing serious health and environmental challenges [1, 2]. In figures 1.1a and 1.1b, this historical relationship is illustrated and shows how an increase in energy consumption correlates with environmental impact and economic growth over the years in Canada [3–5].

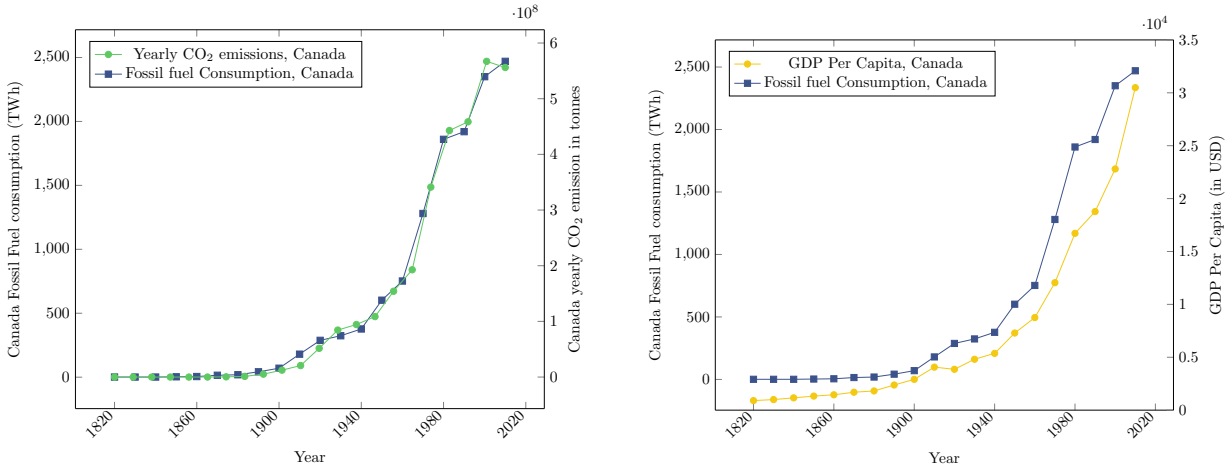

(a) (b)

Figure 1.1 Canadian annual fossil fuel consumption in TWh compared to (a) yearly Canadian CO_2 emissions in tonnes and (b) Canadian Gross Domestic Product (GDP) per capita in USD [3–5]

To face these environmental challenges, engineers and scientists are looking at alternative energy carriers. Hydrogen (H_2) is increasingly viewed as a promising carbon free replacement to fossil fuels, especially in hard to abate industrial sectors and for off-grid power production [6].

Hydrogen is the most abundant element in the universe. It is a colorless and odorless gas, characterized by its low density and high diffusivity at normal temperature and pressure (NTP). Despite its low volumetric energy density of around 11 MJ/m^3, hydrogen possesses high energy density by weight at 142 MJ/kg, which is significantly higher than traditional fossil fuels at around 40-50 MJ/kg.

Hydrogen can be produced through various methods, leading to different types classified by

their production processes and associated emissions [7]. The main categories are gray, blue, and green hydrogen. In general, gray hydrogen is produced from natural gas through steam methane reforming (SMR). Blue hydrogen also comes from SMR, but with carbon capture and storage technologies (CCS) to offset the emissions produced. Green hydrogen is typically produced by electrolysis of water using renewable electricity sources, making it the cleanest option.

In Canada, gray hydrogen is currently the more prominent type due to the country's vast natural gas resources. However, there is growing interest and investment in green hydrogen, mainly by leveraging Canada's abundant renewable energy resources, such as hydropower. The Canadian government branch for Natural Resources is leaning on the hydrogen economy and expects $50B in domestic revenues benefits by 2050 [8].

A critical way in which H_2 can contribute to reducing carbon emissions is power production and storage. Converting electrical energy into hydrogen fuel can help mitigate the intermittent nature of wind and solar power, while enhancing energy reserves and security. In such a scenario, a gas turbine is coupled to an electrolyzer powered by renewable electricity sources. The hydrogen produced from water is stored, and during periods of high demand, the gas turbine burns H_2 to generate electricity. Existing natural gas (NG) power plants can be adapted to run on hydrogen, either blended with NG or as a pure fuel. This fuel flexibility facilitates the integration of hydrogen into current energy infrastructure. This power-to-power design idea is shown in Figure 1.2 [9].

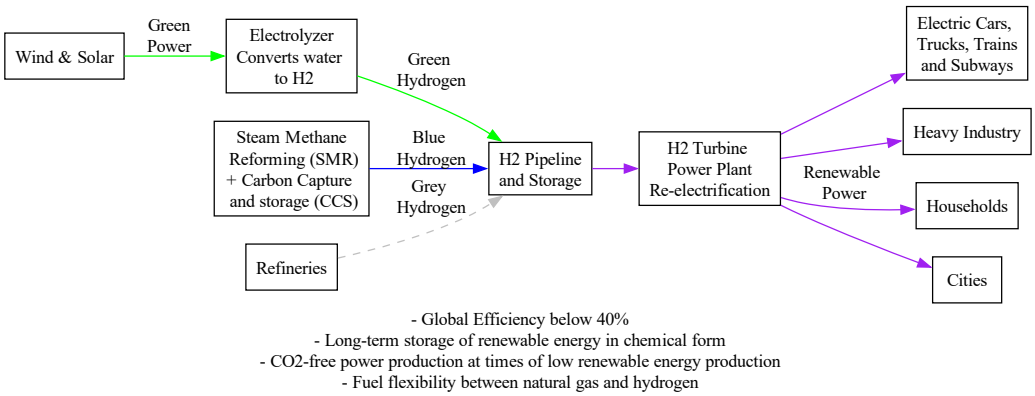

Figure 1.2 Hydrogen power-to-power proposed by Siemens Energy [9]

The thermodynamic properties of hydrogen and classical hydrocarbons, such as methane and gasoline, exhibit significant differences [10] that are shown in table 1.1. Hydrogen has a

much lower molecular mass of 2.016 g/mole, and a much lower density at standard pressure and temperature, when compared to methane and gasoline. This results in a much higher diffusivity coefficient in air that facilitates faster mixing. While this characteristic can be advantageous for combustion processes, it also creates serious risks of leaks in piping systems and flame flashback, where the flame travels backward into unintended premixing areas. The reactive properties of hydrogen are also notably different to classical fuels [10], as is shown in table 1.2. The heat of combustion of hydrogen is notably higher than that of methane and gasoline, indicating that hydrogen releases more energy per unit mass when burned. Additionally, hydrogen has a higher adiabatic flame temperature of 2318 K when compared to methane at 1963 K and gasoline at 2138 K. This can contribute to increased thermodynamic efficiency in heat engines, but necessitates robust materials to withstand those higher temperatures. Furthermore, hydrogen's broader flammability limits in air (4.0–75.0 vol%) allow it to burn over a wide range of conditions, providing flexibility but also instability and safety challenges [11]. Finally, the minimum energy for ignition in air for hydrogen is 10 times lower than methane and gasoline, highlighting how reactive and dangerous this mixture can be. These differences underscore hydrogen's potential as an energy-dense and carbon free fuel, but also highlighting the need for specialized knowledge, handling and infrastructure compared to legacy hydrocarbon fuels.

Table 1.1 Thermodynamic properties of hydrogen, methane, and gasoline [10]

Properties	**Hydrogen**	**Methane**	**Gasoline**
Molecular mass (g/mole)	2.016	16.043	107
Density of gas at STP (kg/m^3)	0.084	0.651	4.400
Lower heat of combustion (kJ/g)	119.9	50.0	44.5
Higher heat of combustion (kJ/g)	141.9	55.5	48.0
Specific heat (c_p) of STP gas (J/g/K)	14.86	2.22	1.62
Diffusion coefficient in STP air (cm^2/s)	0.61	0.16	0.005

1.2 Hydrogen use in gas turbines

Among energy conversion systems, gas turbines are a key technological area where hydrogen can impact a field historically dominated by fossil fuels. A conventional gas turbine designed for power production is schematized in Figure 1.3. One of the most complex area to design is the combustion chamber, where fuel is added and burned with the compressed air. The current particular interest is on the specific method with which fuel is injected into this

Table 1.2 Combustion properties of hydrogen, methane, and gasoline [10]

Properties	**Hydrogen**	**Methane**	**Gasoline**
Limits of flammability (equivalence ratio)	0.1–7.1	0.53–1.7	0.7–3.8
Limits of flammability in air (vol%)	4.0–75.0	5.3–15.0	1.0–7.6
Minimum energy for ignition in air (mJ)	0.02	0.29	0.24
Adiabatic flame temperature (K)	2254	1963	2138
Laminar flame speed in STP air (cm/s)	295	40	41

device. Understanding fuel injection behavior is crucial, as it plays a major role in shaping the flame behavior and the pollutant emission profile of the gas turbine.

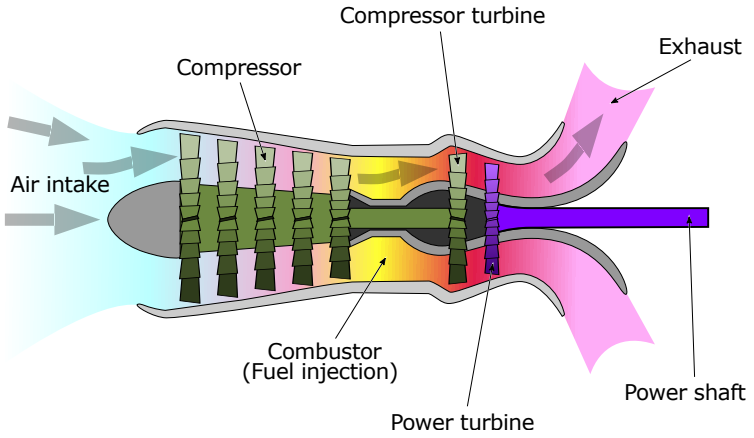

Figure 1.3 Diagram of a gas turbine designed for power production, adapted from [12] under CC

In traditional gas turbines, gaseous fuel, such as methane, is injected within a premixing chamber where it blends with the oxidizer before ignition. This approach, known as lean premixed combustion (LPC), is used in Dry Low Emission (DLE) systems. Premixed DLE systems enable oxygen rich homogeneous mixture composition at the flame front, which allows for lower flame temperatures to reduces thermal NO_x formation [13]. In contrast, Wet Low Emission (WLE) systems use steam injection to lower the temperature of a non-premixed diffusion flames, reducing the production of NO_x at the cost of weight and part complexity. Nitrogen oxides (NO_x) are harmful emissions composed mainly of NO and NO_2 that contribute to acid rain, smog, fine particulate matter and ground pollution, impacting human health and the environment [14]. High temperatures (1800 K and above) lead to the dissociation of the nitrogen in the air, forming NO through the Zel'dovich mechanism, which can subsequently react to form NO_2.

A premixed flame, like that used in LPC systems, propagates as a wave within the mixture of fuel and oxidizer when ignited, stabilizing where to flame speed is in equilibrium with the bulk flow speed [15]. In an ideal laminar case, the burning velocity or "laminar flame speed" S_L, is defined as the velocity of the unburned gases moving into the combustion wave front [16]. In comparison, non-premixed flames form from the diffusion of fuel and oxidizer, and are positioned where stoichiometric conditions are met [15].

Premixed combustion suffers from unwanted risks of flame flashback, whereas non-premixed diffusion combustion does not. Flashback refers to the rapid propagation of the flame into a region upstream of the combustion chamber where the reactants mix, but not intended to sustain flames [17]. This phenomenon can damage components not designed to withstand high temperatures and causes service outages that reducing power reliability. Even if the average bulk flow velocity exceeds the mixture's flame speed, flashback can occur because of complex mechanisms such as vortex breakdown, boundary layer propagation and instabilities [17]. Thus, when considering hydrogen as a replacement to natural gas, several challenges arise for its use within traditional premixed combustor designs. With a laminar flame speed of nearly 3 m/s, compared to 0.4 m/s for methane, Hydrogen shows an order of magnitude higher flashback potential due to its higher reaction rates and thermal diffusivity in air [16]. The broader flammability limits of H_2 can also increase chances of flashback under very lean or rich conditions. Adiabatic flame temperature of almost 300 degrees higher for H_2 also significantly increases thermal NO_x production in the system. This explains why hydrogen cannot be injected directly into existing gas turbine systems while expecting similar performance, NO_x emissions and flame stability characteristics without modifications [18].

To this end, hydrogen micromix injection technology gained recent attention as a promising approach to ensure reliable, flashback-resistant combustion with acceptable pollutant emissions. Micromix injection mixes the fuel and oxidizer at the submillimeter level to create hundreds of small diffusion like flames. This intense fuel-air mixing is achieved using multiple miniaturized jets in crossflow (JICF) to achieve greater turbulence, more uniform fuel-air distributions and lower residence time spent at high temperatures, as an attempt to reduce NOx formation.

1.3 Hydrogen Micromix burners

Hydrogen micromix technology aims to achieve low NO_x in lean DLE combustion systems. To accomplish this, it shifts from conventional premixed burner geometries and their associated lower flame temperatures but high risk of hydrogen flame flashback, to micromix burners with many small diffusion flames. Although diffusion flames are typically associated with

high local temperatures that increase NO_x production, micromix burners mitigate this with arrays of micro jets in crossflow, as will be discussed in this section.

Recent work on micromix hydrogen burner design includes a modified 370 kW gas turbine developed at Aachen university [19–22], shown in Figure 1.4. This design demonstrated ultra low sub-10 ppm NO_x emissions using 1600 individual 0.84 mm diameter JICF injectors in the circular combustor setup.

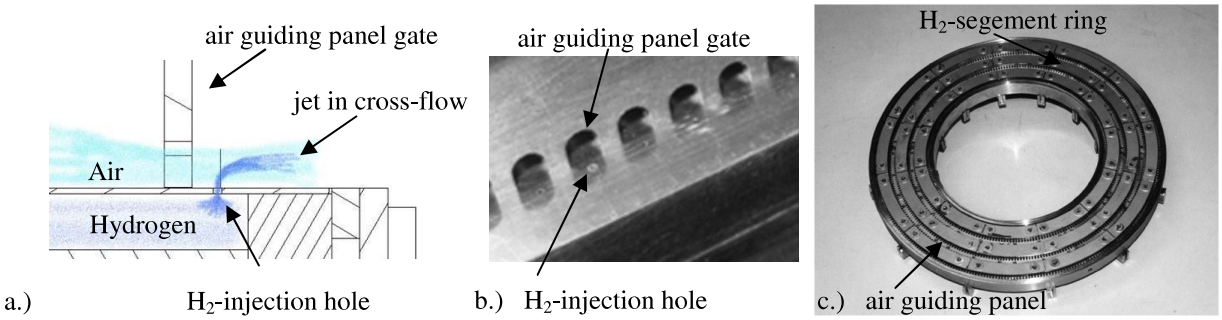

Figure 1.4 Schematic of the micromix burner geometry designed at Aachen university, adapted with permission [22]

Hydrogen burners are also developed at Sherbrooke University using 3D printed micromix injector designs for aerospace gas turbine applications [23]. This new geometry is visible in Figure 1.5, where dozens of small as 0.25 mm 3D printed holes are seen delivering various fuel types, showing the behavior of multiple swirling small JICF diffusion flames.

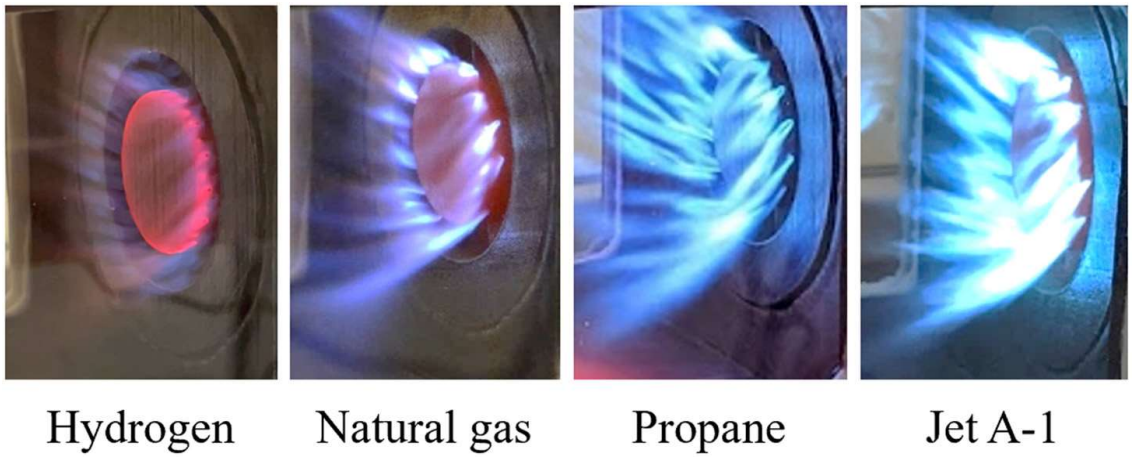

Figure 1.5 Flame behavior for many fuels with the micromix burner developed at Sherbrooke university, reproduced with permission [23]

Another key micromix design was prototyped and investigated by NASA in 2003 to study

premixed lean hydrogen flames [24]. This burner aims to use hydrogen as a fuel for aircraft gas turbine systems. It is shown in Figure 1.6, highlighting the 0.5 mm micro jet in crossflow arrangement and the pale blue hydrogen flame. This burner geometry sparked significant interest in the combustion research community and has been studied to understand the complex flame structure and stabilization mechanisms [25].

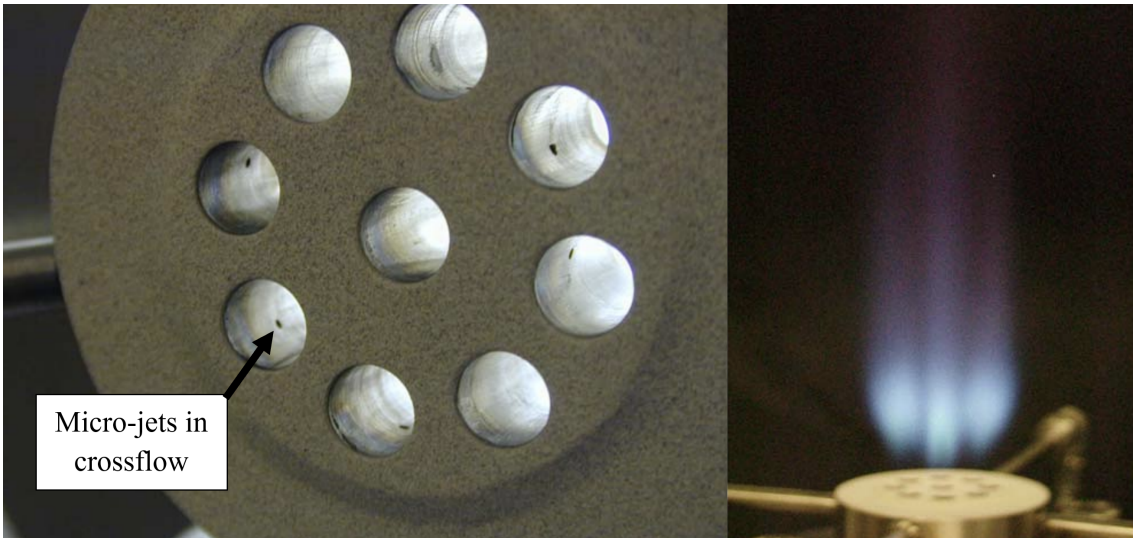

Figure 1.6 NASA Lean Premixed Hydrogen Burner [24], publicly accessible as a service by the U.S. Department of Energy

Despite the advancements in micromix combustion technology, fundamental knowledge of its underlying mechanisms remains incomplete due to its novelty and complexity. Our study addresses this knowledge gap by focusing on the fundamental fluid dynamics of hydrogen jets in crossflow under cold flow conditions. By conducting experiments without combustion, we can isolate the effects of hydrogen's low density on jet behavior, stability, and mixing characteristics. Since industrial gas turbine geometries are complex, it is crucial to decompose these configurations into more fundamental cases to better understand the effects of non-dimensional parameters. This approach allows us to study these parameters and develop insights that will later on be useful for optimizing micromix injector designs in practical applications.

The novel hydrogen micromix burner designs presented herein have a common theme of employing many micro jets injected into a crossflow. Understanding the behavior of these low density jets in crossflow is important to design hydrogen gas turbine fuel injectors. To this end, a thorough literature review of jets in crossflow is presented in chapter 2.

1.4 Global research objectives

This master's thesis focuses on the non-reactive study of multiple low density micro jets in crossflow. The global research objectives are as follows. First, develop an experimental rig to record interactions of low density micro-jet arrays with an air crossflow at a high temporal resolution. Second, characterize the effect of jet-to-crossflow velocity ratio on the flow behavior and mixing field. Third, understand the effect of multiple jet array configurations on the flow field.

1.5 Thesis outline

This master's thesis begins with a comprehensive literature review on single jets in crossflow and jet arrays in crossflow, showing key past experimental studies and current knowledge gaps. Next, the methodology describes the design of the experimental rig and custom-built components. It also details the use of high-speed Particle Image Velocimetry (PIV) system, calibration steps, data acquisition, and processing techniques. The results section, contains an analysis of velocity fields and high-speed recordings for various jet configurations and flow conditions, examining jet spread, trajectories, mixing, and oscillatory shear layer dynamics. This section will shortly be published in the form of a scientific paper in the journal "Physics of Fluids". The author's contributions include the literature review, design, experimentation, analysis, and drafting of the manuscript. The initial proof of concept results are shown in Appendix A in the form of preliminary results presented at a national conference presentation. Ongoing research is shown in the following chapter and in Appendix B to help guide future experimental improvements and identify research needs. Finally, the conclusion provides a summary of the experimental findings, current limitations, and recommendations for future research to improve hydrogen micromix combustion technology.

CHAPTER 2 LITERATURE REVIEW

This state-of-the-art review aims to understand the existing body of work on jets in crossflow, determine what information is useful for this hydrogen injection problem, and identify the research gaps linking the scientific literature to this current issue.

2.1 The single jet in crossflow

The jet in crossflow (JICF) configuration is a well-known flow field that has been studied extensively over the last century. It is relevant to many engineering applications, especially because of its improved near field mixing compared to a classical free jet [26]. This flow phenomenon is visible, for instance, in volcanic eruptions, pollutant stream dispersal in rivers, turbine blade cooling systems, flue-gas stacks and fuel injectors. Figure 2.1 illustrates similar frequent occurrences of jets in crossflow.

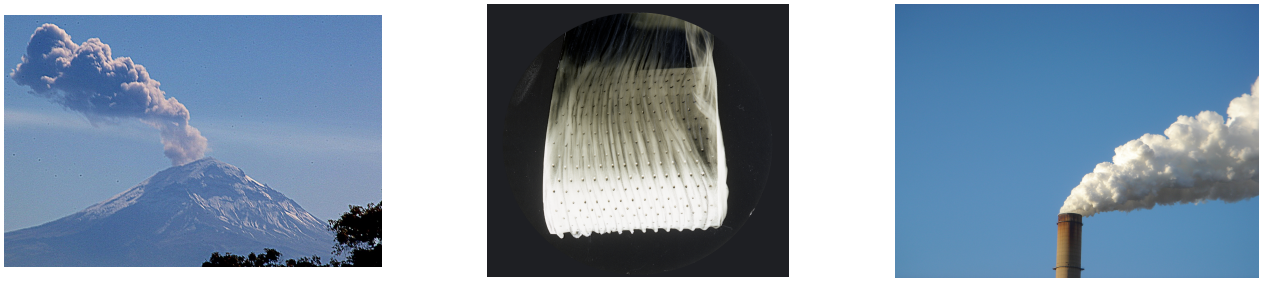

Figure 2.1 Jets in crossflow visible in volcanic eruptions, turbine blade film cooling and chimney gases, reproduced from [27–29] under CC

2.1.1 Main parameters and jet trajectories

Some of the earliest work on JICF can be traced back to the 1930s, where dispersion of coal chimney smoke into the atmosphere and fuel mixing in furnaces was studied to help improve urban air quality [30,31]. In the 1940s, fuel injection in jet engines was investigated using one of the first dedicated laboratory-scale jet in crossflow experimental rig. This NASA research group measured the trajectory of a single air jet issued into a crossflow with a pressure tube rake, while varying the crossflow velocity, jet velocity, jet temperature and jet orifice

shapes [32, 33]. This work employed the velocity ratio R, defined in equation 2.1:

$$R = \frac{U_j}{U_\infty} \tag{2.1}$$

where U_j is the jet velocity and U_∞ is the crossflow velocity. It was shown that R alone is insufficient to predict jet behavior for variable density jet and crossflow [32]. To address this, the density ratio S was introduced to help model the results from these early studies, and is defined in equation 2.2:

$$S = \frac{\rho_j}{\rho_\infty} \tag{2.2}$$

where ρ_j and ρ_∞ denote the jet and crossflow fluid density, respectively.

Exhaustive work was later conducted in 1963 by Keffer and Baines, using smoke visualization and hot-wire anemometer measurements of an air jet issued into an air crossflow [34]. Average velocity profiles were measured along a newly proposed system of axes following the jet centerline, instead of the usual Cartesian system. This natural system of axes is displayed in Figure 2.2, where x is the crossflow streamwise or longitudinal direction, y is the vertical jet direction, z is the lateral or transverse direction, ξ is the jet centerline axis, and finally η and ζ are the orthogonal remaining axes along the curved centerline.

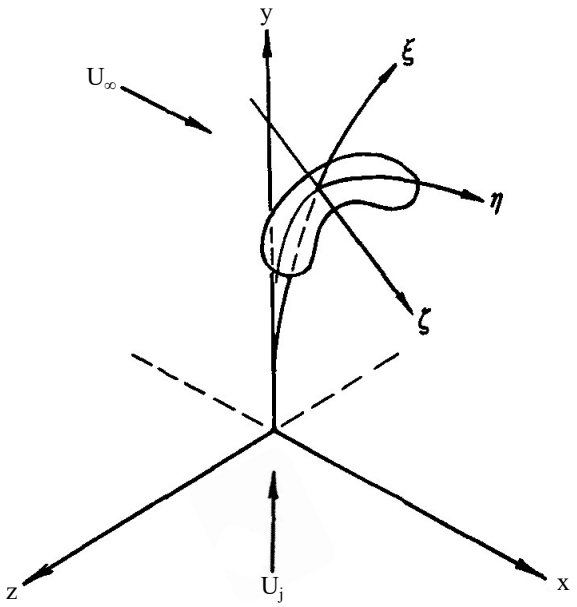

Figure 2.2 Jet in crossflow Cartesian and natural axes system from Keffer and Baines [34], adapted with permission

The velocity profiles along the natural axes are impacted most by the jet-to-crossflow mo-

mentum flux ratio J, defined in equation 2.3:

$$J = SR^2 = \frac{\rho_j U_j^2}{\rho_\infty U_\infty^2} \tag{2.3}$$

This showed that velocity profiles could be better predicted with J for variable density cases. However, these profiles are not always self-similar, unlike the free-jet [34]. This is in part because JICFs behave differently at low velocity ratio, quickly deflecting and curving before entering high into crossflow. Finally, it was shown that, compared to a classical free-jet, the JICF velocity decays faster along its centerline and stronger turbulence is generated [34]. This is caused by the greater entrainment of surrounding fluid causing momentum reduction along the centerline.

Later work by Kamotani and Greber in 1972 demonstrated that the momentum flux ratio J is a better correlation parameter to account for different jet and crossflow temperatures and pressures. This was shown with temperature probe measurements of a heated jet in a cold air crossflow [35]. The mean temperature distribution in cross-sectional planes displayed a kidney-like structure, similar to the counter-rotating vortex pair (CVP) observed in the vorticity field. Also, turbulence intensity $TI = u'_{\text{RMS}}/\bar{u}$ was found to rise with an increase in momentum ratio J [35]. Where u'_{RMS} is the root-mean-square (RMS) of the velocity fluctuations, and $\bar{u}$ is the average velocity.

The TI indicates the relative magnitude of the velocity fluctuations compared to the mean flow by employing the well-known Reynolds decomposition of equation 2.4. This involves expressing the instantaneous velocity vector $\mathbf{U}$ as the sum of its mean components $\bar{\mathbf{u}}$ and the fluctuating components $\mathbf{u}'$. This facilitates turbulent flow analysis by studying the average flow and the turbulent fluctuations independently [36].

$$\mathbf{U} = \bar{\mathbf{u}} + \mathbf{u}' \tag{2.4}$$

In parallel, Margason developed an empirical equation to compare jet paths with each other and with those of previous investigations at the NASA Langley Research Center [37]. This equation takes the power-law form, where A and B are constants in equation 2.5:

$$y = Ax^B \tag{2.5}$$

To help compare other experimental work, the trajectories can be modeled in a universal manner using equivalent velocity ratio [37] defined in equation 2.6:

$$R_e = \sqrt{J} = \sqrt{\frac{\rho_j U_j^2}{\rho_\infty U_\infty^2}} \tag{2.6}$$

Giving the following trajectory equation 2.7 scaled with the equivalent velocity ratio and verified by photographing water vapor smoke added to a compressed air jet in a wind tunnel [37].

$$\frac{y}{R_e d} = A\left(\frac{x}{R_e d}\right)^B \tag{2.7}$$

Where x/d and y/d are the dimensionless streamwise and vertical coordinates, respectively, d is the jet diameter, and A and B are experimental constants to fit the model. Margason provides a compilation of past experimental values [30] of fitting constants in the range of $1.2 < A < 2.6$ and $0.28 < B < 0.34$.

This relationship is plotted in Figure 2.3 for different values of R_e to visualize how y/d changes with respect to x/d and R_e. This Figure shows the clear effect of the momentum flux ratio on the jet centerlines. When the jet has stronger momentum, it penetrates deeper into the crossflow and achieves an asymptotic horizontal trajectory behavior later downstream.

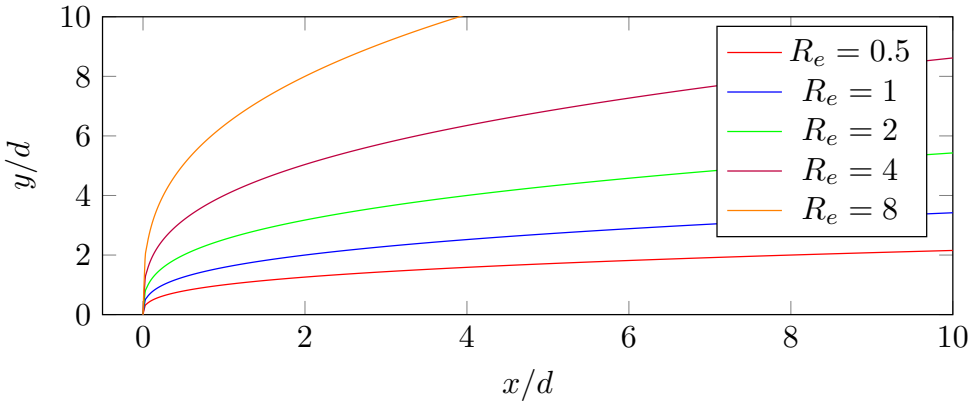

Figure 2.3 Jet in crossflow velocity centerline trajectories for different equivalent velocity ratio R based on Marganson's trajectory model [30].

In this era, there was no distinction yet between the jet concentration, dynamic pressure, and velocity centerlines. Different measurement techniques provided centerlines that were all compared, thus adding to the uncertainty of the empirical trajectory modeling parameters obtained.

Figure 2.4 illustrates the experimental jet centerlines of eight different data sets compared

using Rd scaling [38]. A very large discrepancy is visible between the results, and is attributed to variance is jet outlet profiles, boundary layer thickness and which quantity was used to plot the centerline (velocity magnitude U vs scalar concentration C).

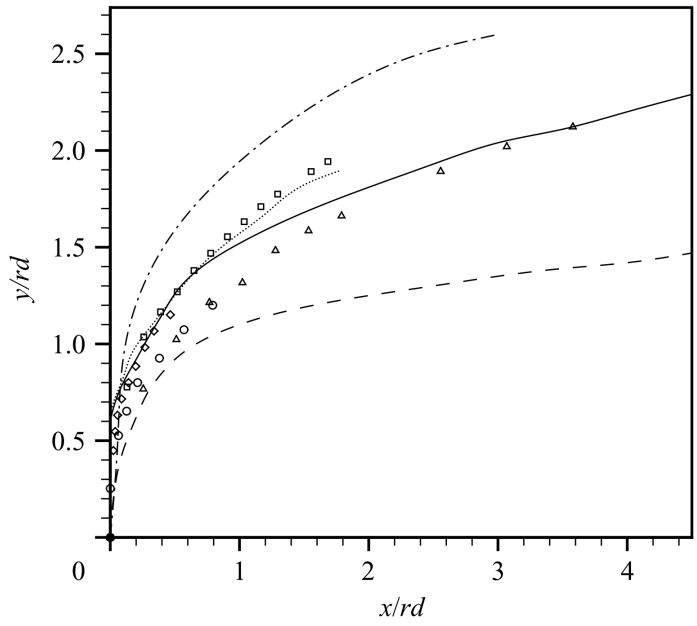

Figure 2.4 Jet trajectories from experimental data scaled by Rd from the review of Muppidi and Mahesh. Velocity ratios are from $R = 3.0$ to $R = 10$ [38], adapted with permission

Even if, as has been noted by Smith & Mungal [39], the trajectory based on maximum local velocity penetrates 5–10% higher into the flow than maximum scalar concentration trajectories, the variance shown in Figure 2.4 is much larger. The trajectories do not collapse unto a single line, showing how Rd scaling is not always sufficient and other parameters may be at play. For instance, a thick boundary layer, having less momentum directly at the jet exit, enables the JICF to penetrate deeper. Similarly, a jet exiting with a quadratic velocity profile, compared to a top hat velocity profile, will have a different momentum distribution and will behave differently. Therefore, a new scaling trajectory model was proposed that takes this idea into account [39]:

$$\frac{y}{Rd} = A' \left(\frac{x}{Rd}\right)^B \left(\frac{h}{d}\right)^C \tag{2.8}$$

Where A' and $C = 0.15$ are constants, and h is the height at which the jet remains vertical, which is a function of the boundary layer thickness and jet velocity profile. This new model collapses trajectories better, but requires knowledge of the vertical jet height, which is difficult

to determine without prior information.

2.1.2 Coherent structures

Later important research focused on obtaining a coherent 3D representation of the JICF features. The vortex structures of the jet in crossflow were extensively studied by Fric and Roshko using smoke photography [40] and Kelso et Al. using dye injection [41]. They obtained detailed measurements and developed a 3D flow schematic, shown in Figure 2.5. Four types of coherent structures can be seen in the near field of a jet in crossflow: (i) the jet shear-layer vortices; (ii) the system of horseshoe vortices; (iii) the counter-rotating vortex pair (CVP); and (iv) the wake vortices.

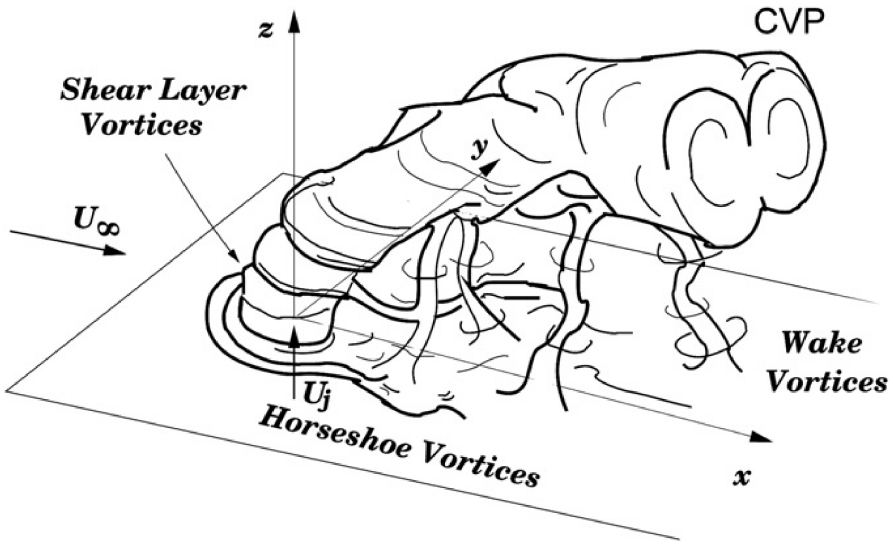

Figure 2.5 Jet in crossflow diagram developed by Fric and Roshko [40], adapted with permission

The jet shear-layer vortices form at the interface of the jet and the crossflow, while the horseshoe vortices originate at the base of the jet near the wall. The CVP develops when the jet is bent by the crossflow, and the wake vortices are generated downstream of the jet. Among these, the shear-layer vortices and wake vortices are unsteady, and the horseshoe vortices and the CVP have mean-flow definitions, although they also exhibit unsteady components [40]. It was initially believed that the JICF wake vortices were similar to Von-Karman vortex streets behind bluff bodies. To the contrary, the vortical structures in the wake of a JICF are not shed from the jet but originate from the boundary layer [40]. The formation process begins when the boundary layer behind the jet separates because of the adverse pressure gradient,

creating vortices based in the boundary layer that reach into the jet wake.

The JICF diagram was later refined by Lim and al. [42], shown in Figure 2.6. Their study concludes that the large-scale structures primarily consist of loops, shown in panel (a), which are generated by a Kelvin–Helmholtz instability at the jet to crossflow velocity shear interface. The CVP is initiated by the side hanging vortices, which are generated on the side shear layer of the jet, changing its initial cross-section round shape to a "U" pattern.

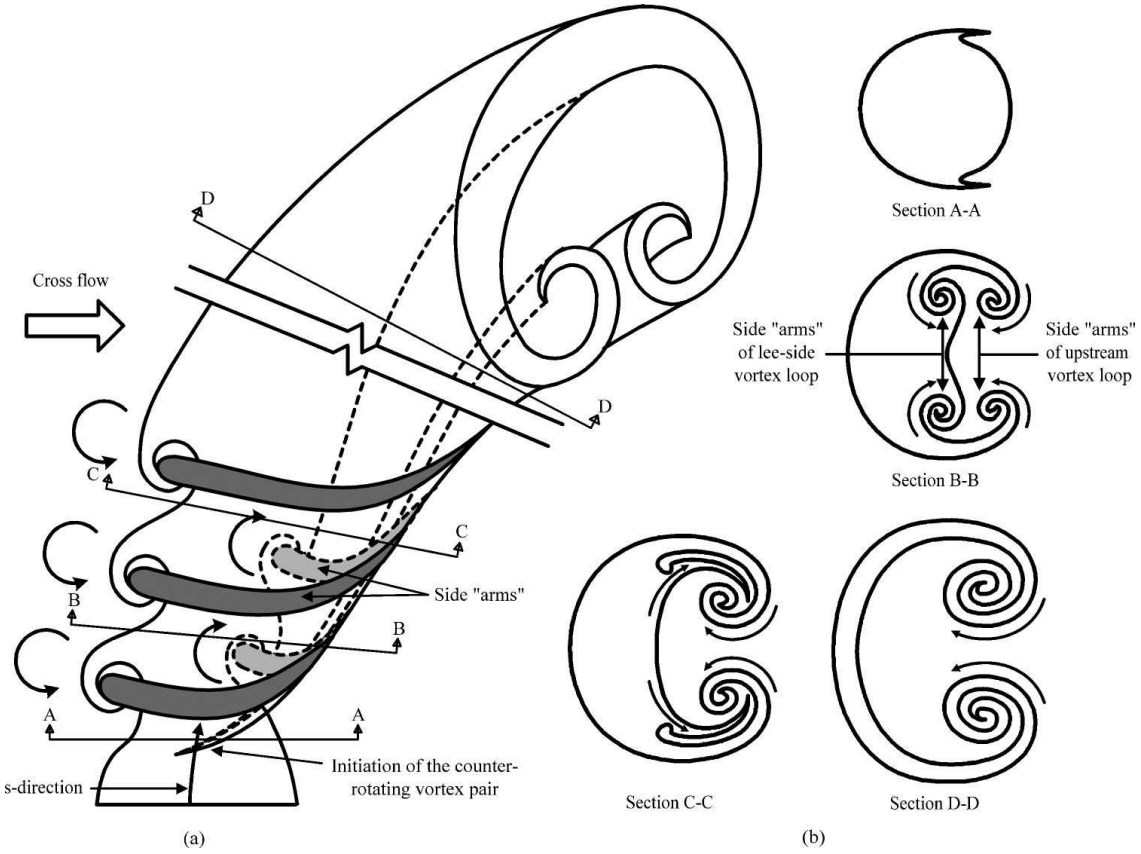

Figure 2.6 Jet in crossflow diagram with shear layer and hanging vortices developed by Lim et al. [42], adapted with permission

This challenged previous research beliefs that the CVP were caused by the folding of ring vortices around the shear layer [41]. Thus, an important feature of the new model is that upstream loops can exist without corresponding lee-side loops. The side arms, shown in darker shades of gray, are thought to initiate at the sides of the cylindrical vortex sheet and contribute to the formation of counter-rotating vortex pairs (CVP). Cross-sections A-A, B-B, and C-C shown in panel (b) illustrate the evolution of the jet cross-section as the distance from the centerline increases. The side arms play a crucial role in initiating the CVP by merging with the vortex loops.

The first Proper orthogonal decomposition (POD) of high-speed velocity measurements of a JICF with a stereoscopic PIV system was done by Meyer and al. in 2007 [43]. Proper orthogonal decomposition (POD) decomposes measurements into orthonormal modes based on energy, capturing the most energetic and largest structures in the initial modes. If the flow dynamics are dominated by a few large structures, the data can be effectively represented using only these first few modes that reflect the primary flow structures. Their study confirmed that at low velocity ratio $R = 1.4$, the shear-layer vortices are the dominant flow structures and that wake vortices lose significance. Also, the hanging vortices, similar to vortex tubes originating at the sides of the jet, theorized previously [42], are visible and contribute strongly to the CVP formation.

2.1.3 Mixing and concentration decay

More recent studies utilizes modern flow measuring techniques such as time resolved particle image velocimetry (TR-PIV) and planar laser induced fluorescence (PLIF) to obtain velocity and concentration fields.

Some of the first PLIF measurements of a JICF were done by Smith and Mungal in 1998 [39]. They used acetone vapor seeded into the jet to obtain quantitative 2-D images of the scalar concentration field. Their experimental study examines coherent structures in near field, mixing, and mean centerline concentration decay. All three regions of the transverse jet are investigated, showing that the jet can be scaled with three length scales: d, Rd and Jd, some more useful than others at different locations. The jet trajectory and dimensions in both the near and far fields show rd-scaling. The near field features a centerline concentration decay along the centerline coordinate ξ of $\xi^{-1.3}$, compared to the free jet decay rate of ξ^{-1} [39]. The "branch point" represent a position where the JICF transitions from enhanced to reduced mixing compared to the free jet, and occurs at a uniform scaled position $\xi/r^2d = 0.3$, marking the division between the near and far fields. Finally, self-similarity is not observed in the near field, but may be present in the far field. Averaged images also show that jet concentration can be asymmetric in the centerline plane [39].

Some of the first combined PIV-LIF data was obtained by Meyer and al. in 2002 [44] using a rhodamine seeded water jet. The averaged velocity and concentration profiles are shown in Figure 2.7 for the laminar and turbulent test cases. An increase in turbulence and jet Reynolds number show better mixing at a constant velocity ratio. Even across a difficult cross-section with strong velocity gradients, the PIV results are in accordance with Laser Doppler anemometer (LDA) point measurements. Some discrepancies were found where mixing is most intense, because the measuring volume of PIV/PLIF was too large (at 2mm

wide) to accurately capture the smaller scales present in areas of high turbulence and mixing.

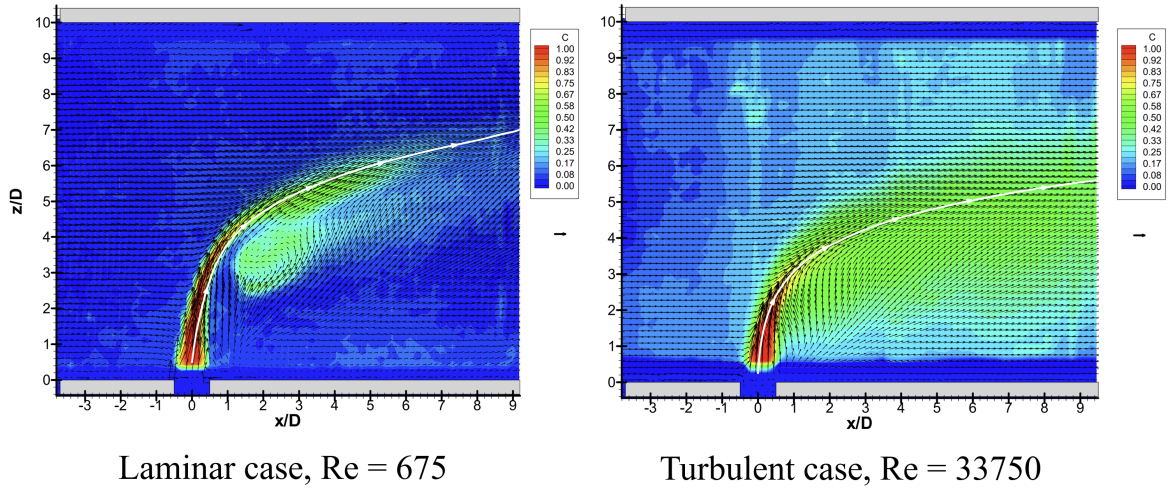

Figure 2.7 Jet in crossflow studied with PIV-LIF for R=3.3 by Meyer and Al [44], with permission

Similar simultaneous PIV-LIF was later done by Su and Mungal in 2004 at Stanford University [45]. Acetone vapor was added to a turbulent jet in crossflow at $R = 5.7$ with two injector position from flat to above the boundary layer. Raised injectors help fluid concentration and momentum to penetrate deeper into the crossflow. Although it was shown that nozzle position has no significant effect on the asymptotic state of the flow. It was finally concluded that the jet exit velocity profile has a greater impact on the evolution of the JICF mixing field than the position of the jet nozzle.

To investigate the mixing characteristics of round gaseous variable density JICF exiting from 3 varying nozzles, Karagozian's research group recently used acetone planar laser-induced fluorescence (PLIF) [46]. It was found that jets with density ratios below 1 tend to mix less efficiently than other cases. This effect is attributed to the differences in how the higher-density crossflow entrains into the lower-density shear layer vortices of the jet. Also, jets with a globally unstable upstream shear layer and symmetric CVP show better local molecular mixing than jets with convective unstable upstream shear layers and asymmetric structures. However, convective unstable jets can exhibit greater spatial evolution downstream, especially when shear layer roll-up occurs, which improves mixing.

The next section focuses on the instabilities present in jets in crossflow to better explain their effect on mixing.

2.1.4 Instabilities

The jet in crossflow is by nature an unsteady and unstable flow field. Many previously mentioned experimental and numerical studies showed the presence of self-sustained oscillations in the JICF. These are instabilities that persist in the flow without the need of periodic external forcing. Two types of local instabilities are visible in such flows: convective and global instabilities [47]. In local convective unstable flows, disturbances move along the flow and its upstream region remains largely unaffected. These instabilities are "swept away" from their origin. In local absolute instability, the disturbance grow and spreads in all directions. The presence of absolute instabilities indicates a more profound level of instability in the jet flow, and can lead to widespread global oscillations in the system. The term "local" refers to the instability of the individual velocity profile, while the term "global" refers to the instability of the entire flow field. This terminology was coined by Briggs [48] in 1964, and applied to spatially developing flows by Chomaz [49], as illustrated in Figure 2.8.

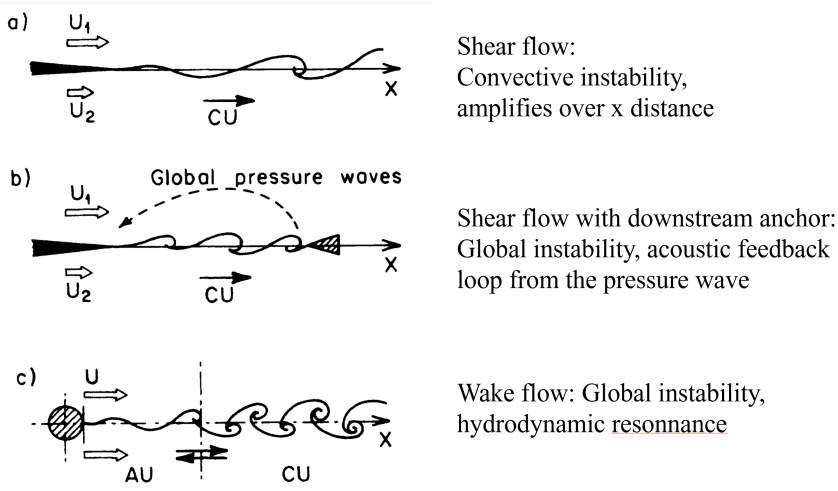

Figure 2.8 Classical flow examples of convective and absolute instabilities leading to globally unstable oscillations, adapted from Chomaz et Al [49] with permission.

The distinction between convective and absolute instabilities is frame-dependent, as a convective instability may seem absolute to an observer moving with the wave (Lagrangian frame). It is important to look at which critical values the flow field becomes absolutely globally unstable, and to measure its oscillating modes.

Monkewitz [50] studied and categorized these instabilities in a classical free jet by varying its Reynolds number and density ratio S. Regular sequences of strong vortex structures were observed for $S < 0.73$ and $Re = 7500$. These self-excited oscillations signifying a switch to global absolute instabilities. Reducing the density ratio by heating the jet caused the

absolutely unstable mode to increase in strength. As S decreased, this mode was clearly visible with an increase in shear layer vortex size and coherence. It was also shown that near-laminar jets with a Reynolds number of 7500 exhibit instabilities proportional in size to the jet diameter. However, as turbulence increases with Reynolds numbers up to 50000, the instability size decreases, approaching the shear layer thickness [50]. The smaller scale eddies disrupt the perfect phases of the vortex shedding found at laminar to turbulent transition Reynolds number values. Turbulence helps to maintain more constant average velocity profiles and reduces self-excitation.

More recently, Megerian et al. [51] investigated JICF shear-layer instabilities using a hot-wire anemometer. They examined the spatial variation of the jet exit velocity and the spectral characteristics of the velocity centerline. As the velocity ratio decreased, the spectral character changed significantly, as shown in Figure 2.9. Multiple amplitude peaks show in the Strouhal number range of 0.7, and appearing closer to the jet exit as the crossflow velocity increased. For $R < 3.5$, the flush jet exhibited a strong fundamental mode near the jet exit, particularly notable for $R = 3$ and $R = 2$ [51] . This rapid emergence of a dominant mode and harmonics with decreasing jet-to-crossflow momentum flux ratio J reminds of the similar phenomenon observed in the spectral characteristics of heated free jets in the previously mentioned work of Monkewitz. This shift to absolute instabilities is visible in Figure 2.9 (b) along the jet shear layer position where a strong signal amplitude at $St = 0.7$ (and its integer harmonics) is visible and does not decay.

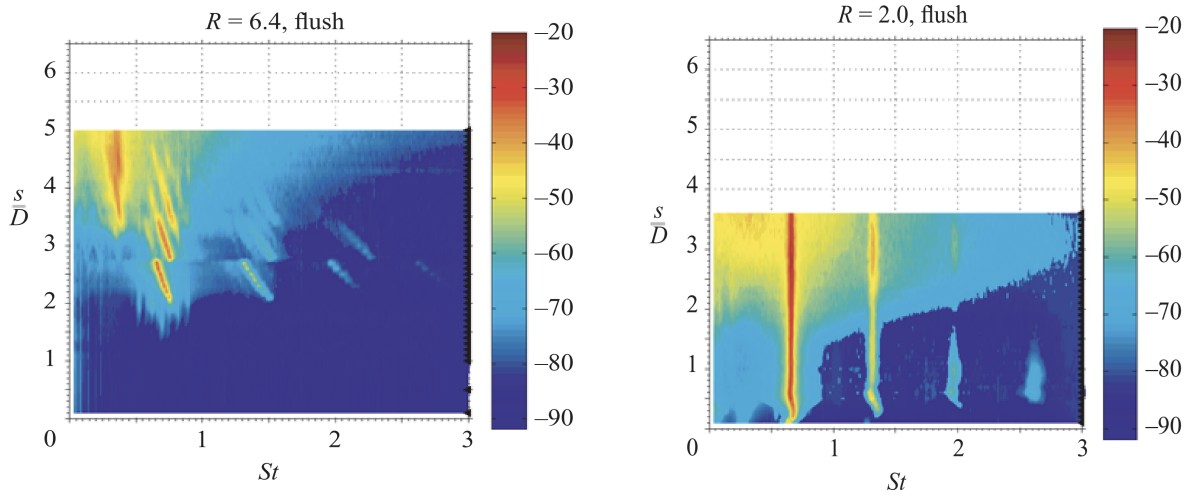

Figure 2.9 Amplitude and frequency of instabilities in the time-wise velocity data along the JICF centerline s/D from Megerian et al. [51], adapted with permission

Figure 2.9 uses the Strouhal number St to characterise the measured frequencies. It is a

dimensionless number that describes oscillating flow mechanisms, and is defined as:

$$\mathrm{St} = \frac{fL}{U} \tag{2.9}$$

Where f is the frequency of vortex shedding (Hz), L is a characteristic length (m), and U is the flow velocity (m/s).

Work by the same research group explores in detail how the upstream shear layer of a JICF transitions from convective to absolute or global instability as J decreases, using numerical [52] and experimental methods [53]. The experimental study measured instabilities in the shear layer of the jets using single-component hot-wire measurements. By analyzing the power spectra of the velocity signals, oscillatory peaks could be identified, and indicated the presence of global instabilities. These peaks were associated with specific modes of oscillation that developed as J and S were varied. When the density ratio S is reduced below 0.45-0.40, the jets transition from convective instability to global instability [53]. The presence of global instabilities is linked to sharp shifts in the Strouhal number and decreased mixing because it often leads to the formation of large, organized vortices. These coherent structures can inhibit the smaller-scale turbulence that is typically more effective at mixing fluids. As a result, energy can remain trapped in large-scale motions, limiting the transfer to subharmonic structures that help dispersion.

2.2 Multiple jets in crossflow

Some of the first work on multiple jet in crossflow array can be attributed to Holdeman [54]. His research focused on evaluating the effect of injector shape on heated jets injected into a cold crossflow to measure the downstream temperature field using probes. This temperature field was used to infer mixing between both flows. A total of 15 different shape and spacing were studied in a wind tunnel described in Figure 2.10.

We define in this thesis the center-to-center jet spacing l which is often non-dimensionalized by the jet diameter to compare different geometries with l/d. It is a key non-dimensional geometrical parameter when multiple jets are used. The results of this NASA study [54] can be summarized as follows:

1. The momentum-flux ratio J is the main parameter for flow behavior and mixing;
2. Mixing increases with downstream axial distance;
3. The effect of injector shape on jet arrays are significant only in the near-field region. Beyond $x/D > 4$ scalar distributions are similar to those of standard circular orifices.

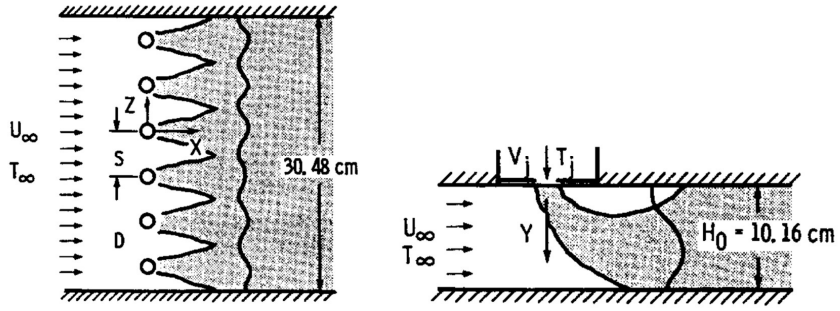

Figure 2.10 Previous experimental setup to study multiple arrays of jets in crossflow by Holdeman [54], adapted with permission

4. Achieving equivalent mixing at smaller momentum-flux ratios requires a longer downstream distance.
5. Greater orifice spacing and jet diameter at a fixed J enhanced jet penetration but reduced lateral flow uniformity (closely spaced small injectors under-penetrate compared to widely spaced bigger jets)
6. Larger orifice diameters at a fixed spacing-to-diameter ratio (l/d) increased jet penetration, yet decreased lateral flow uniformity;

A similar jet array study was conducted by Moawad and Rajaratnam at the University of Alberta [55]. The concentration of seeded rhodamine dye in water jets, 8 mm in diameter, was measured using a rake system connected to a fluorometer. This enabled measurements of concentration profiles and contours along the centerline and lateral planes. Their findings suggest that the presence of multiple jets generally diminishes dilution in the mixing region. This is likely caused by the interference of merging plumes, which affects the entrainment mechanisms. As the plumes merge, the available surface area decreases, leading to a reduction in entrainment for each individual jet [55]. Also, as the spacing between the jets increased, the jets were merging further downstream.

This led to the creation of 3 distinct analysis zones shown in figure 2.11. In zone I, each jet diffuses independently without significant interference from neighboring jets. Zone II refers to a transition zone where there the jets begin to partially merge. The merging distance of the jets from the injector, defined as x_m, is mainly influenced by the velocity ratio J and the relative jet spacing l/d. When J increases, the merging distance decreases [55]. For closely spaced jets, values of x_m/d varied from 1.8 to 0.22 for $J = 3.5$ to $J = 10$. Spaced out jets observe x_m/d from 5 to 2.5 for $J = 5$ to $J = 8$. Finally zone III refers to the downstream distance at which the jets have merged completely and become indiscernible in

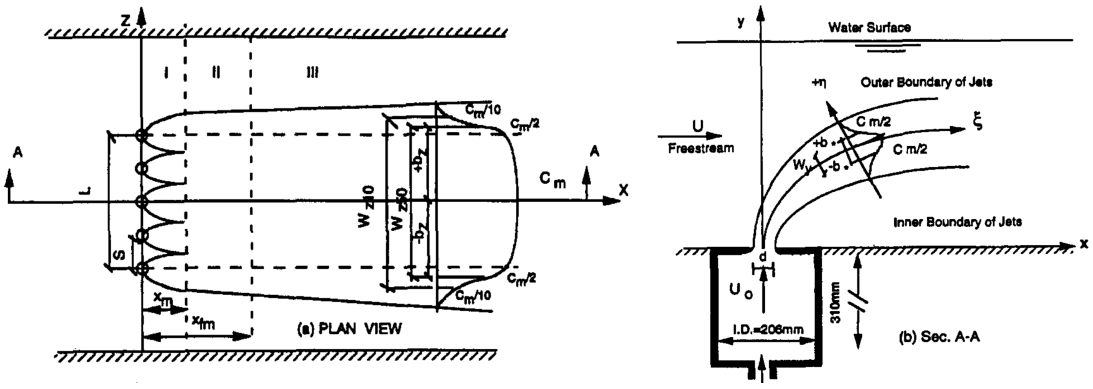

Figure 2.11 Previous experimental setup to study arrays of liquid jets in crossflow by Moawad et al. [55], adapted with permission

the concentration profiles.

Ajersch et al. also studied an array of six square 12 mm JICF spaced by $l = 3d$ for film cooling purposes [56] . Their study compared velocity profiles and turbulent kinetic energy (TKE) data from numerical simulations and experimental wind tunnel measurements. Images showed that jets interact for $R > 0.5$, but below that value they are swept before penetrating above the boundary layer $2d$ in size. The study revealed that for $R > 0.5$, the jets interact both with each other and with the crossflow, penetrating above the boundary layer. This interaction zone showed increased instability and shear, leading to elevated turbulence levels from $x/d = 1$ to $x/d = 8$. In contrast, for $R < 0.5$, the jets are swept downstream and remain confined within the boundary layer, limiting their penetration and reducing interaction.

Most recent studies of multiple jet arrays are investigating cooling in gas turbine systems either using film cooling with slanted low velocity ratio jets, or straight impinging jets at very high velocity ratios [57–59]. In all cases, the jet in crossflow is modulated to quickly come in contact with the upper or lower wall to help cool it down. This is the opposite of what the micromix systems aims to achieve, because the jets have to mix with the crossflow and penetrate above the boundary layer.

Recent work on multiple tandem jets was conducted by Kristo and Kimber [60]. A tandem array of three jets was investigated using high-speed time-resolved PIV. This enabled the analysis of first and second-order turbulent statistics, streamline trajectories, recirculation areas, and penetration depths. Proper Orthogonal Decomposition (POD) is applied also to the instantaneous velocity fields in the spanwise plane to identify the dominant flow features. It was found that the first jet acts as a "shield" to the subsequent jets, helping them to penetrate deeper into the crossflow.

2.3 Research gap and specific research objectives

This state-of-the-art review shows that measurements have not been made with arrays of multiple microscale injectors with diameters below 1 mm. Due to its low density relative to air ($S \approx 0.068$), hydrogen jets are more susceptible to globally unstable flow, leading to periodic instantaneous fuel-to-air concentration profiles that can hinder combustion stability and emissions. This experimental study thus covers notably smaller jet diameters and density ratios, including array spacing relevant for micromix combustors in hydrogen fueled gas turbines.

Precise and specific objectives based on this literature review are to:

- Develop an experimental setup to obtain high frequency recordings of low density micro jet arrays in crossflow.
- Compare low density micro jet array trajectories to classical JICF models.
- Develop a method to measure mixing of the JICF, relying on the available PIV system.
- Measure the effect of jet array spacing on the flow field coherent structures and instabilities.

CHAPTER 3 METHODOLOGY

This chapter explores the experimental and numerical methodology employed in this thesis.

3.1 Crossflow rig

3.1.1 General layout

The crossflow channel, shown in Figure 3.1, is the main test section for investigating jets in crossflow (JICF) with high spatial and temporal resolution. Originally designed for hypergolic hybrid rocket fuel ignition experiments [61], this experimental rig has been modified to support detailed JICF studies. This general layout of the experimental setup can be seen in figures 3.2 and 3.3, which show photographs of the general experimental layout with and without a laser sheet.

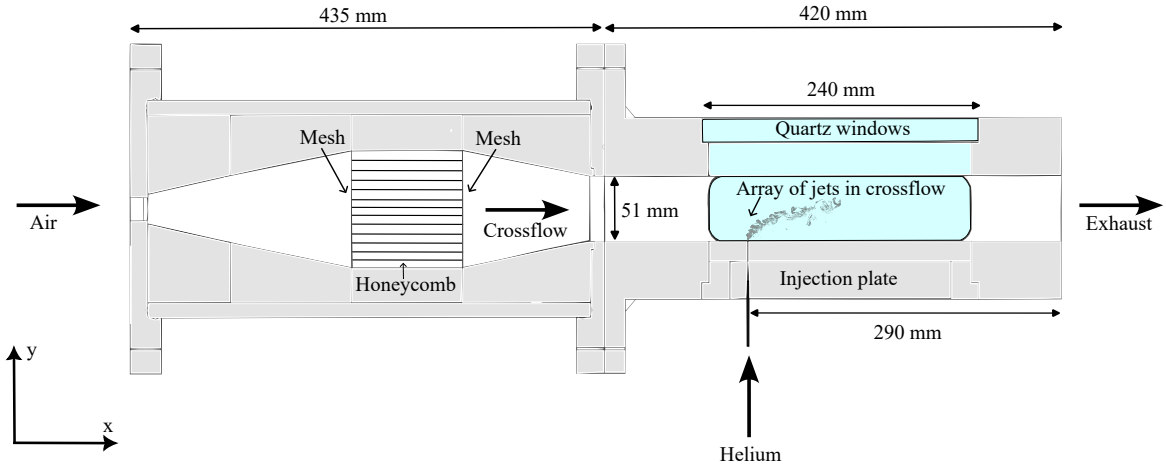

Figure 3.1 Experimental setup to study arrays of helium jets in crossflow

The test section spans 420 mm in length with a square channel cross-section of 50.8 × 50.8 mm, creating a controlled environment for examining jet and crossflow interactions. Optical access is achieved through three 45 mm thick quartz windows on the sides and top of the test section, providing clear access for the camera. To ensure a consistent and well-conditioned crossflow, an upstream diverging-converging section with honeycombs and grids is used to straighten the airflow and minimize lateral velocity components. The crossflow velocity is maintained at a constant 2 m/s, which corresponds to a Reynolds number of 6800, and is precisely monitored via a Coriolis mass flow meter (Bronkhorst mini Cori-Flow M15).

A jet-to-crossflow density ratio of 0.14 was achieved using helium, as a proxy to hydrogen, selected for its similar diffusivity and density, and for safety precautions in this non-reactive study. The helium flow rate is varied from 1 to 10 SLPM, with a mass flow controller (Hasting HFC 202) calibrated with a DryCal Piston calibrator (MesaLabs ML-500). This enables practical jet to crossflow momentum flux ratios J in the range of 0.5 to 100. To prevent helium leakage, leak detection tests were performed with soapy water on the stainless steel tubing after its assembly Injectors consist of one to eight medical grade needles (Unimed S.A.) of $d = 0.8 \pm 0.03$ mm interior diameter. The technique used to cut them needles is detailed in section 3.1.3. This needle-in-a-hole design facilitated the study of different jet diameters and geometries for a given arrangement.

As shown in Figure 3.2, camera movement is facilitated by a robust metallic translation stage (Thorlabs), allowing precise positioning and stability during measurements. Fine adjustments of the laser sheet lateral position is possible using a micro-meter stage attached to the final converging optical lens, ensuring accurate alignment with the injector.

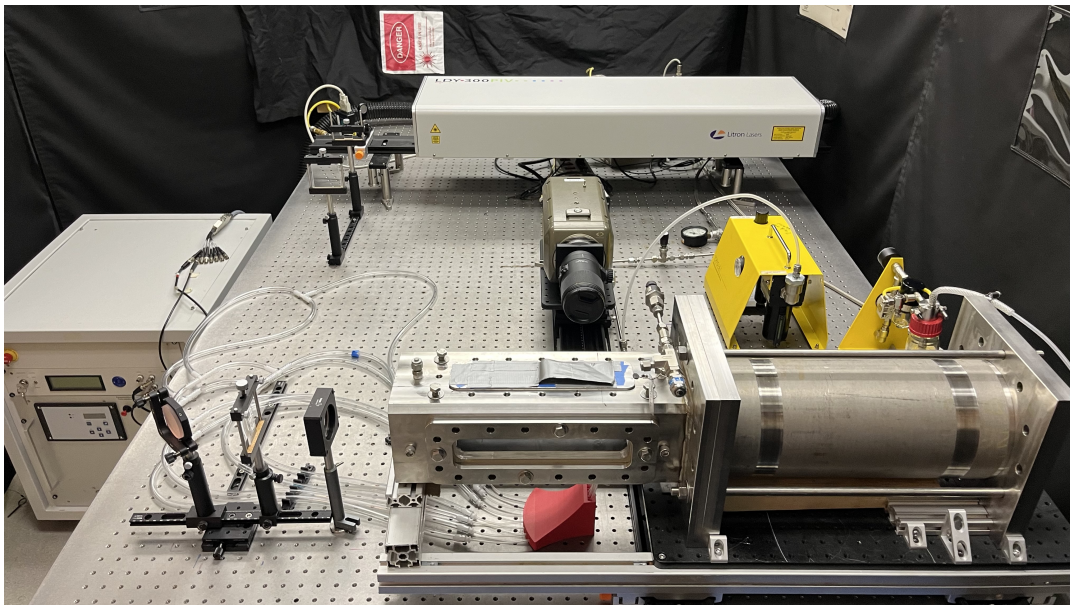

Figure 3.2 Experimental setup with the crossflow rig, helium lines, injector ramp, dual-head laser, high-speed camera and DEHS oil seeders

Figure 3.4 shows the piping and instrumentation diagram for the JICF experimental setup, illustrating the flow paths and connections, control instrumentation, and key equipment.

The following sections will provide detailed descriptions of the modular injection plate, the array spacing geometries, and the needle cutting technique used in the experimental setup.

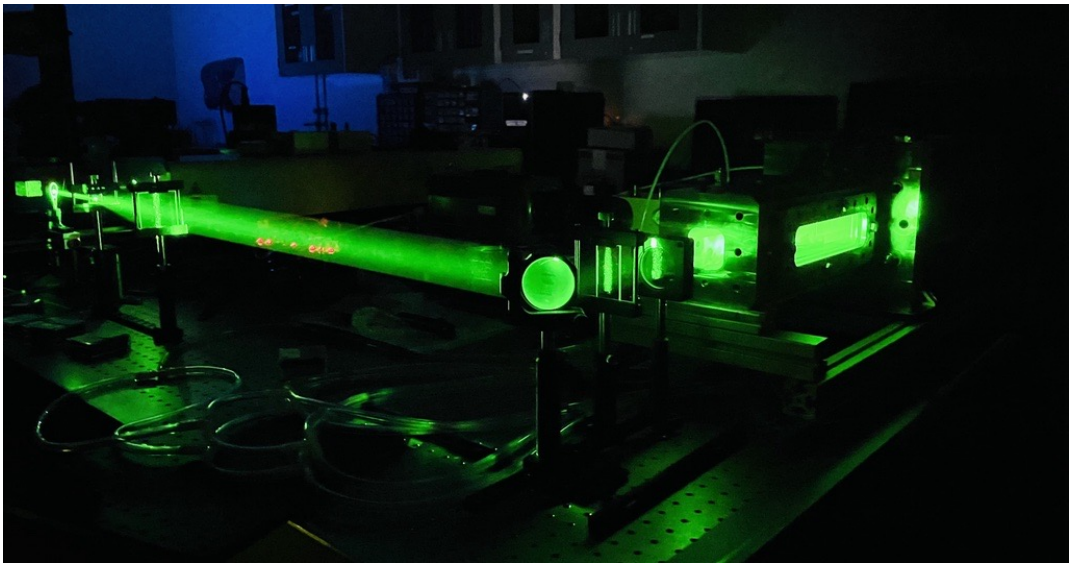

Figure 3.3 Laser sheet illuminating the interior of the crossflow rig

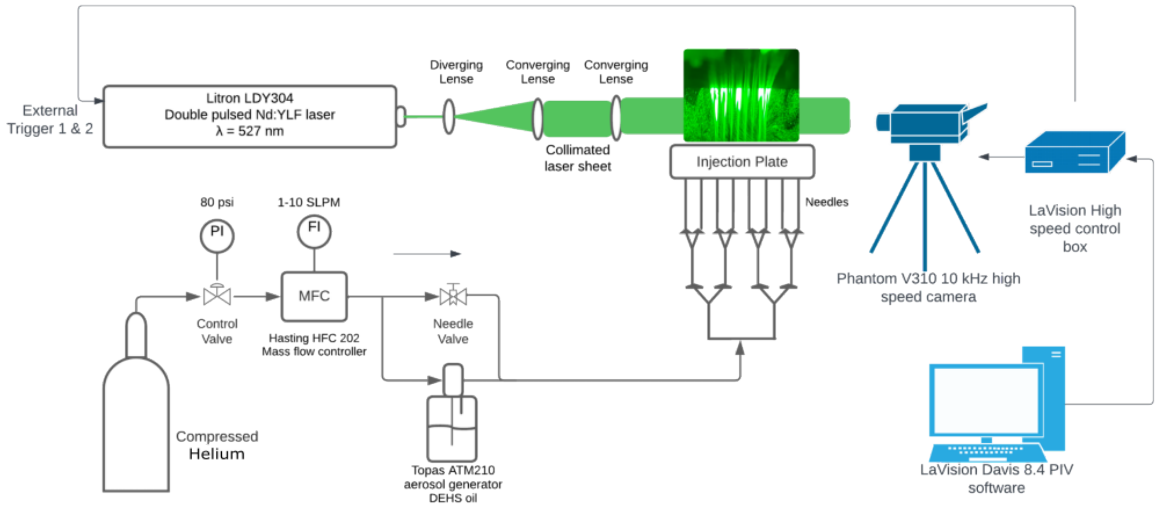

Figure 3.4 Piping and instrumentation diagram of the helium JICF experimental PIV setup

3.1.2 Modular injection array plate

To enable flexible adjustments in jet-to-jet spacing and array configurations, a modular injection plate was designed and machined from aluminum. As shown in Figure 3.5, this two-part plate consists of an upper and bottom section. The top plate features precisely drilled injector holes, each 1.1 mm in diameter, where needles are securely glued with epoxy to ensure

stability and a tight seal. The flared bottom plate is designed to attach firmly to the test section floor with a bolted flange. It includes machined holes that align with those threaded in the top plate, allowing the two to be screwed together and held in place. The bottom plate is also hollow inside, providing clearance for the needles to pass through without obstruction.

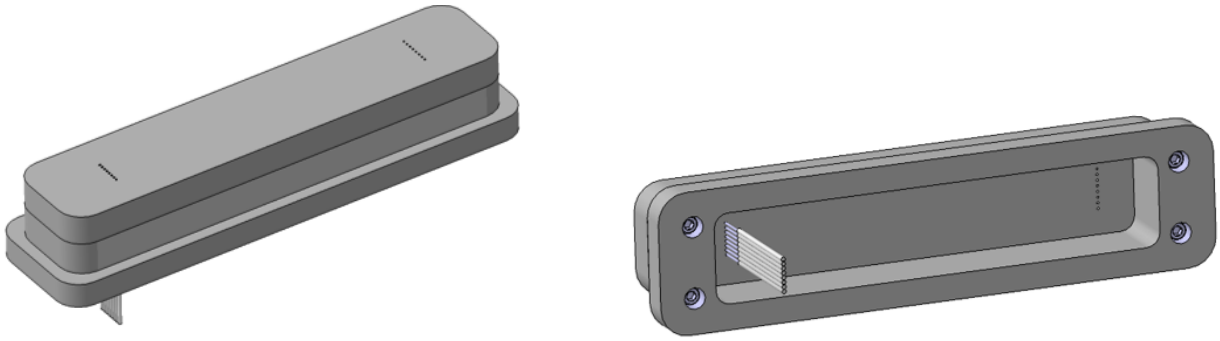

(a) (b)

Figure 3.5 Two-part modular injection plate for arrays of jets in crossflow: (a) isometric view showing top plate with JICF arrays, (b) bottom view with screws and hollow bottom plate.

This modular configuration allows for various jet-to-jet spacing arrangements, which are detailed in table 3.1 and used throughout the experimental campaign. Edge-to-edge spacing, referred to as jet array spacing l/d, is the main parameter used from now on.

Table 3.1 Jet array spacing used in the experimental tests

# of jets	Center-to-center spacing		Edge-to-edge spacing	
	l_c (mm)	l_c/d (-)	l_e (mm)	l_e/d (-)
8	2.00 ± 0.03	2.50 ± 0.04	1.20 ± 0.03	1.50 ± 0.03
8	2.50 ± 0.03	3.12 ± 0.04	1.70 ± 0.03	2.12 ± 0.03
4	5.00 ± 0.03	6.25 ± 0.04	4.20 ± 0.03	5.25 ± 0.03
1	∞	∞	∞	∞

3.1.3 Needle injection

Medical grade needles with a constant interior diameter $d_j = 0.8 \pm 0.03$ mm are used to inject helium into the crossflow. These metal capillaries were bought in bulk from Unimed S.A. (Lausanne, Switzerland). A needle length of $L_j = 50 \pm 0.5$ mm ensures a high enough length over diameter ratio $L_j/d = 62 > 0.06 \cdot Re_j$ that enables a fully developed laminar flow to form at the needle exit for all jet flow rates [62].

To ensure reliable injection of the jet fluid, specific care was taken to have precisely cut metal capillary edges. Several cutting techniques were investigated, and the quality was assessed with a microscope. Water cutting results are shown in Figure 3.6c and 3.6d. Laser cutting results are shown in Figure 3.6e. Electrochemical machining (ECM) results are shown in Figure 3.6a and 3.6b. A water-cooled precision saw target preparation device equipped with a stereo microscope (Leica, EM TXP) was also used with a custom insert tool to hold the needles. Results are shown in Figure 3.6f, displaying the best cut precision across all methods tried. This method was chosen for the quality and repeatability of the results. The final assembly uses epoxy glue to connect the 0.8 mm diameter needle injector to the capillary plastic tubing, and is visible in Figure 3.7. The needles are carefully mounted flush to the test section floor to prevent protrusions that could disturb the flow and cause laser reflections.

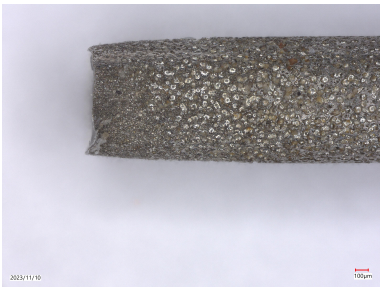

(a) Lateral view, ECM

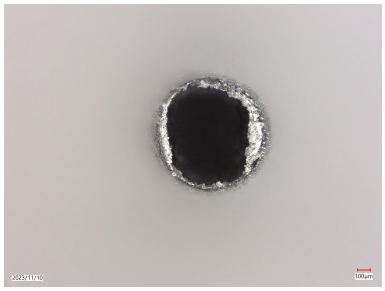

(b) Top view, ECM

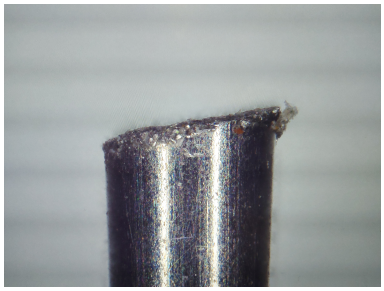

(c) Lateral view, Water Cut

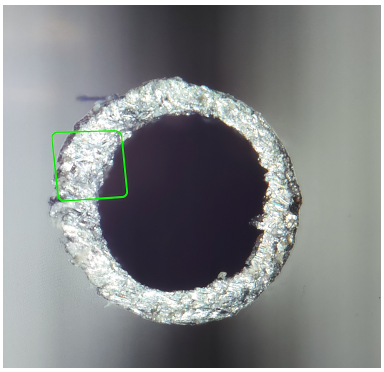

(d) Top view, Water Cut

(e) Top view, Laser Cut

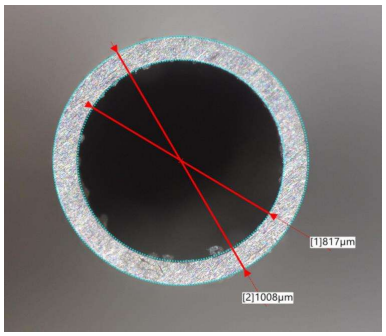

(f) Top view, Precision saw

Figure 3.6 (a, b) ECM cutting of fine needles, (c,d) Water jet cutting of fine needles, (e) Laser cut and (f) precision water-cooled Leica saw for target preparation

At the beginning of each test phase, special care is taken to purge air from the lines such that only helium remains. The effect of this purging is visible as the jets lose momentum

when helium concentration increases until steady state is achieved.

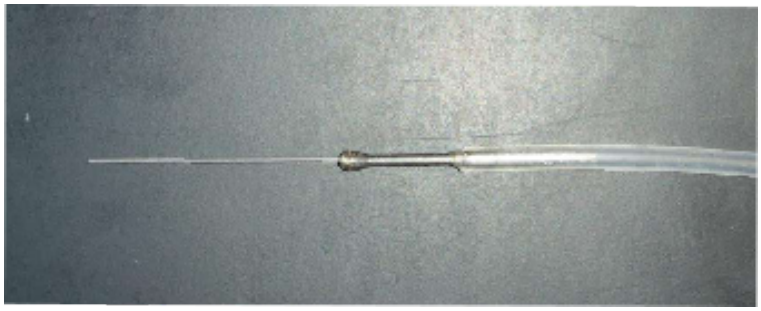

Figure 3.7 Final needle arrangement connected to capillary plastic tubing

Finally, to ensure identical flow rate within the 8 helium lines, a 3D printed injection ramp was designed. It allows for a similar tubing trajectory and curve to ensure a similar pressure drop. This ramp is visible in red below the injection plate in Figure 3.2. Each plastic tubing is 0.5 m in length and connects via a plastic tee junction of 0.6 mm in diameter.

3.2 Particle image velocimetry

This work relies on Particle Image Velocimetry (PIV), a non-intrusive optical technique that provides instantaneous velocity measurements within the flow field. The PIV system features a high-speed camera (Phantom v310), equipped with a 150mm f2.8 macro lens (Sigma), to capture high-resolution images in the test section. The instrumentation diagram of this setup is displayed in Figure 3.4 and a photograph of the camera arrangement in Figure 3.2. The LaVision Davis 8.4 software is used for analysis and post-processing of the PIV images. A double pulsed Nd:YLF laser (Litron LDY304) operating at a wavelength of $\lambda = 527$ nm is employed to illuminate the seeded particles. The energy and intensity settings of the laser are controlled to provide clear and accurate particle tracking without saturation. Pairs of images offset by a typical δt= 40 μs are recorded at a frequency of 10 kHz. The spatial resolution of 15 to 40 pixels per mm, based on a camera resolution of 1280×800 and combined with a final interrogation window size of 12 by 12 pixels overlapped by 50%, yields a maximal spacing between velocity vectors of 300 μm. However, for 10 kHz high-speed recordings the resolution needs to be reduced to 512×280 pixels. This leads to a spatial resolution of 24 pixels per mm in the streamwise longitudinal XY plane (camera from the side window) and to 12 pixels per mm in the transverse YZ plane (camera through the exhaust). This yields an imaging domain in the longitudinal XY plane spans from $x/d = -2$ upstream of the injector tip to $x/d = 24$ and vertically from the injection plate floor at $y/d = 0$ to $y/d = 15$. The laser is collimated by passing through a series of plano-cylindrical NBK-7 optical lenses; $f = -30$

mm and $f = 300$ to expand the beam in the vertical direction, then $f = 500$ mm to reduce its thickness. It is narrowed to thickness smaller than the jet diameter, at approximately 0.6 mm. The method used to measure this laser sheet thickness is detailed in section 3.2.2. The jets are seeded with droplets of Di-Ethyl-Hexyl-Sebacate (DEHS) oil using an aerosol generator (Topas ATM 210) operating at 80 psi. It is connected in series after the mass flow controller providing droplets with an average diameter of 0.5 μm. When air seeding is required for PIV data acquisition, a second aerosol generator (Topas ATM 221) operating at 100 psi is connected to a tee connection before the flow settling section.

3.2.1 Particle laden flow

In this study, DEHS (Di-Ethyl-Hexyl-Sebacate) oil particles are added to visualize and measure the flow field. Understanding their interaction with the fluid flow is important to make sure that these particles accurately follow the movement of the fluid, but also reflect and scatter enough light from the laser to the camera.

For very small particle tracers, the difference between the particle velocity v_p and that of the surrounding fluid U is referred to as the slip velocity and can be approximated by [63]:

$$v_p - U = \frac{d_p^2(\rho_p - \rho_f)}{18\mu_f}\frac{dv_p}{dt} \tag{3.1}$$

Where, v_p represents the velocity of the particle, while U denotes the velocity of the fluid. The term d_p is the diameter of the particle, ρ_p is the density of the particle, and ρ_f is the density of the fluid. The dynamic viscosity of the fluid is given by μ_f, and $\frac{dv_p}{dt}$ represents the particle's acceleration. Clearly, using same density particles and fluid ($\rho_p - \rho_f = 0$) leads to accurately flow tracking. While this condition can be satisfied for liquid flows, it is very challenging to achieve in gas flows, where the typical particle to flow density ratio is $\rho_p/\rho_f \approx 10^3$. Therefore, smaller particles (0.5 µm $< d_p <$ 5 µm) are employed to reduce the slip velocity. The particle response time τ_p, when considering the stokes regime hypothesis around the particle, is given by [63]:

$$\tau_p = \frac{\rho_p d_p^2}{18\mu_f} \tag{3.2}$$

Where ρ_p is the particle density, d_p is the particle diameter, and μ_f is the dynamic viscosity of the fluid. Stokes' drag law is applicable when the particle Reynolds number Re_p is less than one. This condition is typically met for small particles and low relative slip velocities. It is also a conservative estimate of the particles' tracking ability because the drag force on

the particles tends to be higher than what is predicted [64].

The fidelity of flow tracers in turbulent flows is quantified by the particle Stokes number Sk. It is a dimensionless quantity, defined as the ratio of the particle response time (τ_p) to a characteristic timescale of the fluid flow (τ_f).

$$Sk = \frac{\tau_p}{\tau_f} \tag{3.3}$$

The particle response time should be smaller than the smallest timescale of the flow to ensure accurate tracing. Practically, ensuring $Sk < 0.1$ results in acceptable flow tracing accuracy, with errors below 1% [63].

The characteristic timescale of the fluid flow (τ_f) can be defined based on the flow conditions. For instance, in a jet flow, τ_f can be approximated by:

$$\tau_f = \frac{D_j}{U_j} \tag{3.4}$$

where D_j is the jet diameter, and U_j is the jet velocity. For our particular case, given an average particle diameter d_p of 0.5 μm, a maximal jet velocity $U_j = 50$ m/s, helium dynamic viscosity of $\mu_f \approx 1.96 \times 10^{-5}$ kg/(m s), DEHS particle density of $\rho_p \approx 914$ kg/m^3 and a jet diameter of $(d_j) = 1$ mm; calculating τ_p, τ_f and Sk yields:

$$\tau_p \approx 6.48 \times 10^{-7} \text{ s} \tag{3.5}$$

$$\tau_f = 2 \times 10^{-5} \text{ s} \tag{3.6}$$

$$Sk = \frac{\tau_p}{\tau_f} = \frac{6.48 \times 10^{-7}}{2 \times 10^{-5}} = 0.0324 < 0.1 \tag{3.7}$$

Therefore, the Stokes number for DEHS particles in the helium jet is smaller than 0.1 and should behave like a good flow tracer.

3.2.2 Laser sheet thickness

Having a thin laser sheet in PIV measurements is important to only illuminate the particles within the region of interest, especially when sub millimeter jet diameters are in play. This helps the accuracy of measurements by reducing the illumination of out-of-plane particles. To this end, the laser beam profile was analyzed using and Newport PMKIT-06-01 optical power meter and detector. A sharp knife edge, mounted on a micrometer traverse, was used to gradually block the laser beam. By taking measurements of the laser intensity at different

positions of the knife edge, a dataset that represents the cumulative intensity distribution is obtained. In order to reduce noise, each measurement corresponds to the average intensity over 30 seconds. To obtain the shape of the laser beam, the derivative of the intensity data $I(x)$ with respect to the knife-edge position x is plotted. This $\frac{dI}{dx}$ derivative corresponds to the intensity profile of the laser beam, which is numerically computed with a second order finite difference scheme. This profile reveals important characteristics of the laser beam such as its width, symmetry, and peak intensity. By applying smoothing techniques, like Gaussian filtering, the derivative can better reflect the underlying laser profile without being influenced by noise in the measurements.

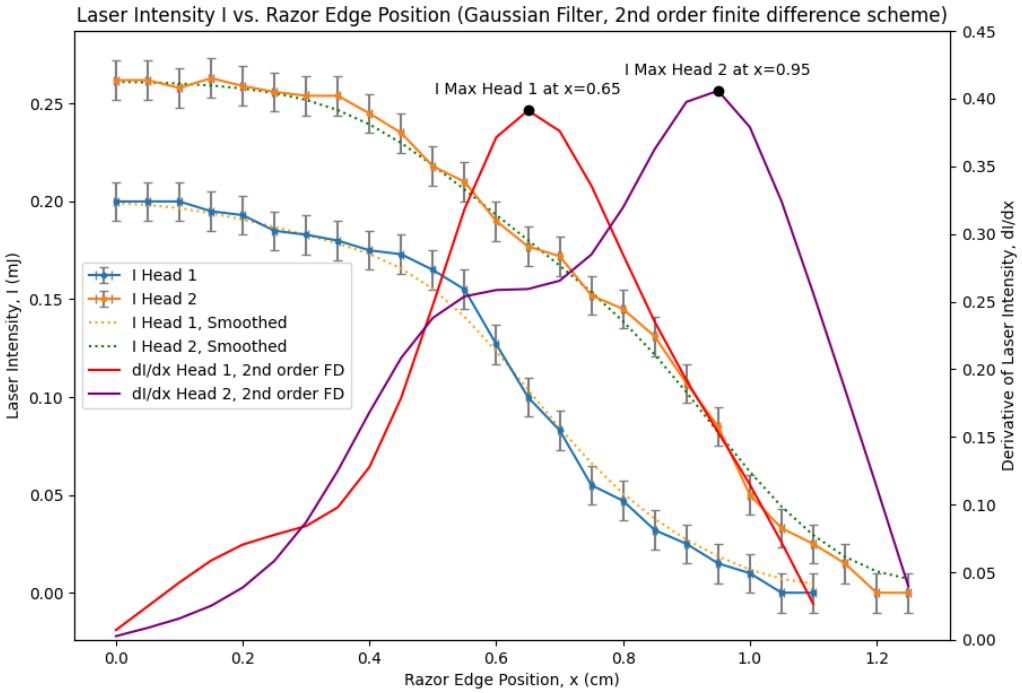

Figure 3.8 Laser beam profile at the exit for both heads

The resulting cumulative intensity distributions as a function of knife-edge position and beam profiles are shown in figure 3.8 and 3.9 for both laser heads. Measurements directly at the exit of the laser, before shaping the beam with any optical components, are illustrated in Figure 3.8. It shows that, because of wear, the laser head #1 has an intensity of 0.26 mJ which is 30% higher than head #2 at 0.20 mJ. A misalignment of 3 mm between both head peak intensities is also visible. Finally, the laser beam from head 1 is thinner, having a full width half maximum value (FWHM) of 4.5 mm compared to beam #2's FWHM value of 6.5

mm.

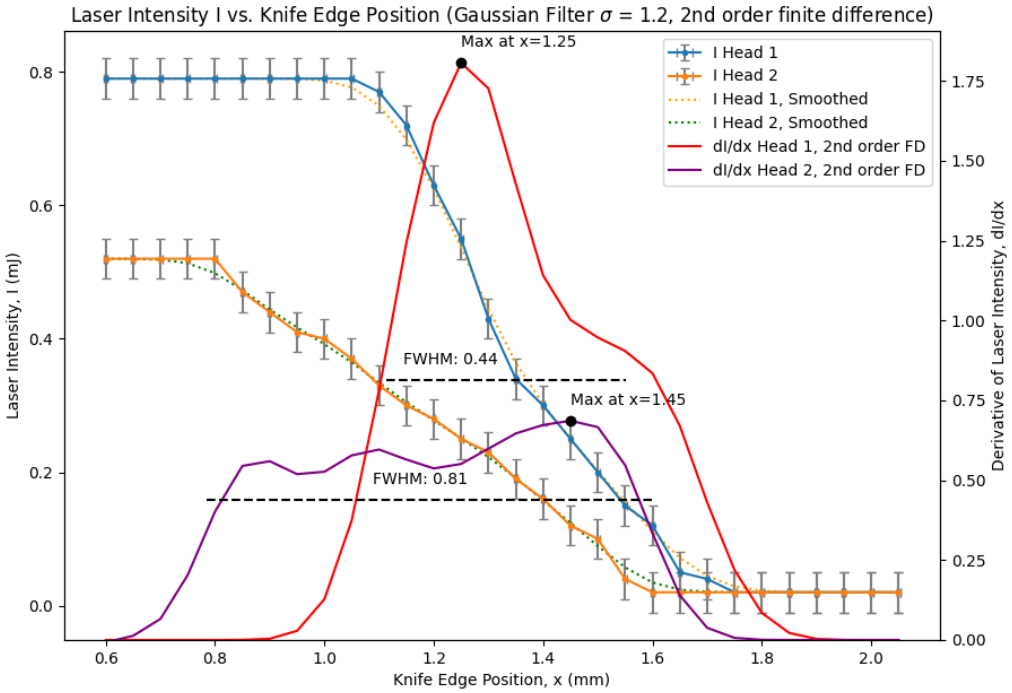

Figure 3.9 Collimated laser sheet profile

Figure 3.9 shows similar intensity and profiles for both laser heads, but were measured at maximal laser power in the thin laser sheet zone after it was collimated with a series of optical components. Laser head #1 has an intensity of 0.79 mJ, while head #2 has an intensity of 0.54 mJ. Head #2 is wider with a FWHM of 0.81 mm when compared to Head #1, showing a sharper profile with a higher peak and a FWHM of 0.44 mm. The sheet thickness of 0.6 mm is approximately the size of the jet injector, of $D = 0.8$ mm. This is good, but not perfect, especially when taking into account the misalignment of 0.2 mm between the peak intensities of the laser heads.

3.2.3 Dual-head laser pulse time interval

One of the main parameter influencing the PIV measurements quality is the time between each double frame images, defined as δt. A preliminary study was done for a crossflow of 1.8 m/s and a final interrogation window size of 12 pixels. Velocity profiles were obtained by averaging the velocity magnitude of 500 instantaneous PIV vector fields across multiple x-positions slices at each y-position. The results are shown in Figure 3.10, revealing that

a δt of 50 microseconds was optimal, allowing sufficient particle displacement (3-5 pixels) between shots for accurate tracking. For a smaller δt of 10 and 20 microseconds, the velocity measurements increased by 35%. This error is caused by the very small particle movement of below 2 pixels between images. Also, δt values greater than 100 microseconds led to particle displacements near the interrogation window size of 8 pixels, causing velocity underestimation of 10%. Balancing δt to achieve adequate particle movement for the entire velocity range is essential for robust PIV measurements.

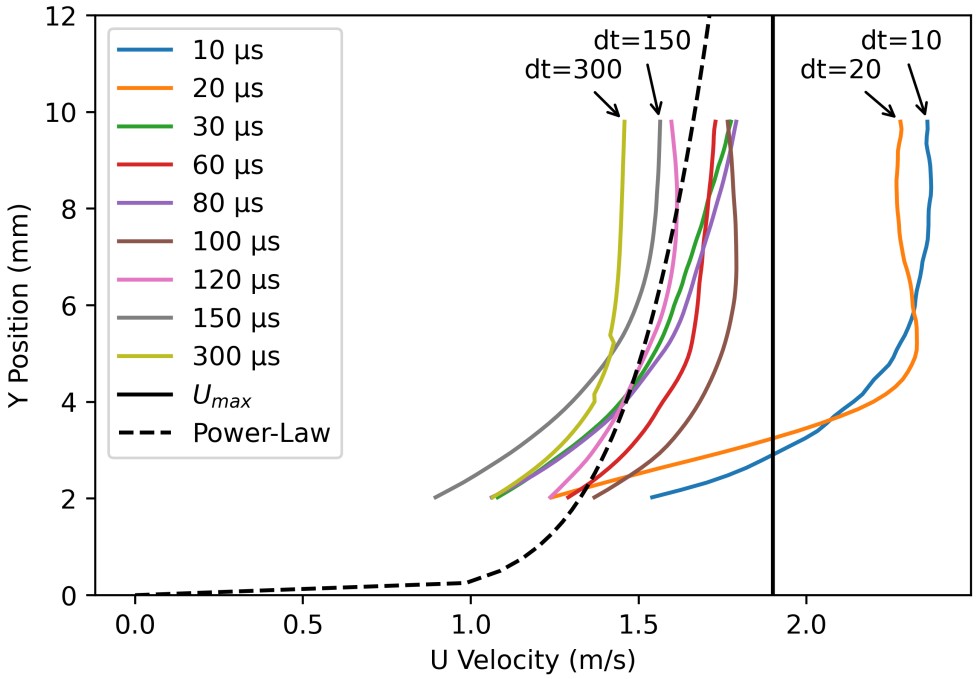

Figure 3.10 Crossflow average velocity profile as a function of laser pulse interval

A problem arises when the jet is added to flow, because its velocity can be as much as 50 m/s, causing a very large velocity gradient in the X-Y plane. A tradeoff must be made in order to capture the very fast jet exit velocity and the relatively slow crossflow simultaneously. To fix this, a first large δt in the range of 60 μs is used to study the wider slow moving crossflow field. This range will capture accurately the flow behavior in the range of 2 m/s that dominate the crossflow and jet wake mixing region. Another small δt in the range of 10 μs is used to resolve completely the exit of the fast micro jets. This timescale is also necessary to resolve the small fast instabilities in the range of $x/d = 0$ to 5. Practically, each experimental test case was repeated for δt values of 10, 20, 40 and 60 to ensure that each region of the flow field is resolved.

3.2.4 Vector field calculation algorithm

The algorithm employed to compute the instantaneous vector fields is provided by the commercial software LaVision Davis v8.4. The double frame high-speed recordings are used to determine of the displacement of the particle by applying a spatial cross-correlation function. The software was set up with the following instructions:

- Camera noise was removed by subtracting a raw picture of the illuminated rig test section.
- Particle intensity in the captured images I is normalized using a sliding window of 64x64 pixel to account for the two seeders with different flow rates and particle count profiles.
- To calculate the vector field, a multi-pass iterative PIV process was used, refining interrogation windows from 24x24 to 12x12 pixels with 50% overlap and orientation-aligned correlation cells.
- Spurious vectors were filtered using a median filter, and missing vectors were interpolated with cubic splines.
- Smoothing was not applied to the instantaneous velocity fields to preserve the original flow structures at the expanse of higher noize.

3.3 Image processing and analysis

This section describes how the raw images of the illuminated oil particles from the helium JICF were processed. The open source programming language Python is used throughout this research project for its robust library selection, ease of use and large community. Appendix B presents a novel Voronoi tesselation technique that can be useful in future research to measure seeded particle number density.

3.3.1 Average Pixel intensity technique

Inside the 2D imaging plane of the PIV setup, when only the jets are seeded, image pixel intensity I is used to infer jet seeded particle number density, used as a proxy for helium concentration. However, as demonstrated in previous studies [65], the relationship between particle number density and fuel concentration is non-linear when particle overlap is non-negligible; affecting the accuracy of fuel concentration estimations. Given the high particle

overlap near the micro jet exit, where particle number density peaks, this study focuses on large field of view measurements after the jet exit, to ensure more reliable particle number density estimations. Furthermore, the image pixel intensity I is normalized by its maximal value at the injector tip $I_{\max}$, and background noise is subtracted. The particle number density is thus related to the local fuel concentration c, with helium used in this case. Time-averaged images are produced by computing the pixel wise mean intensity $\bar{I}$, representing the normalized average particle count. This enables the use of existing images captured for PIV to measure relative particle number density, while simultaneously gathering velocity information within the plane.

3.3.2 Pixel intensity unmixedness

Local mixture variations over time are also quantified, using the unmixedness parameter U [66] defined in equation 3.8. Where $\bar{c}$ is the average normalized fuel concentration over time, as estimated through the approach described above based on particle number density, and c'^2 is its variance. $\bar{I}$ is the time averaged normalized particle signal intensity, and I'^2 is its variance.

$$U = \frac{c'^2}{\bar{c}(1-\bar{c})} \propto \frac{I'^2}{\bar{I}(1-\bar{I})} \tag{3.8}$$

The unmixedness term U quantifies the degree of non-uniformity in particle number density at a location and scales between 0 and 1. A value of 0 signifies complete homogeneity, indicative of optimal mixing, whereas a value of 1 denotes the greatest observed variance, highlighting a condition where pure fuel and oxidizer are sequentially observed in space and not mixed. The unmixedness is assessed across a plane that is aligned with the third micro jet, spanning the entire field of view. A grid of five pixels wide squares is numerically added to calculate the unmixedness in windows as large as the signal of a single illuminated particle.

3.3.3 Jet cross-section spread and Frequency analysis

To investigate the dynamic behavior of the jets in crossflow, the vertical spread of the jets was measured. Also, frequency analysis was performed on the time-series data of the tracked shear layer position over time.

Data preprocessing

Each grayscale image was read and cropped to focus on the region of interest, ensuring consistency across all frames. To isolate the jet regions from the background, a global threshold value T was applied to create a binary images:

$$M(x,y) = \begin{cases} 1, & \text{if } I(x,y) \geq T; \\ 0, & \text{Else} \end{cases} \tag{3.9}$$

where $I(x,y)$ is the pixel intensity at position (x,y). Contours of the jet regions were then detected using the `findContours` function from OpenCV. For each frame and each injector, the minimum and maximum vertical positions, $y_{\min}(t)$ and $y_{\max}(t)$, of the detected contours were recorded, yielding time-series data. The instantaneous vertical spread of the jet was calculated as:

$$\Delta y(t,x) = y_{\max}(t,x) - y_{\min}(t,x). \tag{3.10}$$

To prepare the shear layer position over time data set for frequency analysis, several preprocessing steps were applied:

- **Outlier removal**: Outliers in the $\Delta y(t)$ data were identified using the Z-score method with a threshold of 3. Outlier data points were replaced via linear interpolation between adjacent valid data points.
- **Smoothing**: A moving average filter was applied to reduce high-frequency noise:

$$\tilde{y}_{\max,i} = \frac{1}{N} \sum_{k=i-(N-1)/2}^{i+(N-1)/2} y_{\max,k}, \tag{3.11}$$

  where N is the window size, selected based on the flow rate to balance noise reduction and signal fidelity.
- **Detrending**: To remove very slow-varying trends of associated with jet fluttering and emphasize the oscillatory behavior, the smoothed data was detrended using a sliding window linear detrending over segments of 200 data points using SciPy.

Peak detection

Peaks in the detrended $\Delta y(t)$ data were detected using the `findpeaks` function from SciPy. The minimum peak distance parameter was adjusted dynamically based on the flow rate to account for changes in oscillation frequency, from 2 to 12 data points between them. The dominant frequency was estimated by counting the number of peaks n_{peaks} over the total duration $\Delta t = 0.1s$ of the 1000 recordings:

$$f_{\text{peak}} = \frac{n_{\text{peaks}}}{\Delta t} \tag{3.12}$$

Fast Fourier Transform (FFT)

For a comprehensive frequency analysis, the Fast Fourier Transform (FFT) was applied to the detrended $\Delta y(t)$ data using SciPy. Prior to performing the FFT, the mean of the signal was removed to center the data around zero, eliminating very low-frequency components that typically dominate at low Hz. To reduce spectral leakage, a Hann window was applied to the detrended signal $\Delta y_{\text{detrended}}(t)$:

$$\Delta y_{\text{windowed}}(t) = \Delta y_{\text{detrended}}(t) \cdot w(t) \tag{3.13}$$

where $w(t)$ is the Hann window function. The FFT was then computed as:

$$Y(f) = \mathcal{F} y_{\text{windowed}}(t) \tag{3.14}$$

where $\mathcal{F}\cdot$ denotes the Fourier transform. The frequency spectrum $|Y(f)|$ was analyzed to identify dominant frequencies.

3.4 Crossflow characterization

This section presents the pipe flow behavior, boundary layer thickness, and turbulence intensity within the crossflow channel. Figure 3.11 show a collection of crossflow velocity profiles as a function of downstream distance between $x = 0$ to $x = 80$ mm. It is captured with a zoomed-out view to analyze the entire flow behavior from the test section floor at $y/d = 0$ up to $y/d = 50$ mm, just below the ceiling boundary layer. The average velocity profiles are taken at the fastest possible crossflow velocity obtainable of at 2.5 m/s with the compressed air supply set to 100 psi. This view shows that the crossflow is fully developed in the test section where the JICF will be injected.

Zoomed-in averaged PIV measurements between $y = 2$ to $y = 10$ indicate that the turbulent crossflow boundary layer has an average thickness of $\delta_{95\%} = 8.1$ mm, yielding a large boundary layer to jet diameter ratio of $\delta/d \approx 10$. It also shows a turbulence intensity of 15%, based on the standard deviation of the crossflow velocity profile. This turbulence intensity is useful for boundary conditions in numerical works trying to replicate the present experimental results.

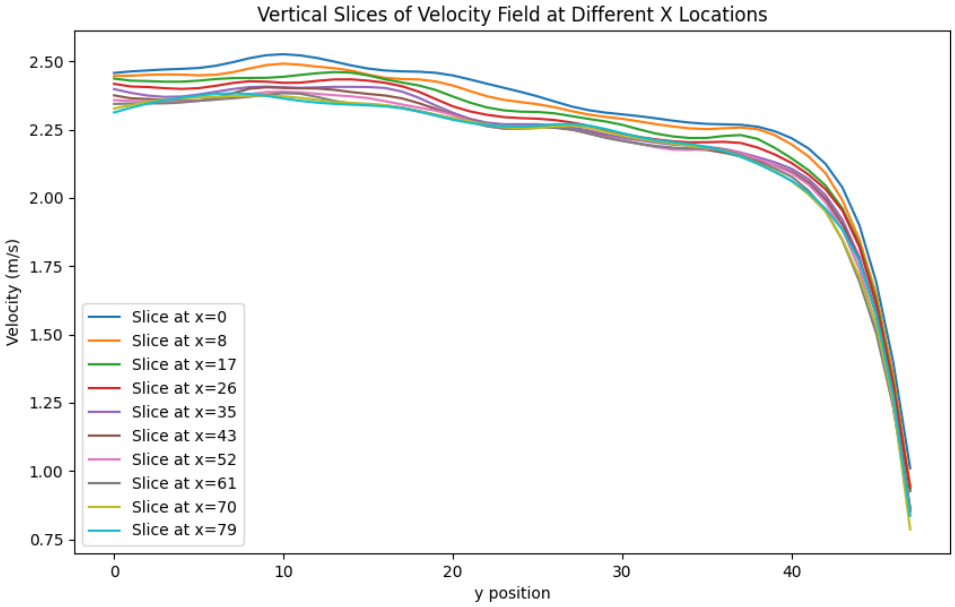

Figure 3.11 Crossflow boundary layer profile at 100 psi inlet pressure

Figures 3.12a and 3.12b present the average vector fields of the boundary layer, covering the region from $y = 2$ to $y = 10$ for two different time intervals, $\delta t = 50$ and $\delta t = 10$. These measurements were taken at the crossflow velocity of 2 m/s with the setup's compressed air supply setup to 80 psi. The results indicate a notable difference between the two time intervals. At the shorter interval of $\delta t = 10$, the vector field overpredicts the low velocities within the boundary layer, with values nearly 40% higher than those obtained with a properly chosen pulse interval $\delta t = 50$. This discrepancy confirms that very low δt values introduces inaccuracies in velocity measurement.

3.5 Test Matrix

Table 3.2 displays the main value of the non-dimensional parameters considered in the present work for a varying jet flow rate. The exit velocity is calculated based on an incompressible volumetric flow rate assumption. The jet Reynolds number is based on the jet diameter of

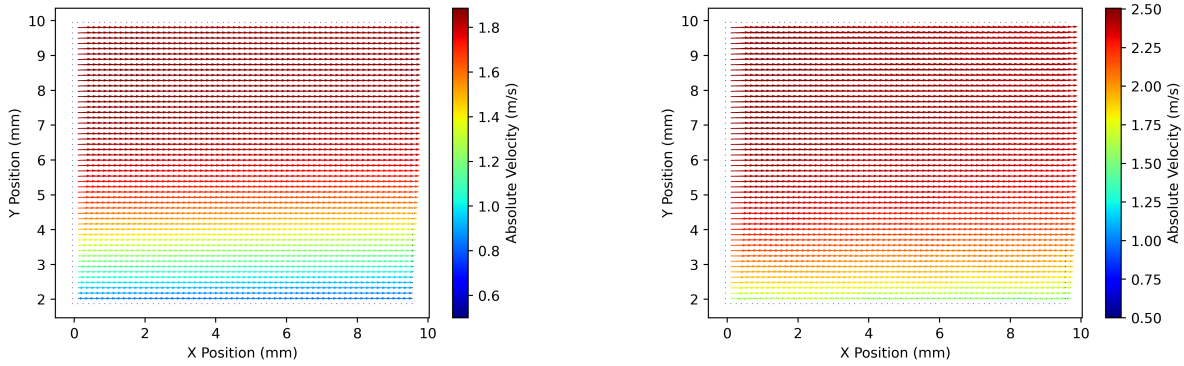

(a) (b)

Figure 3.12 Crossflow boundary layer PIV average vector fields at two time intervals, for (a) dt=50 and (b) dt=10 at 80 psi inlet pressure

0.8 mm and helium's properties. The jet-to-crossflow velocity ratio R is based on a 2 m/s crossflow velocity, and the momentum flux ratio J is based on a density ratio $S = 0.14$ These tests are repeated for a single jet case and three jet array geometries with spacing $l/d = 1.5$, 2.12, 5.25.

Table 3.2 Experimental Parameters for a constant crossflow of 2 m/s and a density ratio S of 0.14

Flow Rate (SLPM)	U_j**- Exit Velocity (m/s)**	Re_j**- Jet Reynolds Number**	**Velocity Ratio** R	**Momentum Flux Ratio** J	**Equivalent Velocity Ratio** R_e
0.5	2.1	15	1.0	0.16	0.39
1	4.1	30	2.1	0.62	0.79
1.5	6.2	45	3.1	1.4	1.2
2	8.3	60	4.1	2.5	1.6
2.5	10	75	5.2	3.9	2.0
3	12	90	6.2	5.6	2.4
3.5	15	110	7.3	7.6	2.8
4	17	120	8.3	10	3.2
4.5	19	140	9.3	13	3.5
5	21	150	10	16	3.9
6	25	180	12	22	4.7

The results from this experimental test campaign are analyzed and shown in the next chapter, in the form a scientific journal manuscript.

CHAPTER 4 RESULTS

The results of this study begin with a qualitative assessment of instantaneous coherent structures in the longitudinal (XY) and transverse (YZ) planes. This is followed by the effects of jet-to-jet spacing on trajectories, scaling, and jet spread. PIV measurements are then used to quantify the impact of array spacing on average velocity fields. Finally, an examination of shear layer instabilities in the transverse (YZ) plane as a function of array spacing concludes this work. The proof of concept preliminary study is shown is Appendix A, and a promising Voronoi cell technique is detailed in Appendix B to measure jet fluid concentration.

4.1 Evolution of instantaneous coherent structures

4.1.1 Jet visualization in the longitudinal (XY) plane

To visualize and understand the behavior of low-density jet arrays in crossflow, measurements are made in the xy longitudinal plane. This plane is helpful for examining the shear layer evolution of a single jet of the array, but does not capture jet-to-jet interactions. In this study, the illuminated jet is near the center of the array, counted from the camera: the fourth jet in an array of eight and the second jet in an array of four. Figure 4.1 shows instantaneous scattering intensity of the DEHS oil particles for varying momentum flux ratio J. In all cases, the laser sheet illuminates the center of the JICF, highlighting the circular laminar jet exit, shear layer evolution, its curvature as it encounters the crossflow, and occasionally the CVP rotating back into the frame below the shear layer. Images are presented at varying magnification levels with a constant aspect ratio to illustrate the evolution of instantaneous jet behavior in crossflow, allowing detailed observation of flow structures.

The instantaneous images reveal the evolution of coherent structures as the momentum flux ratio J increases for a single low density JICF. At a low momentum flux ratio of $J = 0.2$, the jet appears almost laminar and does not penetrate deeply into the crossflow boundary layer. Shear layer instabilities are barely visible, and the jet exhibits minimal mixing with the crossflow. Mixing can be defined qualitatively as a loss of coherence and predictability in shear layer position and scattering signal in time. This behavior is consistent with previous observations that low J jets in crossflow exhibit limited penetration [37]. Some instabilities form on the shear layer further downstream for the current low J cases. They resemble hairpin vortices because they do not fold and rotate unto themselves, as will be discussed in the next section. The emergence of these instabilities aligns with the findings of Sau and

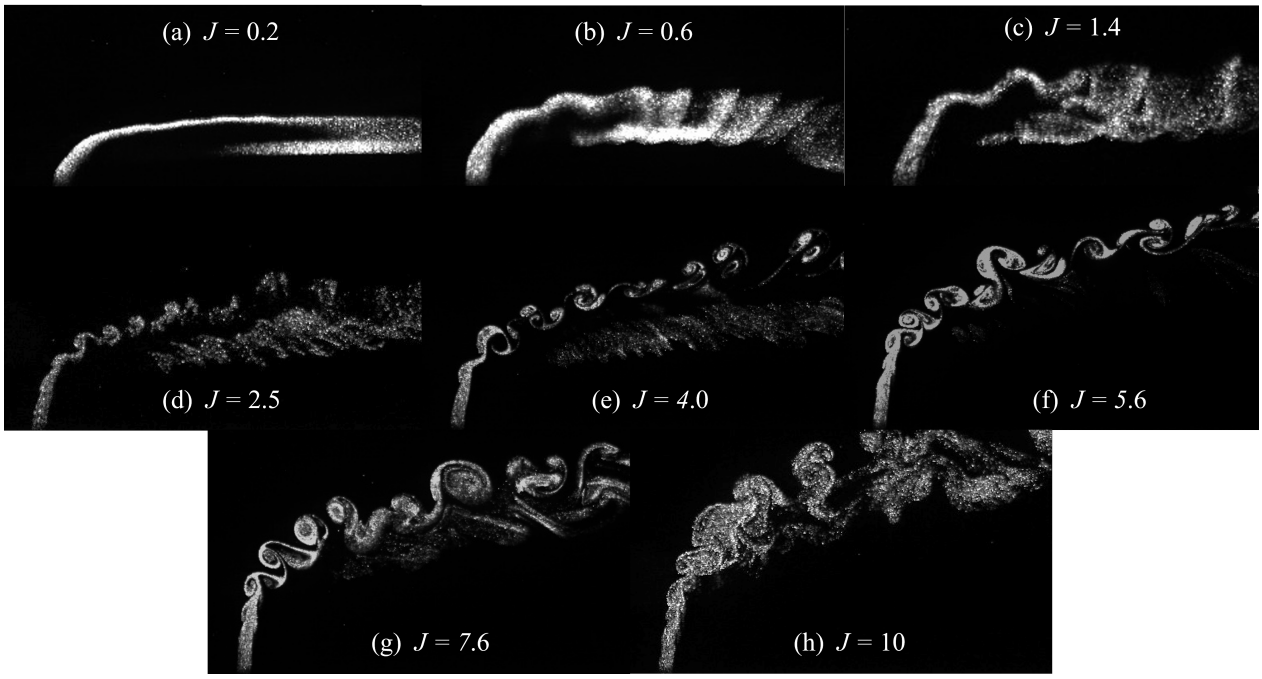

Figure 4.1 Instantaneous scattering images as a function of J for a single low density JICF

Mahesh [67] who observed the formation of hairpin vortices at low velocity ratios ($R \leq 1$).

As the momentum flux ratio increases to $J = 0.6$, shear layer instabilities begin to manifest in periodic fashion, with an amplitude of approximately 0.5 d. Although difficult to separate from shear layer vortices, CVP are forming and rotating below them, as will be shown in the next section. For $J = 1.4$, the amplitude of the oscillations in the shear layer increases to about 1 d, and mixing improves as the jet starts to break up and interact more effectively with the crossflow. The deeper penetration of the jet allows it to encounter faster-moving crossflow fluid enhancing the development of shear layer instabilities. Thus, for low density JICF, the initial development of shear layer instabilities begins for $J > 0.6$ and $R > 2.07$.

At higher momentum flux ratios, such as $J = 2.4$, strong regular rolling shear layer vortices start to appear with a spatial amplitude of approximately 2 d. These vortices are more coherent, folding onto themselves and rotating. A corresponding lee-side vortex pair is not always visible in these highly unstable JICF, as is visible in Figure 4.1 (e), where two top shear layer vortices progress consecutively downstream. This re-enforces the JICF model of Lim et Al. [42] and shows that the primary large-scale structures consist of loops.

For $J = 4$, the shear layer rolling vortices become stronger, exhibiting pronounced rotation from the faster exit velocity, and varying more in size along the streamwise compared to lower J cases. The amplitude of the vortices at $J = 4$ is approximately 3 d, and this trend

of increasing shear layer vortices size with higher momentum continues for $J = 5.41$, where the vortices maintain coherence. The increase in the jet Reynolds number and velocity contributes to the development of these larger vortical structures. This range of momentum flux ratio exhibits strongest global instabilities along the entire shear layer, with vortices remaining locked in coherent structures that resist breaking into smaller turbulent eddies. These globally unstable, self-excited vortices display remarkable coherence, allowing their evolution and growth to be tracked downstream across nearly the entire domain. These instabilities are very similar to Kelvin-Helmholtz type behavior, but for a curved, varying density shear interface. Kelvin-Helmholtz instabilities occurs due to velocity shear between a fluid interface, leading to wave-like disturbances that grow downstream. Rayleigh-Taylor instabilities can also be at play, because of the density difference at the shear interface. Similar observations have been reported in studies of jets in crossflow where higher momentum flux ratios lead to stronger shear layer vortices [40, 68].

When J is increased further to $J = 7.6$, the vortices vary in size, with the largest reaching up to 6 d. However, at $J = 10$, the vortices begin to dissipate and lose the coherence observed at lower J values. Turbulent mixing, denoted by a cascade and breakup in vortex size, becomes more apparent at these higher momentum flux ratios. The jet mixes more rapidly with the crossflow, and the rolling vortices are no longer as distinct. This behavior suggests that beyond a certain momentum flux ratio, the coherent structures break down leading to improved mixing but less organized flow structures. This is consistent with the previous observations [69], who showed that as the jet becomes more turbulent with higher velocity ratio, the coherent vortical structures diminish.

Finally, these high-speed recordings are repeated for the aforementioned jet array spacing geometries. Figure 4.2 displays the effect of jet array spacing on the instantaneous low density JICF images for $J = 3.75$. For a constant velocity ratio, it is clear that closely spaced arrays behave differently. With increased helium injection per crossflow area, the coherent structures from globally unstable oscillations break up more rapidly. Near the jet exit, instabilities and shear layer vortices are created in all jet spacing cases, however they seem to lose coherence faster when neighboring jets are present. This is believed to be caused by jet-to-jet interactions, which help break-up self-exciting modes. Lee-side shear layer vortices are also much less prone to form in arrays compared to the single JICF case. Another key visible impact of small array spacing is the increase in jet spread, visible in Figure 4.2 (b) and (c), where seeded oils particles appear closer to the test section floor compared to the single JICF case. These jet-to-jet interactions will be further visualized, quantified and discussed in the following sections.

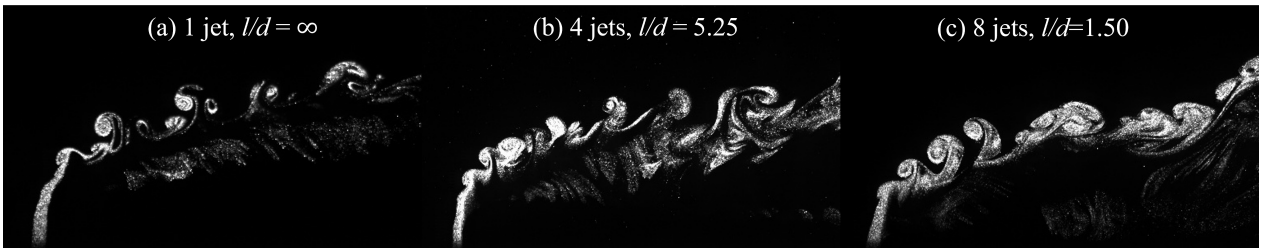

Figure 4.2 Instantaneous scattering images as a function of array spacing l/d for $J = 3.75$

4.1.2 Jet visualization in the transverse (yz) plane

The longitudinal plane of view cannot accurately portray jet-to-jet interactions as they merge and influence each other downstream. To this end, images are taken with the camera looking upstream through the exhaust of the rig, and the laser sheet illuminating transverse slices in the yz plane.

Figure 4.3 and 4.4 present instantaneous images of the seeded jets, highlighting the change in coherent structures at two different downstream positions x/d for various jet spacing and momentum flux ratio J. Figure 4.3 is located at $x/d = 2.5$, showing transverse plane structures for $0.6 < J < 9.62$. Further downstream at $x/d = 12$, Figure 4.4 highlights momentum flux ratios over the limited range $0.6 < J < 5.76$, as higher values leave the frame of view.

The first row of images (a to d) illustrates how the single jet evolves with increasing momentum ratio. For $J < 2.4$ and $x/d = 12$, the counter rotating vortex pair is the main flow feature and is clearly visible. It strongly curves onto itself and forms a complete revolution, similarly to the visualizations of Lim et Al. [42]. But at $x/d = 2.5$, the CVP does not have time to completely form, indicating that CVP vorticity increases with downstream distance. For $J > 2.4$, the CVP is less defined, showing DEHS particle intensity stratification over the shear layer instabilities, pointing to increased mixing. Amplitudes of the shear layer oscillations also start to increase, which is likely caused by increases jet momentum leading to more velocity gradient at the shear interface helping transition faster to completely formed shear layer vortices.

The second row of images (e to h) shows how the 4 jet array geometry separated by $l/d = 5.25$ evolves. Even for low velocity ratios ($J = 1.35$), jet interactions already are visible; for instance in image 4.4 (e) at $x/d = 12$, the right most jet's CVP pulls its neighboring jet's CVP "leg" into itself. This novel interaction is visible for many recordings where the CVP is strongly defined at lower J. The CVP of low density JICF being entrained into another

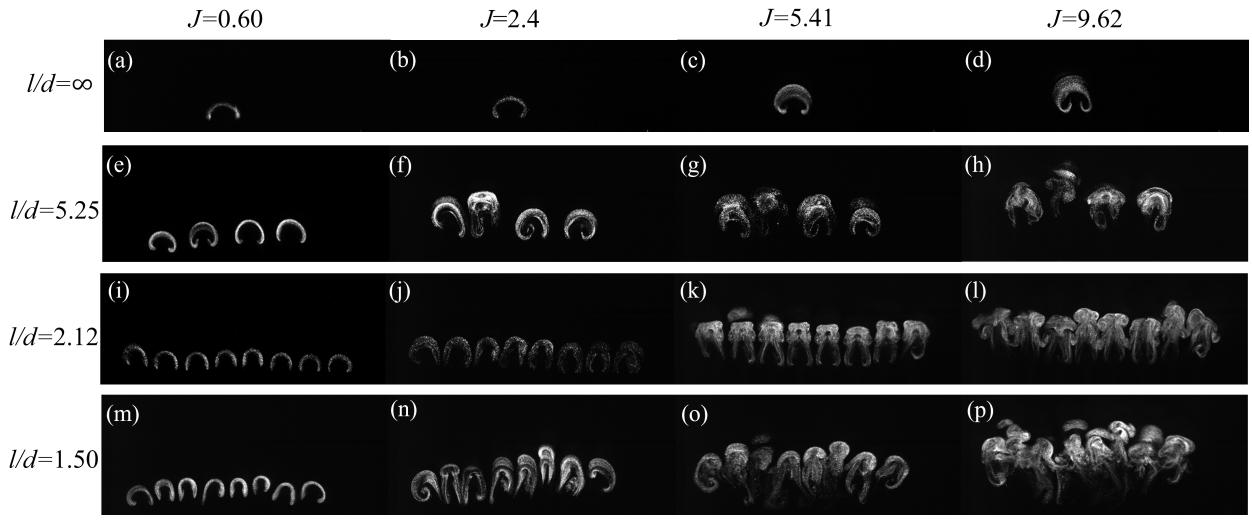

Figure 4.3 Instantaneous images transverse YZ plane scattering images evaluated at $x/d = 2.5$ as a function of array spacing l/d and J

jets CVP may lead to improve mixing and spread. Similar interactions are also visible for $J > 1.35$ cases, where each center jet is squeezed by its neighbor, stretching them vertically. Mixing already improves compared to the single jet cases, as more variance is added to the shear layer position and size.

The third row of images shows an array of 8 jets spaced by $l/d = 2.12$. For cases with $J < 2.4$, the globally unstable jets show clearly defined oscillatory modes where the peak amplitude is reached concurrently for all jets. This spacing is also characterized by the CVP "leg" not rotating under the jet center, but instead are stretched downwards. The exception to this are the jets at the extremity of the array who only have their exterior most CVP leg rotate. The interior legs remain more vertical as they are pinched between other jet wakes, compared the free exterior legs. This clearly indicates that neighboring jets affect the CVP mixing and momentum of others near them. Strong globally unstable frequency phase locking is visible in pictures (k), where the peak amplitude is reached simultaneously.

The last row of images displays the jet array spaced by only $l/d = 1.5$. Intense variance in jet position is visible, and jet behavior can quickly switch between injector, for example one might be on top of its neighbor, but stuck below it a few milliseconds after. Well-defined CVP below the jets are no longer visible. Similarly, shear layer instabilities, or periodic vertical oscillations, are present but less predictable, as interactions and mixing becomes stronger compared to the single jet case. With such small spacing, the flow behavior reminisces of a single wide slit injected into a crossflow. Local properties of each jet are less coherent, but two global CVP start to appear on both sides of the array in pictures (o) and (p), entraining

together the edge jets and rotating them towards the center of the array. This behavior further indicates that $l/d = 1.5$ is near a critical jet spacing value acting more as a wall in crossflow, especially for $J > 1.35$ when jet penetration is large.

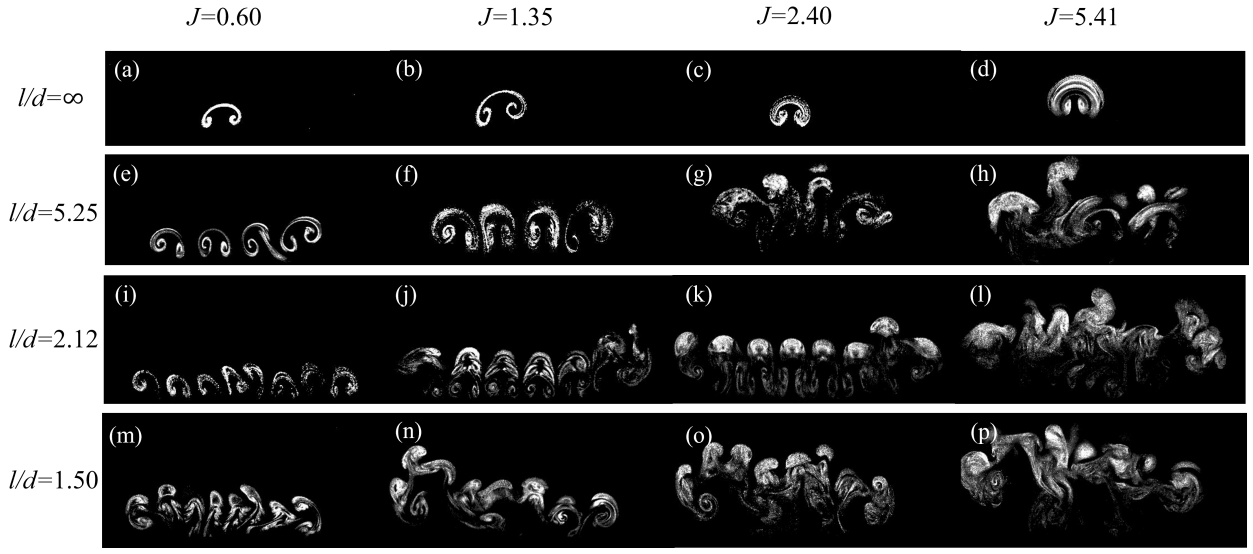

Figure 4.4 Transverse YZ plane scattering images evaluated at $x/d = 12$ as a function of array spacing l/d and J

To conclude on these transverse images, it is clearly visible that JICF turbulent mixing increases with smaller jet spacing and higher J. Tightly spaced arrays of jets help to reduce the flow structure coherence and suppress globally unstable modes faster due to the decreased predictability of vertical oscillation periodicity. Some novel jet interactions visible in these videos include a jet's CVP entraining its neighboring jet CVP into its own vortex rotation, and the size of the "legs" of a JICF increasing in length with decreasing jet spacing, hinting towards increased vertical spread.

4.2 Effect of jet-to-jet spacing on jet trajectories and penetration

By averaging 1000 instantaneous images of the illuminated tracer particles for a given test, the JICF trajectory centerlines can be approximated in the plane of interest. Regions inside the averaged image with higher pixel intensity denote higher seeded particle concentration or more frequent presence of particle-laden flow. This average image can then be used to compute the jet centerline, by taking the average location of the 10 brightest pixels for each x-axis pixel columns. Figure 4.5 illustrates the effect of jet-to-jet spacing l/d on the average particle laden JICF image in the longitudinal plane for $J = 5.41$. This analysis rests on

the hypothesis that seeded particle number density is proportional to helium concentration, which is realistic for the low Stokes numbers encountered. Consequently, it also assumes that the averaged pixel intensity is proportional to the local average particle number density. For a dilute particle field, light scattering can be considered proportional to the number density of particles [65], assuming each particle contributes a roughly equal amount of scattered light and consistent laser illumination.

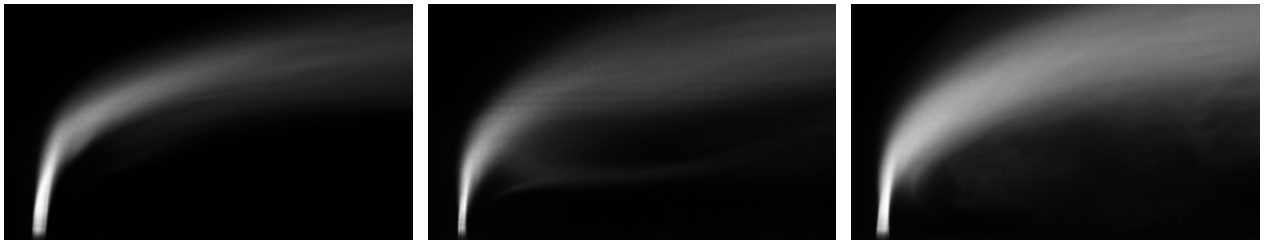

(a) (b) (c)

Figure 4.5 Time averaged JICF images for $J = 5.41$ (3 slpm) as a function of jet-to-jet-spacing: (a) single Jet, $l/d = \infty$, 4 jets, $l/d = 5.25$, (c) 8 Jets, $l/d = 1.50$

The positions of highest pixel intensity $I_{max}(x, y)$ of the images of Figure 4.5 are aggregated using Python's OpenCV library. A vertical line is constrained from $y/d = 0$ to $y/d = 0.2$ at the injector tip $x/d = 0$ to ensure constant initial conditions. Scipy's non-linear least-square function `curve_fit` from the optimization library [70] is used to fit a typical exponential JICF trajectory model $y/d = A(x/d)^B$ to the $I_{max}(x, y)$ cloud of coordinates, revealing the unknown constants A and B.

Figure 4.6 shows jet centerlines calculated based on the aforementioned technique and illustrates the centerline trajectories for different momentum ratios J. No significant difference in jet centerline trajectory was found as a function of jet-to-jet spacing within the error range. This finding suggests that jet-to-jet interactions do not strongly affect the average centerline trajectory under these conditions.

In some low velocity ratio cases, the CVP is illuminated below the shear layer, resulting in the average maximal pixel intensity position being located at the CVP rather than on the shear layer, causing the centerline to shift downward. To address this, the jet trajectory model is constrained to prevent regression in the y-direction beyond $x/d = 1$ for $J < 1$. The shaded error bars were calculated based on the standard deviation of the brightest pixel positions at each x position, as well as the standard deviation of the residual between the fitted curve and the pixel positions.

To identify which non-dimensional parameter has the most influence on the trajectory of

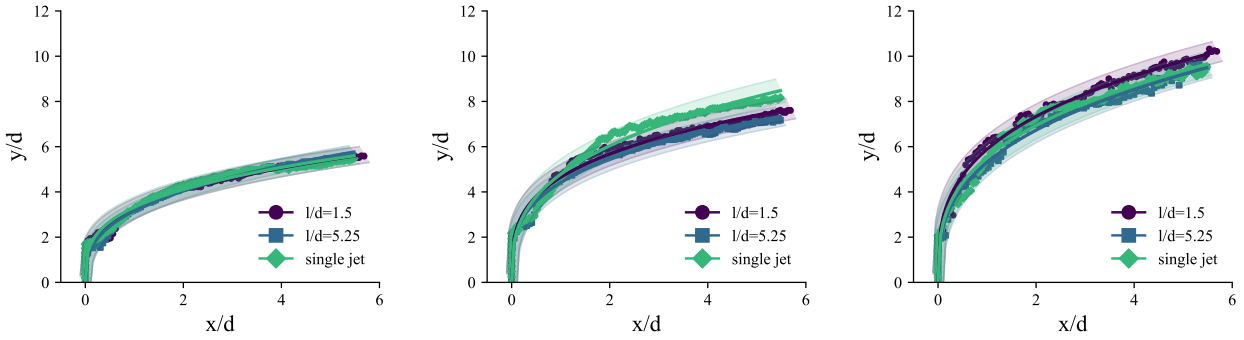

Figure 4.6 Low density JICF tracer particle centerline trajectories as a function of jet-to-jet spacing for (a) $J = 1.35$, (b) $J = 3.75$ and (c) $J = 7.37$. Symbols are data and curves are the least square fits. Shaded zone represent curve residuals and data standard deviation

the low density JICF particle centerline, the position (x, y) is plotted and normalized by the jet diameter d, the product of the momentum flux ratio and diameter Jd, and the velocity ratio multiplied by the jet diameter Rd. Figure 4.7 illustrates the trajectories scaled by these methods for a range of flow rates equivalent to $J = 0.2$ to $J = 9.41$ and an array of four JICF spaced by $l/d = 5.25$. The trajectories themselves are not recalculated for each normalization method; instead, only the axis scales are adjusted accordingly. Given that array spacing has minimal effect on JICF trajectory, the results of the four jet array spaced by $l/d = 5$ are used for further trajectory scaling discussions.

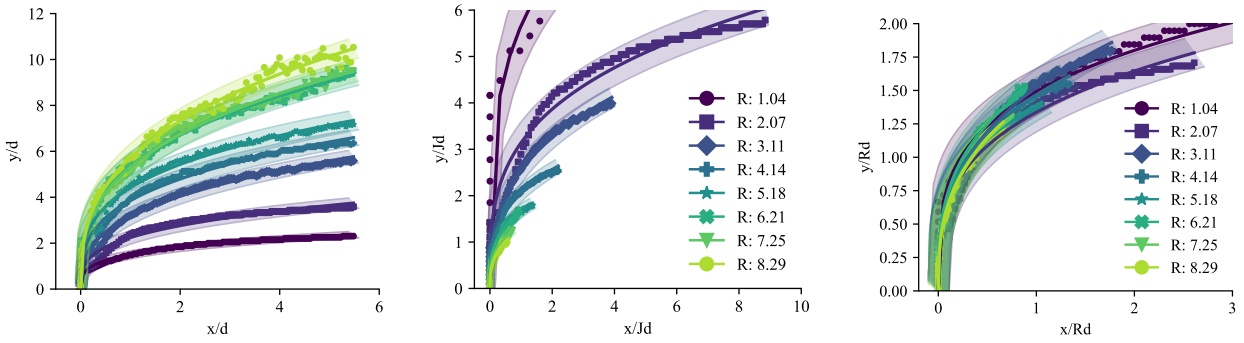

Figure 4.7 Scaling of low density JICF tracer particle centerline trajectories using (a) non scaling, only d, (b) Jd scaling and (c) Rd scaling for a jet-to jet spacing $l/d = 5.25$

Figure 4.7a shows that scaling with d alone does not collapse the trajectories; as expected,

jets with larger jet-to-crossflow velocity ratios penetrate deeper into the crossflow. Scaling with the momentum ratio Jd, depicted in figure 4.7b, does not significantly improve the collapse of the trajectories. For $J \leq 2.40$, the data appear artificially higher, suggesting over-normalization at low momentum ratios; for $J > 2.40$, trajectories are injected lower, indicating under-normalization at high momentum ratios. This suggests that, for a constant density ratio, scaling with Jd does not adequately account for the quadratic definition of the momentum ratio $J = SR^2$, generating large difference between low and high J cases across the flow conditions considered here. Based on this, when the density ratio is varied, the square root of the velocity ratio $\sqrt{J}$ should be used to scale trajectories in the near field.

In contrast, scaling with the velocity ratio Rd, presented in Figure 4.7c, produces a strong collapse of the trajectories across various flow rates. This phenomenon is consistent for all four array spacing studied here between $l/d = 1.5$ and $l/d = \infty$ at constant $S = 0.14$. This implies that jet penetration and trajectory shape are predominantly governed by the velocity ratio, even for arrays of low density, microscale JICF. Additionally, the average trajectory shows a linear increase in penetration depth with R; however, when jet momentum is enough $J > 4$ to reach $y/d > 8$, this increase in height becomes less rapid. This is believed to be caused by the fully developed crossflow having more momentum above the boundary layer.

The velocity ratio R emerges as the more appropriate non-dimensional parameter for scaling the present low-density JICF array trajectories in the $x/d = 20$ domain. These results align with standard single JICF trajectory scaling reports in the literature [68, 71, 72], leading to the following trajectory equation:

$$\frac{y}{Rd} = A(\frac{x}{Rd})^B \tag{4.1}$$

To examine the values of the constants A and B for arrays of low-density, microscale JICF, the data was fitted again using Rd and Jd scaling. The pre-exponential term A of the trajectory model is shown in Figure 4.8a as a function of jet flow rate and scaling method. The effectiveness of the Rd scaling compared to Jd is further supported in this analysis. The value of A remains approximately constant at around 1.6 across all jet flow rates, indicating consistent trajectory behavior regardless of jet flow rate. This consistency of A suggests that scaling with Rd successfully normalizes the influence of varying jet velocities, pointing to self-similarity of the jet trajectories. Trend line equations for A against jet flow rate $\dot{V}$ in SLPM are, for d scaling: $A = 1.242 \cdot \dot{V} + 1.128$, for Rd scaling: $A = 0.046 \cdot \dot{V} + 1.338$ and for Jd scaling: $A = 0.385 \cdot \dot{V}^2 - 2.61 \cdot \dot{V} + 5.77$. The linear term for Rd scaling is near zero, indicating good collapse of the data. Thus, for the aforementioned trajectory model, the value of $A = 1.43 \pm 0.09$ is proposed for arrays of low density micro JICF, when scaled by R.

Along all the trajectories, the exponential term B showed little variation as a function of array spacing and scaling method, as is shown in Figure 4.8b. It has an average value of $B = 0.320$ and a standard deviation of ± 0.040. A slight linear increase in B as a function of velocity ratio is noticed for all jet-to-jet spacing. This may be caused by the faster crossflow velocity at higher y/d positions above the boundary layer, causing a need for trajectory compensation. This value aligns with single JICF literature values [30], further indicating that $B = 1/3$ is a reasonable approximation.

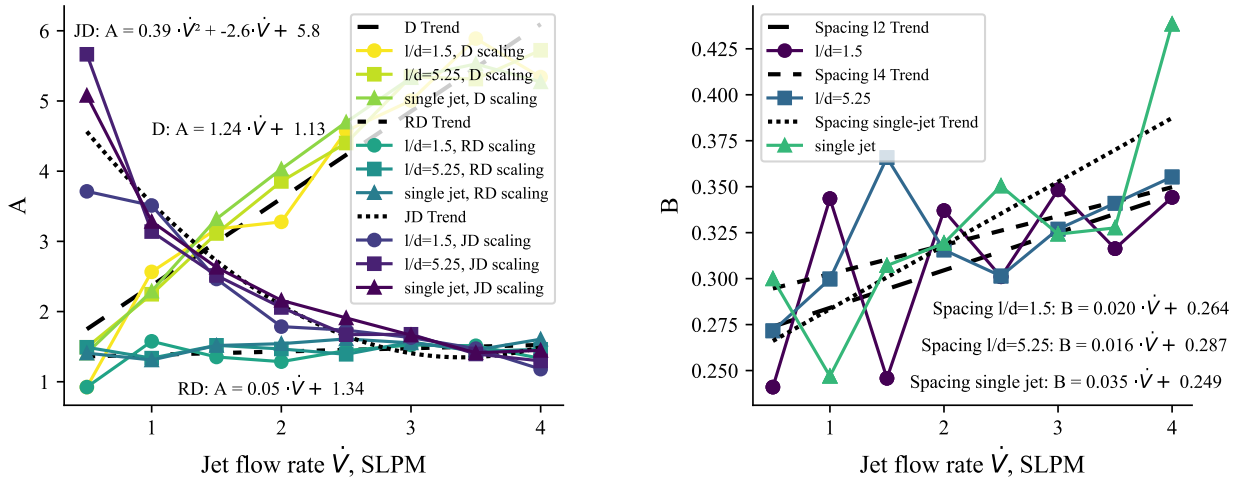

(a) Constant A

(b) Constant B

Figure 4.8 Trajectory model constants A and B from least-square fit for d, Jd and Rd scaling of low density JICF tracer particle centerline trajectories for a jet-to jet spacing $l/d = 5.25, 2$ and ∞

Therefore, the results demonstrate that the velocity ratio $R \propto \sqrt{J}$ is the most influential non-dimensional parameter in modeling low-density JICF array centerline trajectory behavior. It provides the best collapse of the data, enabling a generalized representation of the jet trajectories across many flow conditions. For a fixed low density ratio of $S = 0.14$, modeling jet array trajectories is best done with R scaling using constants $A = 1.43 \pm 0.09$ and $B = 0.320 \pm 0.040$.

4.3 Effect of jet-to-jet spacing on tracer particle mixing and spread

4.3.1 Jet spread as a function of array spacing in the longitudinal XY Plane

The averaged images shown in Figure 4.1 are employed to evaluate the streamwise evolution of the pixel intensity profile perpendicular to the jet centerline. This is used as a proxy to investigate mixing of the injected helium along the axial direction. In Figure 4.9a, the centerline is overlaid onto the time averaged JICF image, and perpendicular lines are drawn at regular intervals of approximately 1/3 d along the axial direction. For each perpendicular line, the pixel intensity profile is extracted and fitted with a Gaussian curve, as shown in Figure 4.9b, where the dotted lines indicate the raw pixel intensities and solid lines represent the Gaussian fits. The Gaussian fit provides a means to quantify the jet's spread by measuring the width of each profile. The standard deviation, σ, of the Gaussian profile is used as a measure of the characteristic width (spread) of the illuminated JICF center plane.

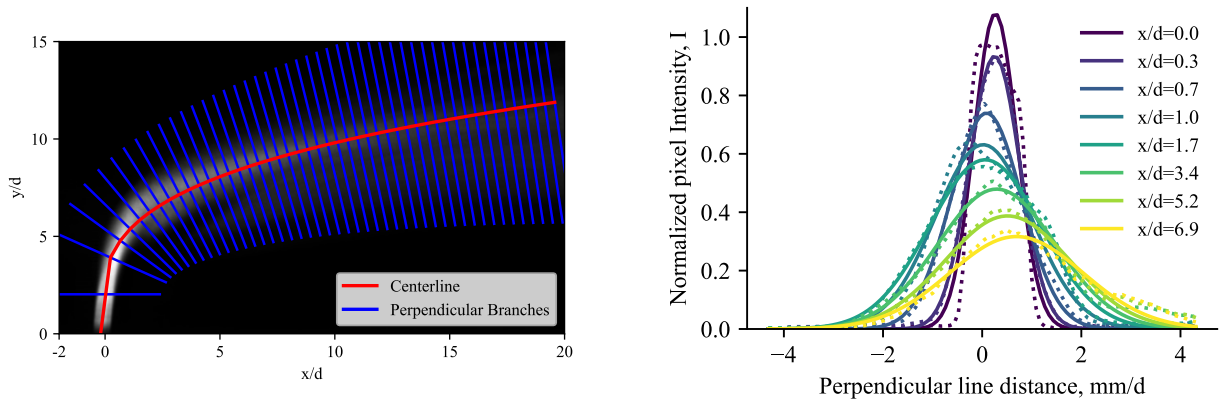

(a) (b)

Figure 4.9 (a) Averaged image with fitted centerline and perpendicular lines and (b) the Gaussian distributions adjusted to the intensity profile along the lines perpendicular to the jet for a single JICF at $J = 5.41$. Dotted lines indicate the raw pixel intensities and solid lines represent the Gaussian fits.

To remain above the low intensity laser sheet region near the test section floor, the first perpendicular line is manually lifted 25 pixels upwards. Also, the peak of the fitted Gaussian curves are not always perfectly centered around 0 on the perpendicular line axis. The is because the centerline trajectory is modeled with a least-square fitted exponential function that does not coincide with the most bright pixel at any given downstream distance. It

is worth noting that the jet spread observed in these cases could also be influenced by instabilities and crossflow turbulence, making the illuminated region sometimes quickly leave the imaging plane. This, along with the frequent illumination of the counter-rotating vortex pair (CVP), can cause variability in perceived jet thickness especially at $J < 1$. This is visible in Figure 4.1 (a, b, c) where to CVP is illuminated when rotating back below the shear layer in the center plane. As a result, the intensity profile sometimes deviates from a single Gaussian curve fit, exhibiting a bimodal distribution. Only the first peak, generated by shear layer vortices, is taken into account.

The widths of the Gaussian curves are plotted as a function of downstream position in Figure 4.10, for arrays of 1, 4 ($l/d = 5.25$) and 8 jets ($l/d = 1.50$) at two different momentum ratios, $J = 3.75$ and $J = 5.41$. As the jet-to-jet spacing decreases, the jets in crossflow become wider for a given axial position. The same behavior is seen in Figure 4.3 for $J = 5.41$, where the instantaneous cross-section of the JICF spreads lower in the y direction for closer array spacing. It is interesting that the spacing of the jet arrays only strongly affects the spread in the near field (x $\lessapprox 2.5d$) for the flow conditions presented. Growth after this point is dampened and increases steadily, reminding of the decreasing mixing efficiency branching point [39]. Specifically, for both subfigures 4.10 (a) and (b), the single jet ($l/d = \infty$), has consistently a width of approximately 50% lower than the jets spaced by $l/d = 5.25$, and almost 60% lower than 8 jets spaced by $l/d = 1.50$. The increased interaction between jets and crossflow blockage caused by closer jet-to-jet spacings result in a broader jet in the longitudinal plane. These measurements are obtained on the center array jet, flanked by tightly spaced neighboring jets on both sides, which restricts it to more readily spread in the vertical direction. These results indicate that smaller jet array spacing broadens the jet flow as it propagates downstream, which could enhance the mixing efficiency. This spreading phenomenon is believed to correctly represent JICF array spread for momentum ratios above $J > 1$. Under that value, jet spread and mixing is less pronounced and jet spacing has significant effect only further downstream when plumes collide.

Overall, this analysis showed that reduced jet-to-jet spacing enhances the spread of jets in crossflow in the longitudinal plane. This analysis is consistent with the instantaneous JICF cross-section evolution detailed in section 4.1.2, who showed a loss of coherence and growth of the CVP leg size as a function of array spacing. When designing hydrogen fuel injectors, this result can be used to increase fuel spread, for instance by discontinuous arrays of a few closely spaced micro holes.

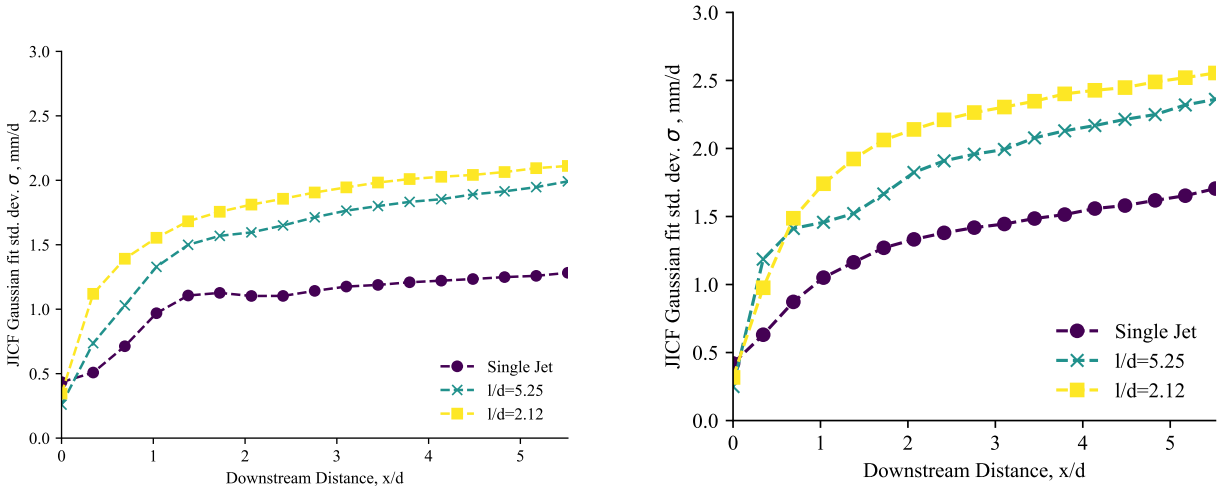

(a) (b)

Figure 4.10 Longitudinal spread of a JICF modeled with a Gaussian fit as a function of downstream distance x and jet-to-jet spacing for (a) J=3.75 and (b) J=5.41

4.3.2 Jet spread as a function of array spacing in the transverse YZ Plane

To quantitatively analyze the evolution in space and time of the JICF, each of the 1000 image obtained at 10 kHz acquisition frequency are processed with OpenCV. The illuminated jet regions are identified where the threshold value respects $I(x, y) \geq 0.15 \cdot I_{max}$. Contours of the jet regions are then detected using OpenCV's `findContours` function around the binary mask obtained. For each frame and jet, the minimum and maximum vertical positions $y_{\min}(t)$ and $y_{\max}(t)$ are recorded, as shown in Figure 4.11 yielding time-series data. The instantaneous vertical spread of the jet is calculated as: $\Delta y(t, x) = y_{\max}(t, x) - y_{\min}(t, x)$ and its time average span $\overline{\Delta y}$ is taken across all 1000 images.

Figure 4.12 illustrates the typical evolution of time averaged jet cross-section size $\overline{\Delta y}$ as a function of two momentum ratios equivalent to $R = 3.11$ and 6.21 and four jet array spacing. The error bars represent the standard deviation of the average Δy value over time. Velocity ratios larger than $R > 7.25$ cannot be analyzed with this metric, as their top most position is higher than the camera frame of view and were removed. Across all array spacing, an increase in momentum ratio J leads to a rise in average jet vertical spread, which is expected as high J penetrate deeper, increase turbulence generation and inject more jet fluid per unit time into the crossflow; leading to larger CVP and shear layer vortices. Also, jet spread almost always increases with smaller array spacing, as is shown in Figure 4.12 where a trend between spacing and jet spread is visible, especially when comparing the single jet to arrays. For a

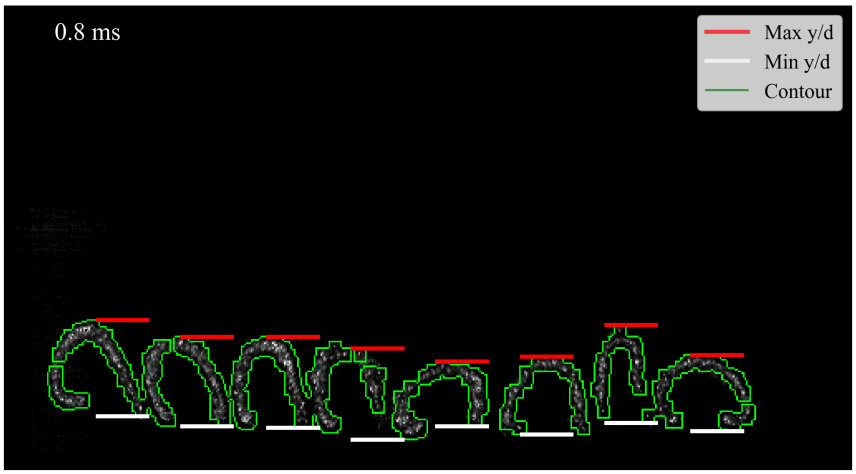

Figure 4.11 Instantaneous contour in the z-y plane for the $l/d = 2.12$ array at the downstream position $x/d = 2.5$ and for momentum flux ratio $J = 1.35$

single JICF, the highest measured size of the CVP is $\Delta y/d \approx 7.3$ for $J = 7.37$, compared to the tightly spaced array of $l/d = 1.5$ having a CVP height of almost $\Delta y/d \approx 13.1$. As the jets get closer to each other, lateral space is diminished, restricting the jets to spread more in the vertical plane compared to single JICF cases. Smaller spacing also increases crossflow blockage, as will be demonstrated in the following section. This in turn creates a low dynamic pressure, low velocity zone below the shear layer. It is believed that this zone also impacts the Counter-rotating vortex pair (CVP) downward spread.

Figure 4.13 shows the normalized crossflow vortex pair (CVP) spread along the downstream position x/d for varying jet array spacings. The spread $\Delta y/(R \cdot d)$, normalized by the velocity ratio R, is plotted as a function of x/d to illustrate the influence of downstream distance and array configuration on the vortex size development. Each subplot corresponds to a different jet array spacing, with individual data points representing various velocity ratios. The black dashed line in each subplot indicates the best-fit power law model, $\Delta y/(R \cdot d) = m \cdot (x/d)^n$, where m and n are empirically derived coefficient optimized for each spacing using SciPy. This normalization allows direct comparison of spread behavior across configurations and highlights the extent of CVP vertical spreading as a function of array spacing position.

As shown in Figure 4.13, the low momentum ratio cases with $J < 1$ (or equivalently $R < 2.5$) do not collapse effectively under the scaling $\Delta y/(R \cdot d)$. This indicates that the dynamics of low-momentum arrays of JICF differ significantly from those of higher-momentum cases. A likely explanation is the absence of oscillations at these lower momentum ratios, which alters the global behavior of the low-density JICF, leading to deviations in spread that make

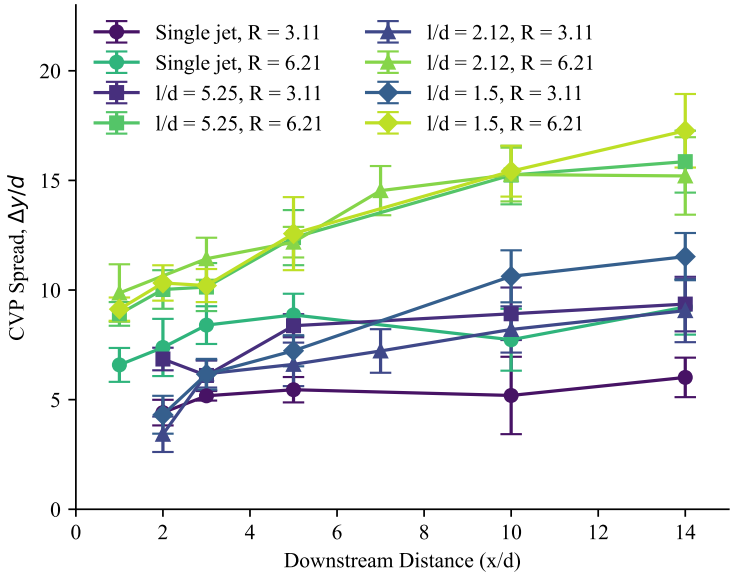

Figure 4.12 Comparison of the CVP spread along downstream position x/d for different jet array spacing and for velocity ratios $R = 3.11$ and 6.21.

the $R \cdot d$ normalization less effective. Furthermore, the fitted power-law models reveal a trend in the exponential term that depends on jet array spacing. For instance, we obtain $\Delta y/Rd = 1.21 \cdot (x/d)^{0.15}$ for a single jet, but for a four-jet array, this changes to $\Delta y/Rd = 1.68 \cdot (x/d)^{0.19}$, indicating a higher empirical exponent. Similarly, for arrays with eight jets at reduced spacing, we observe $\Delta y/Rd = 1.44 \cdot (x/d)^{0.28}$ for $l/d = 2.0$ and $\Delta y/Rd = 1.38 \cdot (x/d)^{0.30}$ for $l/d = 1.5$. These increased exponential constants suggest that tighter array spacing enhance vertical spread of the counter-rotating vortex pair (CVP). It also highlights a clear shift from single jet behavior to arrays of jets. This effect intensifies the JICF vertical spread.

4.4 PIV Velocity Fields

A typical velocity vector fields is presented in figures 4.14 for four jet-to-jet spacings (l/d) and for a velocity ratio of $J = 3.9$. The velocity fields were recorded at 10 kHz and averaged over 2000 images. The first 1000 images were captured with a $\delta t = 10$ μs to accurately resolve the jet exit velocity, though this comes at the cost of introducing around 15% over estimation error in the crossflow velocity measurement. The next 1000 images were recorded at $\delta t = 40$ μs, which allows for better accuracy in capturing the crossflow and the recirculation zone behind the jets. Although this methodology introduces some limitations, it provides a strong global representation of the velocity field. The flow fields are normalized by the crossflow

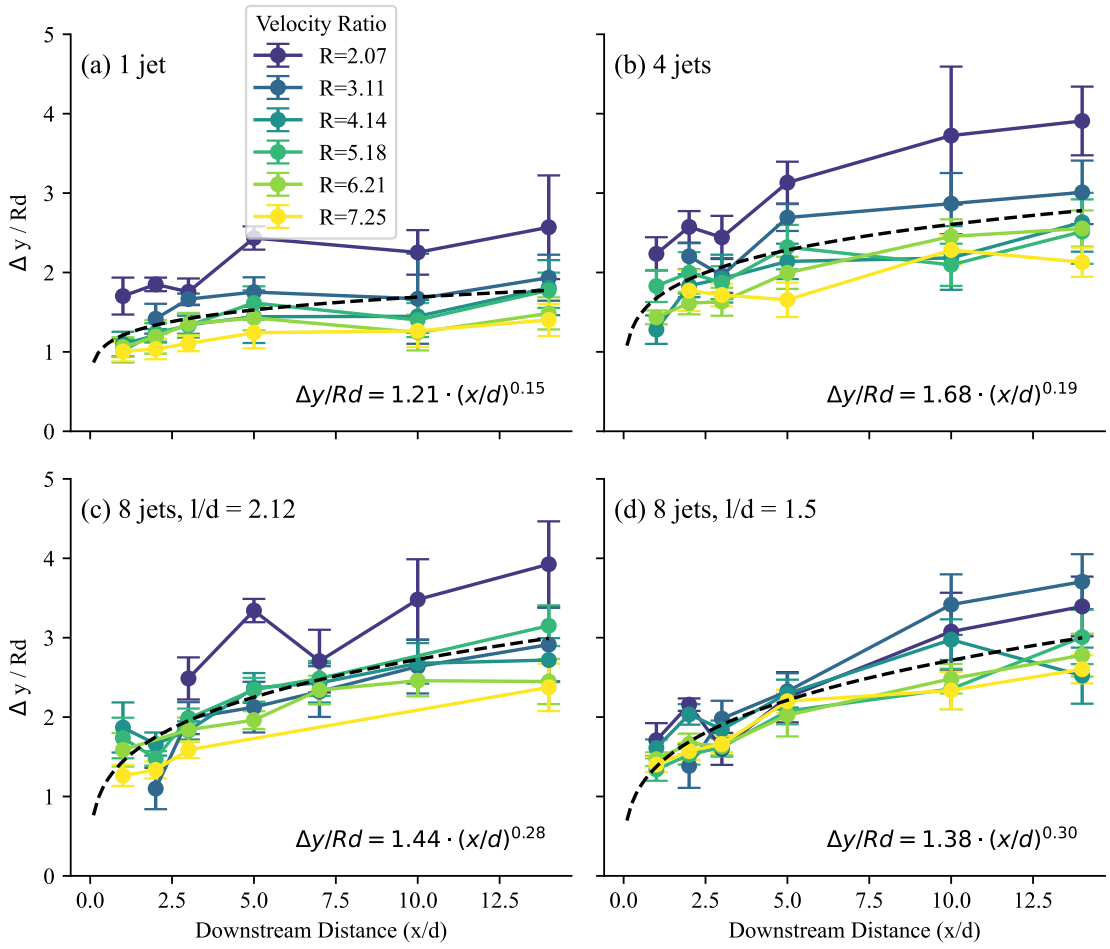

Figure 4.13 CVP spread normalized by the velocity ratio R along downstream position x/d for different jet array spacing and their fitted power model

velocity, which is approximately 2 m/s, and cropped at 99% of the velocity population to remove high value outliers and maintain a consistent color map across all cases. The color map represents the absolute velocity magnitude, calculated as $\sqrt{u^2 + v^2}$.

The jet velocity decreases significantly as it enters the crossflow, which is expected based on the low momentum of the helium jets. However, the PIV vector fields do not capture the theoretical jet exit velocities derived from volumetric flow rates. This discrepancy may be attributed to a too large laser pulse interval δt value or laser sheet thickness, but is believed to be primarily due to the interrogation window size to jet exit diameter ratio of 3 windows per mm, enabling two resolved vectors at the jet exit in a perfect case. This is not enough to verify the exit parabolic profile, but is helpful to look at the effect of jet spacing downstream of the array. When analyzing the effect of jet-to-jet spacing on the velocity field for a given J, a low-velocity zone is clearly visible behind the jets, indicated by darker blue regions in

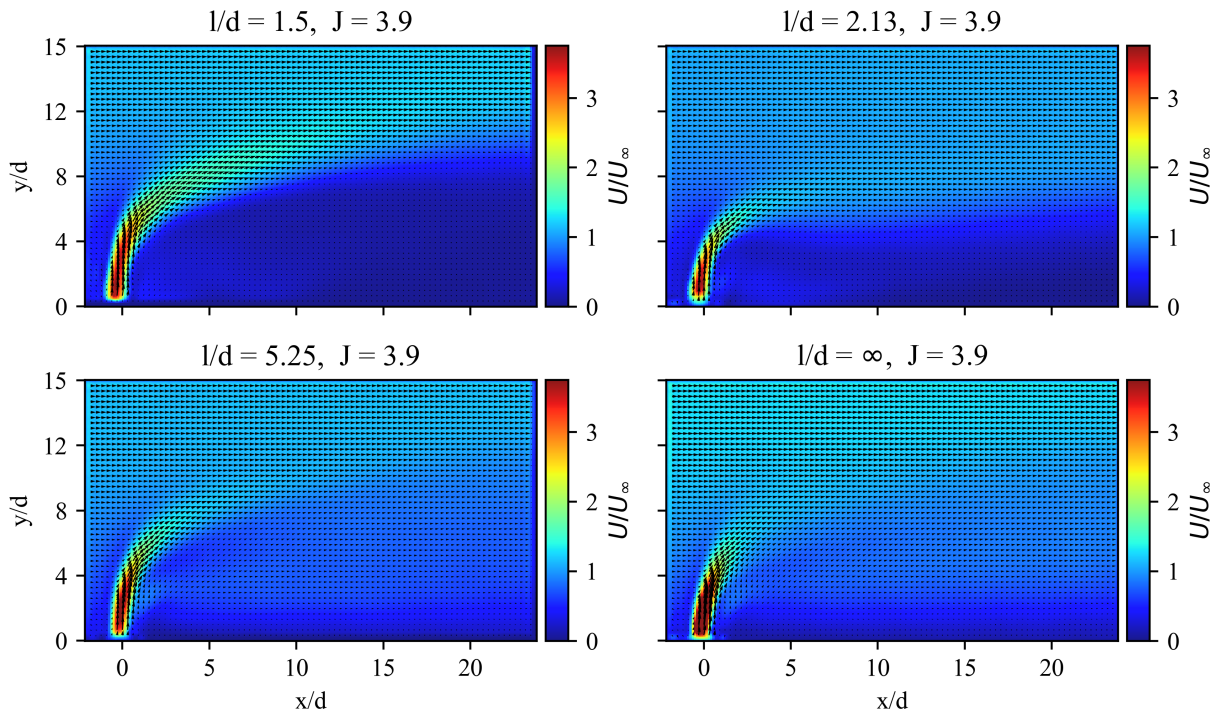

Figure 4.14 Average PIV vector field for four jet-to-jet spacings at J=3.75

the color map. This is prompting the need for recirculation zone analysis to quantify the effect of jet spacing l and momentum ratio J on the blockage effect behind the jet array

Figure 4.15a shows the average axial velocity profiles $\bar{u}_x$ at variable positions downstream of the closely spaced array of 8 jets. The error bars represent the unsteady axial velocity component u'_x measured with the PIV system. Below $y/d = 5$, a prominent flow reversal zone where $\bar{u}_x < 0$ is observed and persists further downstream. In this case, the crossflow is unable to reattach effectively behind the jets, leading to a larger and sustained recirculation zone. Even three diameters downstream of the jet array, the average $\bar{u}_x$ velocity remains close to zero, indicating that the crossflow cannot overcome the blockage imposed by the closely spaced jets and is unable to push the recirculation zone downstream. The velocity profile persists to be near zero until $x/d > 10$, where the crossflow begins again to add momentum below the JICF array fluid.

In contrast, the single jet case shown in Figure 4.15b, exhibits a different behavior. Directly behind the jet $\bar{u}_x$ is negative, but quickly returns to positive values as the crossflow reattaches and inhibits the formation of the recirculation zone. This reattachment of the crossflow after $x/d > 2$ helps reduce the size of the flow reversal region, which diminishes more rapidly compared to the case with multiple jets. Figure 4.15b exhibits stronger velocity standard

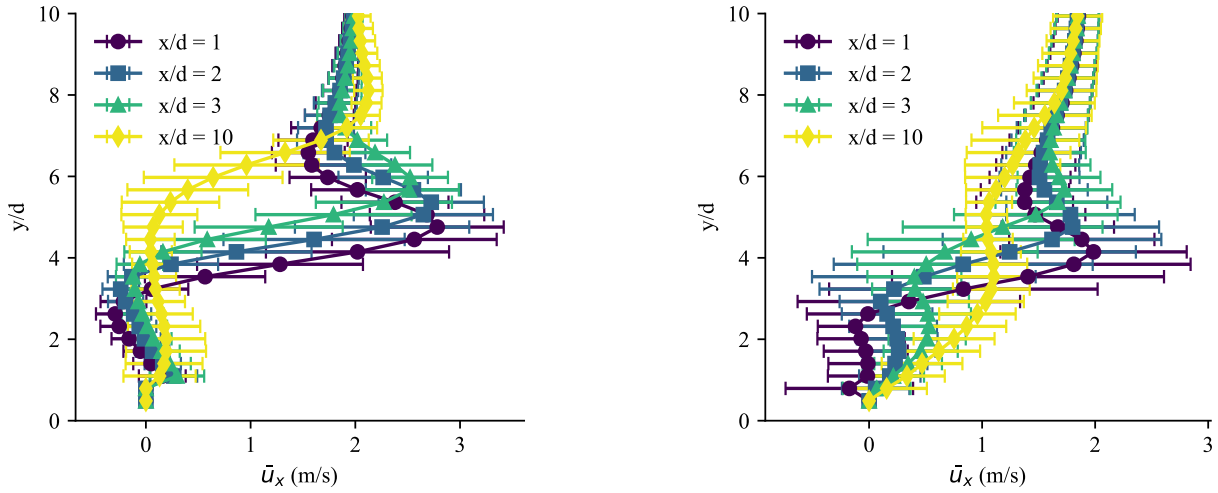

Figure 4.15 Comparison of u_x velocity profiles against downstream position, for (a) 8 jets, $l/d = 2.1$ and (b) Single jet, $l/d = \infty$ highlighting the flow reversal behind tightly spaced jets. Error bars represent u'_x and the PIV error

deviation compared to the array of jets. This is believed to be caused by all around faster flows near the micro injector; causing more disturbances.

Figure 4.16a shows a representative recirculation zone highlighted in red behind the jet, where the velocity is lower than 0.05 m/s. PIV recordings at intervals of $\delta t = 40$ μs are used to resolve the recirculation zone, because the area of interest is not the jet exit, but behind it. To assess the impact of jet array spacing on the extent of the recirculation zone, its area is calculated as the sum of the area of all PIV vector field grid cells where the velocity is 2.5% of the crossflow velocity (0.05 m/s). This method allows for a quantitative comparison of the size of the recirculation zone for different jet flow rates and jet-to-jet spacings, as shown in figure 4.16b. To ensure that the observed behavior is not simply caused by the u_x threshold value, a parametric study was done with values ranging from 0.01 to 0.2. Although the area size varied, the trend remained similar as a function of jet spacing and flow rate.

The results demonstrate that as the jet velocity increases, the recirculation zone area grows as faster jets penetrate deeper creating a shielding effect behind them. The single jet and cases with $l/d = 2.12$ and $l/d = 5.25$ spacing do not show significant differences in recirculation area. This suggests that the crossflow is able to go around the individual jets of the array preventing the formation of large recirculation zones. However, a marked increase in the area of the recirculation zone size is observed for the 8 jet array of $l/d = 1.5$ spacing.

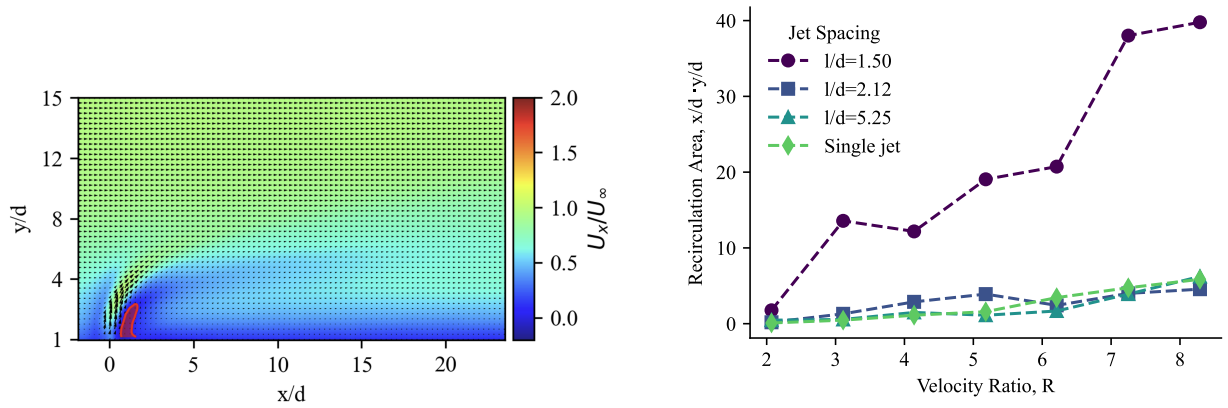

(a) Highlighted recirculation zone

(b) Size of all recirculation zones

Figure 4.16 Illustration Area of the recirculation zone behind the jet in crossflow for u<0.05 m/s (a) and recirculation zone area for all flow rates and geometries (b)

This suggests a significant change in the flow field where the jets collectively obstruct the crossflow leading to a large recirculation zone. Despite the potential uncertainty caused by spatial resolution, PIV vector density, and slight misalignment of the laser sheet with the jet center, the pronounced increase in recirculation zone area for $l/d = 1.5$ strongly suggests a fundamental shift in the flow field dynamics, where reduced spacing leads to a more substantial jet blockage effect. To summarize, tightly spaced jets lead to the formation of a large recirculation zone, which could have deep implications on micromix hydrogen flame stabilization mechanism.

4.5 Shear layer position tracking in the transverse (YZ) plane

Frequency analysis can help further understand JICF interactions in arrays and tie it to the mixing metrics. Recent numerical and experimental investigations explored the transition of a transverse jet's shear layer from convective to absolute instability [52, 53]. The Strouhal number $\mathrm{St} = \frac{fL}{U}$ is used to characterize these instabilities, where f is the vortex shedding frequency, L is a characteristic length, and U is the flow velocity. When the density ratio S decreases below approximately $S \approx 0.4$, jets transition to global instability, exhibiting sharp shifts in Strouhal number and decreased mixing efficiency [53]. This is because the formation of large, organized vortices associated with global instabilities inhibits the smaller-scale turbulence that is more effective at mixing fluids. Momentum is trapped in large-scale motions, limiting the transfer to smaller structures to assist dispersion. The low density of H_2 relative to air results in low density ratios ($S = 0.07 \ll 1$), thus making micromix burners

very susceptible to absolute instabilities, potentially affecting mixing efficiency and flame properties in these combustion systems. This needs to be investigated to further understand hydrogen injection technology.

As shown in Figure 4.11, the position of the shear layer between the seeded helium jet and the crossflow is tracked in time over 1000 images, revealing a strong periodic signal indicative of globally unstable oscillations for $1.35 > J > 7.37$. Figure 4.17 illustrates a typical periodic signal, showing the raw and detrended signal amplitude of shear layer position for a single JICF at $J = 3.75$ in the top and bottom panels, respectively. To prepare the data for analysis, outliers were identified using SciPy's Z-score method with a threshold of 3 and replaced through linear interpolation between adjacent valid data points. The data was smoothed using a moving average filter with a window size of $N = 3$ to balance noise reduction and signal fidelity. A sliding window linear detrending of 200 data points per segment, implemented via SciPy, removed slow-varying trends associated with jet fluttering, thereby isolating the oscillatory behavior. Peaks in the detrended shear layer position $y_{max}(t)$ data were detected using SciPy's `find_peaks` function, with the minimum peak distance parameter adjusted dynamically based on the flow rate, ranging from 2 to 12 data points. The dominant frequency was estimated by counting the number of peaks n_{peaks} over the total duration $\Delta t = 0.1$ s. This methodology enables consistent and reliable peak detection, providing repeatable calculations of the average main shear layer oscillation frequencies.

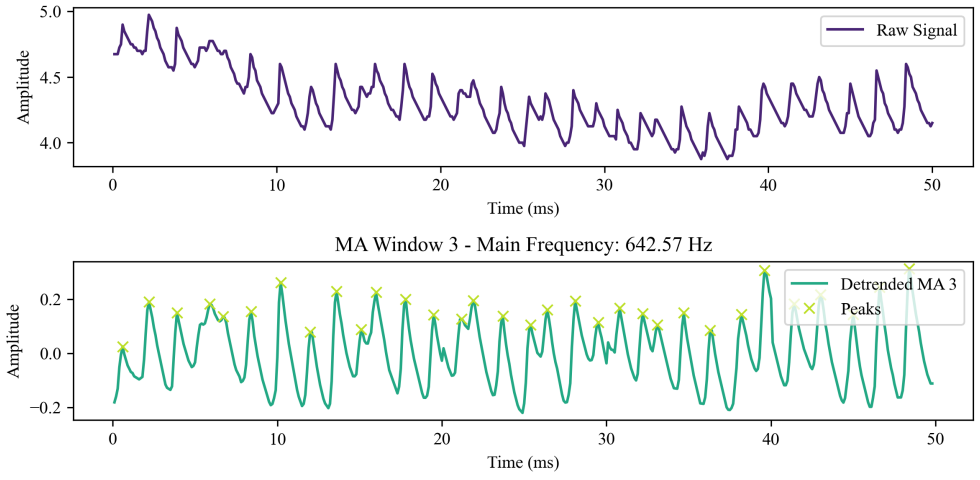

Figure 4.17 Raw and detrended signal of shear layer position over time for $J = 3.75$ and $x/d = 2.5$

Figure 4.18 presents the average peak frequency of shear layer oscillations as a function of

arrays spacing, downstream distance and jet flow rate. The frequencies were obtained using the aforementioned peak detection algorithm applied to time-series data of the shear layer position $y_{max}(t)$. Figure 4.18a shows the variation of average peak frequency of the shear layer oscillations as a function of downstream distance for different jet configurations at $J = 2.40$. Figure 4.18b displays the effect of flow rate and array spacing on shear layer average frequencies. These results indicate that higher flow rates lead to higher initial oscillation frequencies near the jet exit. For example, at $x/d = 1$, the frequency reaches approximately 780 Hz for $R = 8.29$(4 SLPM), but it is approximately 550 Hz for $R = 2.07$ (1 SLPM). These results suggest that faster jets exhibit more frequent oscillations as they enter the crossflow. This observation aligns with the Strouhal number definition, $St = \frac{f \cdot l}{U}$, indicating that, for a constant St and jet diameter d, an increase in jet exit velocity U leads to a linear increase in vortex shedding frequency f. As the jet moves downstream, the average oscillation frequency diminishes. The magnitude of this reduction is more pronounced for tightly spaced jet arrays. For instance, the $l/d = 2$ case shows a decrease in frequency from 880 Hz to 520 Hz over the range from $x = 0$ mm to $x = 14$ mm. In contrast, the single jet case shows a smaller reduction, from 590 Hz to approximately 500 Hz over the same downstream distance. This greater frequency reduction for tightly spaced array of jets may be attributed the increased spread shown in Figure 4.10 and to from intensified jet interactions resulting in a more substantial energy decay, as illustrated in Figure 4.3. These jet-to-jet interactions lead to faster dissipation of shear layer energy, thereby enhancing mixing and reducing average oscillation frequencies.

In summary, higher velocity ratios induce increased shear layer vortex shedding frequencies in the near field of the jet array. Globally unstable cases with very low density ratios ($1 < J < 8$) exhibit high-amplitude oscillations that can be tracked over time. As the low-density jet fluid enters the crossflow, these oscillations diminish in frequency downstream, indicating increased mixing and loss of coherence. Tightly spaced jet arrays show higher shear layer frequencies than the single JICF case, likely due to jet-to-jet interactions generating additional peaks in the shear layer position time series. This behavior suggests enhanced turbulence and reduced coherence in tightly spaced array configurations.

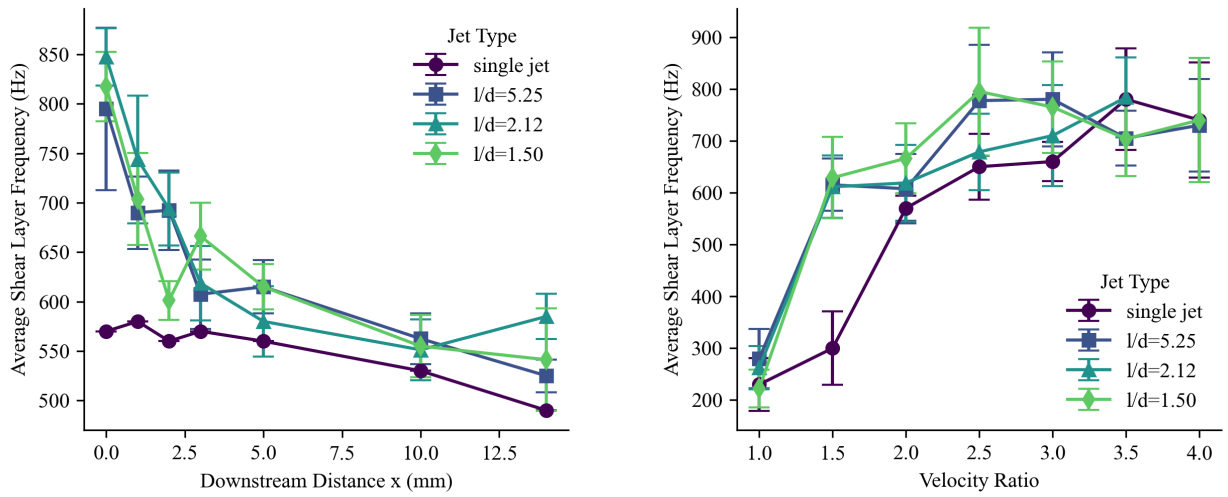

(a) (b)

Figure 4.18 Average main shear layer frequency for the four array geometries against (a) downstream distance for $J = 2.4$ and against (b) jet flow rate at $x/d = 4$

CHAPTER 5 SUPPLEMENTAL WORK

5.1 XZ plane measurements

Scattering images

Measurements in the XZ plane were made for 5 momentum flux ratios values from 2 to 10 for the 8 jet array spaced by $l/d = 2.12$. Some of these images are visible in Figure 5.1 for 6 different y height scans between $y/d = 0$ to 12. Strong phase locking and pulsating shear layer vortices are visible in the near field, further indicating that low density JICf are globally unstable for $J < 10$. This plane has great potential to measure the effect of array spacing on mixing, as the instabilities visibly dampen and dissolve with downstream distance x.

These images shown reveal that the shear layer is not well mixed and follows a periodic change in helium concentration over time which is most likely detrimental for combustion. Cells of fuel at high mixture strength should be mixed quickly to reduce hot spots and reduce NO_x emissions. However, low density jets in crossflow do not behave that way as they are inherently unstable.

Velocity field vs J

The PIV vector fields are shown in Figure 5.2 for 4 SLPM for an 8 jet array spaced by $l/d = 2.12$. Similar velocity fields are recorded for 2, 3, 6 and 8 SLPM. The low velocity zone is visible below the jets. The crossflow momentum is largely blocked by the jets, although some of it passes between them helping to remove the recirculation zone.

5.2 Spectral analysis of shear layer oscillations

For comprehensive frequency analysis, a Fast Fourier Transform (FFT) is applied to the detrended shear layer position over time signal using NumPy's FFT functions. Prior to performing the FFT, the mean of the signal was subtracted to remove low frequency signal components, and a Hann window was applied to reduce spectral leakage. The frequency spectrum $|Y(f)|$ can then be analyzed to identify dominant frequencies associated with the jets' oscillatory behavior.

The FFT of the single jet signal showed in last section gives the following very clear signal in Figure 5.3. It showcases an amplitude peak at 550 Hz, which is equivalent to the frequency

value of 560 Hz detected using the peak detection algorithm used in section 4.5. The FFT works well in showcasing peak frequency when the shear layer position in time is periodic and not influenced by neighboring jets, which add turbulence and unpredictability in the shear layer oscillation amplitude and period length.

To show and explain jet-to-jet interactions, the spectra of 8 jets in an array subjected to the same flow conditions can be compared. This is visible in Figure 5.4, where the FFT of 8 jets spaced by $l/d = 2.12$ is illustrated for $x/d = 6.25$ and for jets sharing the same peaks, a connection between them is implied.

High J cases with more than 4 jets produce a very noisy FFT spectrum featuring several small peaks around 500 Hz. Further work could entail scaling these frequencies with the Strouhal number to model them as a function of array spacing. It is complex to extract a conclusion from the present FFT of jet arrays as the periodicity of the oscillations is strongly diminished. The FFT thus becomes noisy when multiple jets interact and break the cyclical nature of the shear layer oscillations. Further analysis or a better measuring technique is needed.

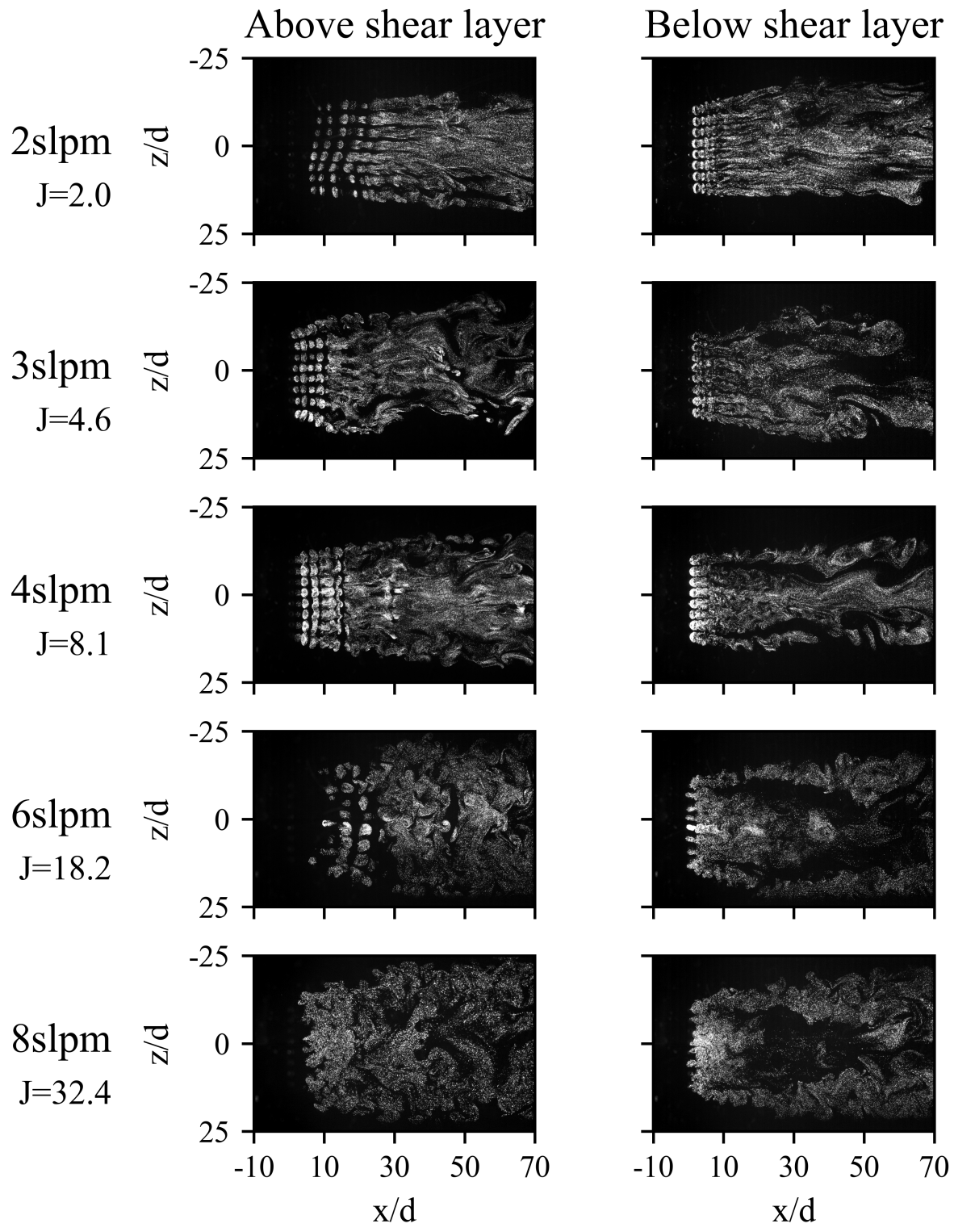

Figure 5.1 Lateral X-Y plane mie scattering measurements of 8 jet array in crossflow for various momentum ratios

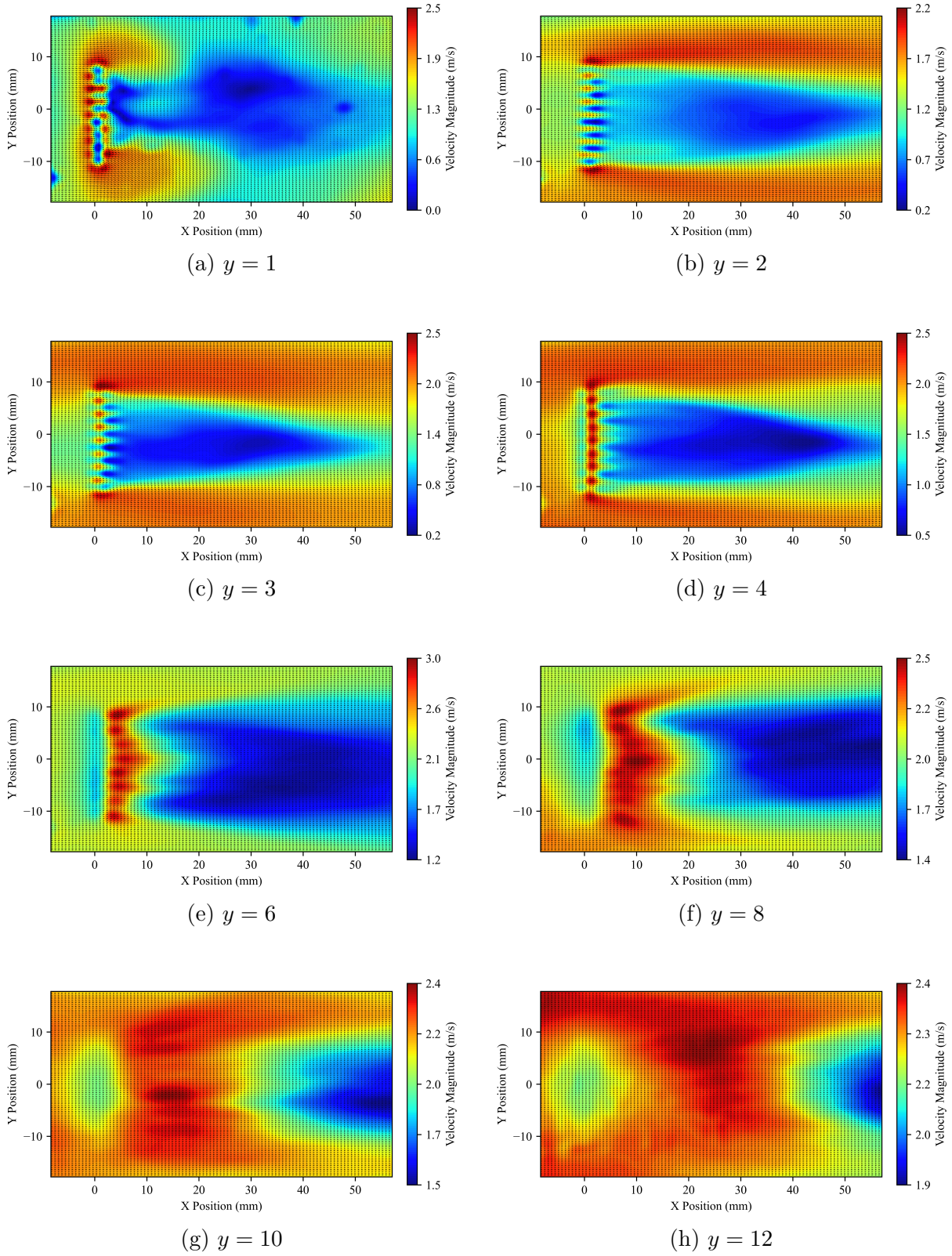

(a) $y = 1$ (b) $y = 2$

(c) $y = 3$ (d) $y = 4$

(e) $y = 6$ (f) $y = 8$

(g) $y = 10$ (h) $y = 12$

Figure 5.2 Instantaneous velocity fields for 4 slpm, j=10, evaluated at many y location

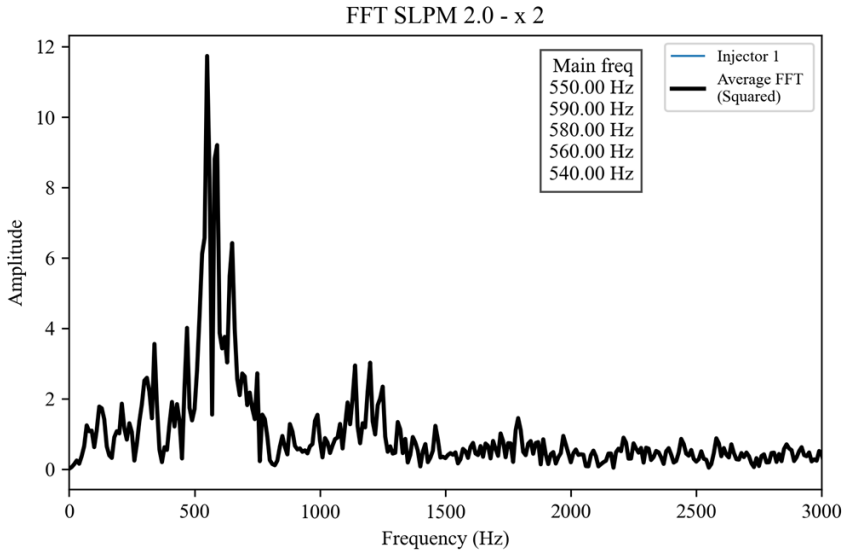

Figure 5.3 Power spectrum of a globally unstable single low density jet in crossflow at x/d=2 and J=2.5

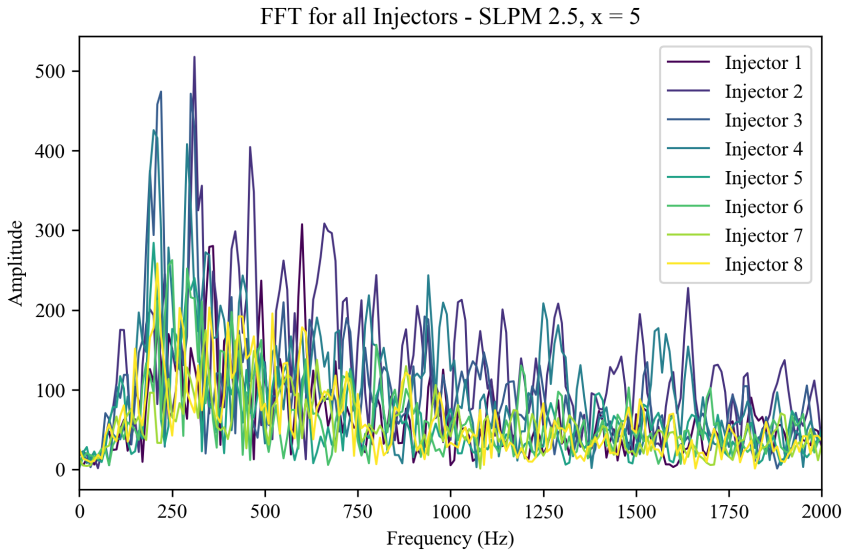

Figure 5.4 Power spectrum of an array of 8 unstable low density jet in crossflow at J=2.5 and x/d=6

CHAPTER 6 THESIS CONCLUSION

6.1 Work Summary

With the emergence of hydrogen as a promising carbon-free fuel for combustion processes, novel injector geometries are needed to mix this low density gas with air ahead of the flame front. The newly proposed Micromix configuration employs numerous micro jets in crossflow (JICF) to reduce harmful NO_x emissions and the risk of flame flashback. While single jets in crossflow have been widely explored both numerically and experimentally in fundamental and applied research, arrays with very low jet-to-crossflow density ratios relevant for hydrogen combustion remain rarely studied. An experimental setup was therefore designed to obtain high frequency recordings of low density micro jet arrays in crossflow. This was accomplished by using a high-speed PIV system to record particle laden helium JICFs illuminated with a thin laser sheet. A square channel test section was modified to provide low density injection into an air crossflow for this non-reactive study. A custom injection plate was machined, enabling the study of four geometries with 1, 4 and 8 jets enabling jet-to-jet spacing of $l/d = \infty$, 5.25, 2.12 and 1.5.

Trajectories of low density micro jet arrays were compared to those of single larger diameter JICF. To this end, the center jet was visualized on a longitudinal plane for a range of helium flow rates and array spacings. This showed that for a constant low density ratio of 0.14, jet centerlines trajectories collapse when scaled by the velocity ratio R, as is the case for classical JICF. Experimental results point towards the trajectory model $\frac{y}{Rd} = 1.43(\frac{x}{Rd})^{0.32}$ to describe the average centerline trajectory of low density JICF arrays.

To quantity the mixing of the JICF array with the available PIV system, the spread of the jets in the longitudinal and transverse planes was measured between $x/d = 1$ to 15 as a function jet flow rate and array spacing. Key results show that closely spaced arrays lead to JICFs that spread more rapidly. The size of the JICF counter rotating vortex pair (CVP) also increases in length with decreasing jet spacing, likely caused by neighboring jets reducing room for lateral movement. Velocity fields captured on the longitudinal plane show that arrays of jets generate a lee-side low velocity zone, which increases in size with higher jet velocities, and is particularly marked for spacing of $l/d = 1.5$. This low velocity zone could favor upstream stabilization of the hydrogen flame.

Lastly, the effect of jet array spacing on the JICF coherent structures and instabilities was investigated. High speed recordings highlighted the formation of unstable and strong shear

layer vortices that increase in amplitude for larger jet-to-crossflow velocity ratios, which is expected for globally unstable very low density JICF. It is believed that tightly spaced arrays of jets help to reduce the shear layer structure coherence and escape globally unstable modes faster downstream. Some novel jet-to-jet interactions are also visible, for instance when a jet's CVP entrains a neighboring jet's CVP into its own vortex rotation. Finally, the shear layer position is tracked in time showing that arrays of 8 jets exhibit higher average oscillation frequencies compared to the 4-jet and single jet cases. The single jet configuration shows the lowest frequency values across all downstream positions, which could be attributed to the lack of jet-to-jet interactions.

6.2 Future Research opportunities

The lessons learned during this Master's project are listed below with appropriate future research opportunities.

The size of the crossflow boundary layer to the jet diameter was fixed at a large ratio of $\delta/d \approx 10$ in the current setup. This may cause different jet penetration behavior as a function of jet velocity because the crossflow becomes increasingly rapid with distance from the test section floor. To address this, a new experimental campaign is proposed, utilizing a sharp, adjustable metallic plate to vary the boundary layer size. Investigating the effect of boundary layer thickness to jet diameter ratio could allow for further understanding of its effect on jet penetration dynamics.

Implementing a multi-camera flow measurement system, such as 2D or 3D tomographic PIV, would greatly advance future research by enabling measurements of the intricate 3D velocity fields that emerge past arrays of low-density jets in crossflow. This approach would allow solving current out of plane velocities and better understand jet interactions, turbulence characteristics, and dominant flow structures across different array configurations and velocity ratios.

To gain a more granular understanding of jet spacing effects, particularly to identify the critical l/d value at which blockage occurs, future experiments could benefit from an injection plate with more gradual l/d variations or more injection holes. Such a setup would allow for efficient parametric studies of the array geometry, offering insights into optimal configurations.

Additionally, varying the density ratio S could reveal its influence on flow instabilities. Understanding these dynamics could help predict behaviors when higher-density natural gas is mixed with hydrogen in combustion systems, to help optimize stability and performance of

low-emission burners. Hot wire probe measurements of the shear layer velocity fluctuations could help gather more precise and complete frequency signals. Also, further work is needed to assess the effect of jet array spacing on the global vs convective stability transition.

The current work used DEHS oil particles as a flow tracer and visualization tool, which does not take molecular diffusion into account. Laser based diagnostics, such as NO-LIF, are thus needed to accurately measure concentration fields of gaseous fuels. This could help understand the impact of instabilities, J and array geometries on the mixing process of low density gases into air.

It is clear that the Reynolds numbers used in this study are orders of magnitude lower than what is present in gas turbine combustors. The crossflow in this work leads to a relatively low Reynolds number of $\mathrm{Re}_\infty \approx 7000$. Thus, a dedicated test campaign is needed to investigate the effects of increasing both jet and crossflow Reynolds numbers. This new research would provide insights into how changes in flow regime impact jet penetration, mixing, coherent structures and jet-to-jet interactions.

Finally, reactive studies with an ignited array of hydrogen jets in crossflow are needed to measure the effect of array geometry and velocity ratio on pollutant emissions and flame stabilization mechanism.

REFERENCES

[1] H. Ritchie, P. Rosado, and M. Roser, "Co_2 and greenhouse gas emissions," *Our World in Data*, 2023, https://ourworldindata.org/co2-and-greenhouse-gas-emissions.

[2] Environment and Climate Change Canada, "Canada's air pollutant emissions inventory report," Environment and Climate Change Canada, Gatineau, QC, Series En81-30E-PDF, 2019.

[3] H. Ritchie and P. Rosado, "Fossil fuels," *Our World in Data*, 2017, https://ourworldindata.org/fossil-fuels.

[4] Statistics Canada, "Historical Statistics of Canada: Section Q: Energy and Electric Power," Statistics Canada. www.statcan.gc.ca, 2014, archived 2014-07-02. [Online]. Available: https://www150.statcan.gc.ca/n1/pub/11-516-x/sectionq/4057756-eng.htm

[5] J. Bolt, M. P. Timmer, and J. L. van Zanden, *GDP per capita since 1820*. Organisation for Economic Cooperation and Development (OECD) publishing, 2014.

[6] International Energy Agency, "Global hydrogen review 2023," International Energy Agency, Paris, Tech. Rep., 2023, licence: CC BY 4.0. [Online]. Available: https://www.iea.org/reports/global-hydrogen-review-2023

[7] M. Yue, H. Lambert, E. Pahon, R. Roche, S. Jemei, and D. Hissel, "Hydrogen energy systems: A critical review of technologies, applications, trends and challenges," *Renewable and Sustainable Energy Reviews*, vol. 146, p. 111180, 2021.

[8] Natural Resources Canada, "Hydrogen strategy for canada," Natural Resources Canada, Tech. Rep., December 2020. [Online]. Available: https://natural-resources.canada.ca/climate-change/canadas-green-future/the-hydrogen-strategy/23080

[9] J. Johansson, J. Leirnes, K. Walton, E. Yilmaz, and E. Zindel, "Hydrogen power and heat with siemens energy gas turbines," Siemens Energy Global GmbH & Co. KG, Freyeslebenstraße 1, 91058 Erlangen, Germany, White Paper, 2022.

[10] L. M. Das, *Hydrogen*. John Wiley and Sons, Ltd, 2021, ch. 13, pp. 373–402.

[11] National Aeronautics and Space Administration, "Safety standard for hydrogen and hydrogen systems: Guidelines for hydrogen system design, materials selection, operations, storage, and transportation," Office of Safety and Mission Assurance, Washington,

DC 20546, Washington, DC, Tech. Rep. NASA-STD-6001, Feb 1997, available from: https://standards.nasa.gov/standard/nasa/nasa-std-6001.

[12] Emoscopes, "Turboshaft operation," 2011, creative Commons CC BY-SA 3.0, via Wikimedia Commons. [Online]. Available: https://commons.wikimedia.org/wiki/File:Turboshaft_operation.png

[13] G. D. Lewis, "Prediction of NOx Emissions," ser. Turbo Expo: Power for Land, Sea, and Air, vol. Volume 2: Coal, Biomass and Alternative Fuels; Combustion and Fuels; Oil and Gas Applications; Cycle Innovations, 03 1981, p. V002T06A023. [Online]. Available: https://doi.org/10.1115/81-GT-119

[14] P. Versailles, "CH formation in premixed flames of C1–C4 alkanes: assessment of current chemical modelling capability against experiments," PhD Thesis, McGill University, Montreal, Canada, 2017. [Online]. Available: https://escholarship.mcgill.ca/concern/theses/m326m4500

[15] C. K. Law, *Combustion Physics*. Cambridge University Press, 2006.

[16] K. K. Kuo, *Principles of Combustion*, 2nd ed. New Jersey: John Wiley & Sons, 2005, chapter 5: Premixed Laminar Flames.

[17] T. C. Lieuwen, *Unsteady Combustor Physics*. Cambridge University Press, 2012.

[18] P. Therkelsen, T. Werts, V. McDonell, and S. Samuelsen, "Analysis of nox formation in a hydrogen-fueled gas turbine engine," *Journal of Engineering for Gas Turbines and Power*, vol. 131, no. 3, p. 031507, 02 2009. [Online]. Available: https://doi.org/10.1115/1.3028232

[19] H.-W. Funke, N. Beckmann, and S. Abanteriba, "An overview on dry low nox micromix combustor development for hydrogen-rich gas turbine applications," *International Journal of Hydrogen Energy*, vol. 44, no. 13, pp. 6978–6990, 2019.

[20] H. H.-W. Funke, N. Beckmann, J. Keinz, and A. Horikawa, "30 years of dry-low-nox micromix combustor research for hydrogen-rich fuels—an overview of past and present activities," *Journal of Engineering for Gas Turbines and Power*, vol. 143, no. 7, p. 071002, 03 2021.

[21] S. Boerner, D.-I. H. Funke, P. Hendrick, E. Recker, and R. Elsing, "Development and integration of a scalable low nox combustion chamber for a hydrogen-fueled aerogas turbine," *EUCASS Proceedings Series*, vol. 4, pp. 357–372, 03 2013.

[22] H. H.-W. Funke, S. Boerner, J. Keinz, K. Kusterer, D. Kroniger, J. Kitajima, M. Kazari, and A. Horikawa, "Numerical and experimental characterization of low nox micromix combustion principle for industrial hydrogen gas turbine applications," ser. Turbo Expo: Power for Land, Sea, and Air, vol. Volume 2: Combustion, Fuels and Emissions, Parts A and B, 06 2012, pp. 1069–1079. [Online]. Available: https://doi.org/10.1115/GT2012-69421

[23] A. Landry-Blais, S. Sivić, and M. Picard, "Micro-Mixing Combustion for Highly Recuperated Gas Turbines: Effects of Inlet Temperature and Fuel Composition on Combustion Stability and NOx Emissions," *Journal of Engineering for Gas Turbines and Power*, vol. 144, no. 9, p. 091014, 08 2022.

[24] R. Schefer, T. Smith, and C. Marek, "Evaluation of nasa lean premixed hydrogen burner," Sandia National Laboratories, Albuquerque, New Mexico 87185 and Livermore, California 94550, Tech. Rep. SAND2002-8609, January 2003, unlimited Release, Printed January 2003.

[25] T. Howarth, M. Picciani, E. Richardson, M. Day, and A. Aspden, "Direct numerical simulation of a high-pressure hydrogen micromix combustor: Flame structure and stabilisation mechanism," *Combustion and Flame*, vol. 265, p. 113504, 2024. [Online]. Available: https://www.sciencedirect.com/science/article/pii/S0010218024002128

[26] A. R. Karagozian, "The jet in crossflow," *Physics of Fluids*, vol. 26, no. 10, p. 101303, 09 2014.

[27] Chilangabacho, "The volcano popocatepetl erupts on the east side of the valley of mexico," December 2018, creative Commons CC BY-SA 4.0, via Wikimedia Commons. [Online]. Available: https://commons.wikimedia.org/wiki/File:The_volcano,_Popocatepetl_(Nahuatl_for_%22Smoking_Mountain%22,_on_the_east_side_of_the_Valley_of_Mexico,_errupts_on_Dec.2018.jpg

[28] D. Laity and H. Seidel, "Figure from the national archives: NOAA collection," National Archives, 1980, capture Date: 11/26/1980. [Online]. Available: https://catalog.archives.gov/id/17499524

[29] joelbeeb, "Zimmer power plant smoke stack," December 2007, photo of Zimmer Power Plant smoke stack. [Online]. Available: https://commons.wikimedia.org/wiki/File:Zimmer_Power_Plant_Smoke_Stack_-_panoramio.jpg

[30] R. J. Margason, "Fifty years of jet in cross flow research," in *the 72nd AGARD Fluid Dynamics Panel Meeting and Symposium on Computational and Experimental Assessment of Jets in Cross Flow*, April 1993.

[31] C. H. Bosanquet and J. L. Pearson, "The spread of smoke and gases from chimneys," *Trans. Faraday Soc.*, vol. 32, pp. 1249–1263, 1936.

[32] E. E. Callaghan and R. S. Ruggeri, "Investigation of the penetration on an air jet directed perpendicularly to an air stream," National Advisory Committee for Aeronautics, Flight Propulsion Research Laboratory, Cleveland, Ohio, Tech. Rep., June 1948.

[33] R. S. Ruggeri, E. E. Callaghan, and D. T. Bowden, "Penetration of air jets issuing from circular, square, and elliptical orifices directed perpendicularly to an air stream," National Advisory Committee for Aeronautics, Lewis Flight Propulsion Laboratory, Cleveland, Ohio, Tech. Rep., February 1950.

[34] J. F. Keffer and W. D. Baines, "The round turbulent jet in a cross-wind," *Journal of Fluid Mechanics*, vol. 15, no. 4, p. 481–496, 1963.

[35] Y. Kamotani and I. Greber, "Experiments on a turbulent jet in a cross flow," *AIAA Journal*, vol. 10, no. 11, pp. 1425–1429, 1972.

[36] H. Tennekes and J. L. Lumley, *A First Course in Turbulence*. Cambridge, MA: MIT Press, 1972.

[37] R. J. Margason, "The path of a jet directed at large angles to a subsonic free stream," NASA Langley Research Center, Langley Station, Hampton, Va., Tech. Rep. NASA TN D-4919, November 1968.

[38] S. Muppidi and K. Mahesh, "Study of trajectories of jets in crossflow using direct numerical simulations," *Journal of Fluid Mechanics*, vol. 530, p. 81–100, 2005.

[39] S. H. Smith and M. G. Mungal, "Mixing, structure and scaling of the jet in crossflow," *Journal of Fluid Mechanics*, vol. 357, p. 83–122, 1998.

[40] T. F. Fric and A. Roshko, "Vortical structure in the wake of a transverse jet," *Journal of Fluid Mechanics*, vol. 279, p. 1–47, 1994.

[41] R. M. Kelso, T. T. Lim, and A. E. Perry, "An experimental study of round jets in cross-flow," *Journal of Fluid Mechanics*, vol. 306, pp. 111–144, 1996.

[42] T. T. Lim, T. H. New, and S. C. Luo, "On the development of large-scale structures of a jet normal to a cross flow," *Physics of Fluids*, vol. 13, no. 3, pp. 770–775, 03 2001.

[43] E. Meyer, J. Pederson, and O. Özcan, "A turbulent jet in crossflow analysed with proper orthogonal decomposition," *Journal of Fluid Mechanics*, vol. 583, p. 199–227, 2007.

[44] K. E. Meyer, O. Özcan, P. S. Larsen, P. Gjelstrup, and C. H. Westergaard, "Point and planar lif for velocity-concentration correlations in a jet in cross flow," in *Proceedings of 10th International Symposium on Applications of Laser Techniques To Fluid Mechanics*. Springer Verlag, 2002.

[45] L. K. Su and M. G. Mungal, "Simultaneous measurements of scalar and velocity field evolution in turbulent crossflowing jets," *Journal of Fluid Mechanics*, vol. 513, p. 1–45, 2004.

[46] L. Gevorkyan, T. Shoji, D. R. Getsinger, O. I. Smith, and A. R. Karagozian, "Transverse jet mixing characteristics," *Journal of Fluid Mechanics*, vol. 790, p. 237–274, 2016.

[47] P. Huerre and P. A. Monkewitz, "Local and global instabilities in spatially developing flows," *Annual Review of Fluid Mechanics*, vol. 22, no. Volume 22, 1990, pp. 473–537, 1990. [Online]. Available: https://www.annualreviews.org/content/journals/10.1146/annurev.fl.22.010190.002353

[48] R. J. Briggs, *Electron-Stream Interaction with Plasmas*. Cambridge, MA: The MIT Press, dec 1964, chapter 2.

[49] J. M. Chomaz, P. Huerre, and L. G. Redekopp, "Bifurcations to local and global modes in spatially developing flows," *Physical Review Letters*, vol. 60, no. 1, pp. 25–28, 1988.

[50] P. A. Monkewitz, D. W. Bechert, B. Barsikow, and B. Lehmann, "Self-excited oscillations and mixing in a heated round jet," *Journal of Fluid Mechanics*, vol. 213, p. 611–639, 1990.

[51] S. Megerian, J. Davitian, L. S. de Brito Alves, and A. R. Karagozian, "Transverse-jet shear-layer instabilities. part 1. experimental studies," *Journal of Fluid Mechanics*, vol. 593, pp. 93 – 129, 2007. [Online]. Available: https://api.semanticscholar.org/CorpusID:122830423

[52] T. Shoji, E. W. Harris, A. Besnard, S. G. Schein, and A. R. Karagozian, "On the origins of transverse jet shear layer instability transition," *Journal of Fluid Mechanics*, vol. 890, p. A7, 2020.

[53] D. R. Getsinger, C. Hendrickson, and A. R. Karagozian, "Shear layer instabilities in low-density transverse jets," *Experiments in Fluids*, vol. 53, no. 3, pp. 783–801, Sep. 2012. [Online]. Available: https://doi.org/10.1007/s00348-012-1329-x

[54] J. D. Holdeman, "Mixing of multiple jets with a confined subsonic crossflow," *Progress in Energy and Combustion Science*, vol. 19, no. 1, pp. 31–70, 1993.

[55] A. K. Moawad and N. Rajaratnam, "Dilution of multiple nonbuoyant circular jets in crossflows," *Journal of Environmental Engineering*, vol. 124, no. 1, pp. 51–58, 1998.

[56] P. Ajersch, J.-M. Zhou, S. Ketler, M. Salcudean, and I. S. Gartshore, "Multiple Jets in a Crossflow: Detailed Measurements and Numerical Simulations," *Journal of Turbomachinery*, vol. 119, no. 2, pp. 330–342, 04 1997.

[57] R. G. Brakmann, R. Schöffler, F. Kocian, M. Schroll, C. Willert, M. Müller, and E. Kügeler, "Quantitative flow imaging of film cooling jets in a cross-flow using particle image velocimetry and computational fluid dynamics," in *ASME Turbo Expo 2020: Turbomachinery Technical Conference and Exposition*, ser. Turbo Expo: Power for Land, Sea, and Air, vol. 7B. The American Society of Mechanical Engineers (ASME), 9 2020, p. V07BT12A069.

[58] Z. Cao, B. Sundén, and J. Fu, "An experimental study on heat transfer performance of jet impingement arrays," ser. Heat Transfer Summer Conference, vol. ASME 2022 Heat Transfer Summer Conference, 07 2022, p. V001T12A003.

[59] B. Bai, Z. Li, M. Hao, Y. Li, K. Zhang, Z. Li, and J. Li, "Turbine blade endwall heat transfer and film cooling performance with multigap jets and film holes," *Journal of Engineering for Gas Turbines and Power*, vol. 145, no. 11, p. 111020, 10 2023.

[60] P. J. Kristo and M. L. Kimber, "Time-resolved particle image velocimetry measurements of a tandem jet array in a crossflow at low velocity ratios," *Experiments in Fluids*, vol. 62, no. 4, p. 67, 2021.

[61] O. Jobin, "Small-scale experiments for the development and characterization of novel hybrid rocket fuel systems," Ph.D. dissertation, Polytechnique Montreal, Montreal, Canada, December 2023.

[62] T. L. Bergman and F. P. Incropera, *Fundamentals of Heat and Mass Transfer*, 7th ed. Wiley, 2011.

[63] B. McKeon, G. Comte-Bellot, J. Foss, J. Westerweel, F. Scarano, and C. Tropea, "Velocity, vorticity, and mach number," in *Springer Handbook of Experimental Fluid Mechanics*, C. Tropea, A. L. Yarin, and J. F. Foss, Eds. Berlin, Heidelberg: Springer, 2007, ch. 5, pp. 215–471.

[64] A. Melling, "Tracer particles and seeding for particle image velocimetry," *Measurement Science and Technology*, vol. 8, no. 12, p. 1406, dec 1997. [Online]. Available: https://dx.doi.org/10.1088/0957-0233/8/12/005

[65] A. Sankaran, R. Hain, and C. J. Kähler, "Particle image based simultaneous velocity and particle concentration measurement," *Measurement Science and Technology*, vol. 35, no. 6, 2024.

[66] T. F. Fric, "Effects of fuel-air unmixedness on nox emissions," *Journal of Propulsion and Power*, vol. 9, no. 5, pp. 708–713, 1993.

[67] R. Sau and K. Mahesh, "Dynamics and mixing of vortex rings in crossflow," *Journal of Fluid Mechanics*, vol. 604, p. 389–409, 2008.

[68] K. Mahesh, "The interaction of jets with crossflow," *Annual Review of Fluid Mechanics*, vol. 45, no. 1, pp. 379–407, 2013.

[69] S. Muppidi and K. Mahesh, "Direct numerical simulation of round turbulent jets in crossflow," *Journal of Fluid Mechanics*, vol. 574, p. 59–84, 2007.

[70] P. Virtanen, R. Gommers, T. E. Oliphant, M. Haberland, T. Reddy, D. Cournapeau, E. Burovski, P. Peterson, W. Weckesser, J. Bright, S. J. van der Walt, M. Brett, J. Wilson, K. J. Millman, N. Mayorov, A. R. J. Nelson, E. Jones, R. Kern, E. Larson, C. J. Carey, İ. Polat, Y. Feng, E. W. Moore, J. VanderPlas, D. Laxalde, J. Perktold, R. Cimrman, I. Henriksen, E. A. Quintero, C. R. Harris, A. M. Archibald, A. H. Ribeiro, F. Pedregosa, P. van Mulbregt, and SciPy 1.0 Contributors, "SciPy 1.0: Fundamental Algorithms for Scientific Computing in Python," *Nature Methods*, vol. 17, pp. 261–272, 2020.

[71] B. D. Pratte and W. D. Baines, "Profiles of the round turbulent jet in a cross flow," *Journal of the Hydraulics Division*, vol. 93, no. 6, pp. 53–64, 1967.

[72] M. Ilak, P. Schlatter, S. Bagheri, and D. Henningson, "Bifurcation and stability analysis of a jet in cross-flow: Onset of global instability at a low velocity ratio," *Journal of Fluid Mechanics*, vol. 696, pp. 94–121, 04 2012.

APPENDIX A PROOF OF CONCEPT: PRELIMINARY RESULTS AND EXPERIMENTAL FACILITY

This section showcases key results from the proof of concept experimental study. It was presented at the Combustion Institute Canadien Section (CICS) Spring Technical Meeting, May 14th, 2024 at Queen's University. It successfully showed that the experimental setup could extract high quality datasets of jets in crossflow. This preliminary study was key in learning the PIV technique, and also helpfull in tuning acquisition parameters for more precise data gathering in the future.

Jet trajectories and spatial mixing

Analysis of particle number density of the jet in crossflow, via image pixel signal intensity, aims to determine whether the jet centerline trajectories, penetration depth, spread, and spread rate align with behaviors predicted in the literature, despite the utilization of very low density micro jets arranged in a linear array. Figure A.1 provides an instantaneous image of a low-density micro JICF with the DEHS particles illuminated by the laser sheet from the jet injection point to the end of the test section at $x/d = 70$. Note that the laser sheet is cut 2mm above the bottom surface to prevent reflections into the camera. Figure A.2 depicts the average particle intensity field, computed from an ensemble of 1000 images at 1 kHz illuminated with the second laser head. The resulting image represents the time-averaged seeded particle number density within laser sheet. Near unity particle number density at the injector tip indicates high particle overlap, limited spread, and low mixing close to the jet's origin, used as reference.

Figure A.3 presents jet centerline trajectories and penetration depths for low-density micro jets in a crossflow. Figure A.3a shows the jet centerline trajectories based on the maximum average particle signal along the x-axis. These points are then fitted to a simple power-law curve, where A and B are constant parameters obtained from a non-linear least squares fitting using SciPy [70]. The obtained values of the exponential decay parameter are from $B = 0.3$ for J=5 and to $B = 0.38$ for J=100. These results are similar to values of $B = 1/3$ in the far field of subsonic JICF found in the literature [26]. Jets with a higher momentum flux ratio, J, achieve greater centerline penetration into the crossflow, and exhibit asymptotic behaviors further downstream of the injection point. Figure A.3b further supports this by displaying a linear relationship between the injection depth and J evaluated at $x/d = 60$, as

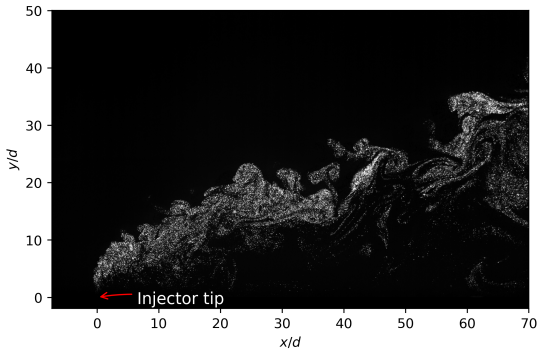

Figure A.1 JICF High-speed PIV image

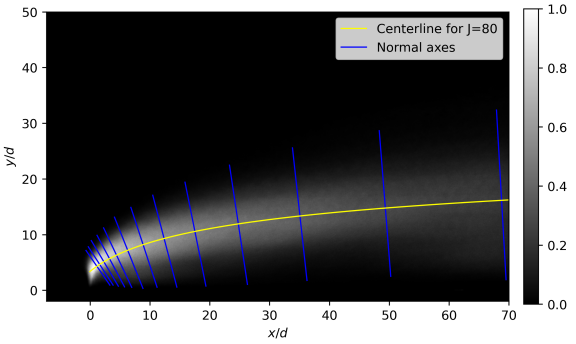

Figure A.2 Time averaged normalized particle intensity

expressed by the linear fit $y/d = 0.16J + 0.73$ with a high R^2 value of 0.9917. The vertical error bars in figure A.3b reflect the standard deviation of ten calculated injection depths for a single J, each derived from subsets of 100 instantaneous images out of the 1000 collected in each time series.

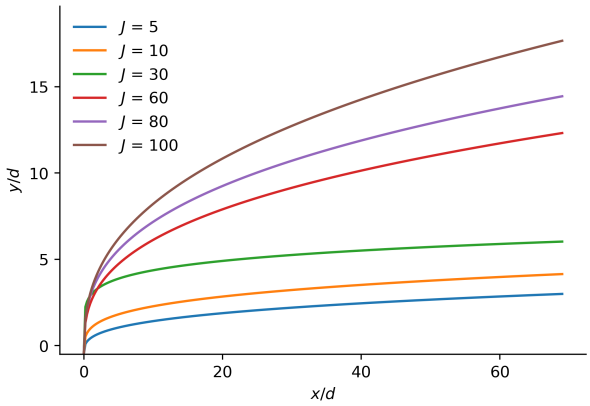

Figure A.2 (a)

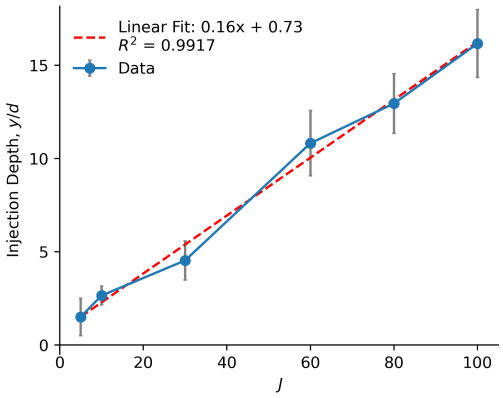

Figure A.2 (b)

Figure A.3 JICF fitted trajectories (a) and penetration depth (b) as a function of momentum flux ratio J.

Figure A.4 provides a visualization of particle number density distributions for a micro JICF of $J = 80$. The normalized raw image signal intensity is captured along multiple planes perpendicular to the jet's centerline axis C. These planes, shown in Figure A.2b, are normal to the jet centerline axis and capture the jet behavior at various stages of its penetration within the crossflow. This visualization helps in understanding how the particle intensity decays

with increasing time in contact with the air crossflow. Figure A.4 also presents Gaussian fits of the raw signal, demonstrating a good correspondence with the observed data. The Gaussian peaks, representative of maximal particle number density, diminish in height with increased axial distance, indicating a decrease in maximum local particle concentration. This phenomenon is attributed to the three-dimensional spreading of the jet, which naturally reduces the particle concentration within the laser sheet. Also, the Gaussian distribution widens along the test section's x-axis, illustrating the jet's mixing with the crossflow. This spreading of the distribution is a critical indicator of the jet's mixing efficiency; a wider spread denoting enhanced mixing.

The spread widths of micro low-density JICF are used to model the spatial mixing of JICF as a function of J. Full width at 10% of the Maximum (FW 10%M) of the Gaussian fit of the signal intensity is used to characterize the jet spread, offering a consistent measure for comparison across different conditions. Figure A.5 shows jet spread width along the centerline, for various momentum flux ratios J. As J increases, so does the spread width, with the broadest spread observed at J=100, reaching a maximum of 34.5 N/d at x/d=66. In contrast, the smallest jet spreads are associated with J=5 and J=10, highlighting the positive effect of momentum flux ratio on jet spreading. Notably, the rate of spread within the initial region from x/d=0 to x/d=10 is markedly steep, showing that the micro jets mix and diffuse rapidly with the crossflow. Beyond x/d=10, while the increase in spread continues, it does so with a lower gradient, indicating the persistence of mixing effects but at a reduced rate as the jet progresses downstream. These results align with the dual-zone near-field and far-field approach for scalar decay scaling presented by Smith and Mungal [39]. These authors observed dual trends in the reduction of jet concentration and momentum: the near-field decays at a higher rate, approximately $C^{-1.3}$, compared to the far field, which decays at $C^{-2/3}$. This transition zone is typically attributed to the point where the jet orientation shifts from predominantly vertical to more horizontal, transitioning from jet-like to wake-like mixing mechanisms [46].

Temporal Unmixedness

This section presents the unmixedness maps of the low-density micro JICF, shown in figure A.6 across different jet to crossflow momentum flux ratios J. Each map provides a quantitative visual representation of the temporal unmixedness, showing how the jet to crossflow momentum flux ratio influences the temporal mixing process. Darker regions of color gradation represent higher unmixedness, denoting lower temporal mixing efficiency and high particle number density variations in time. Lighter color areas indicate more homogeneous

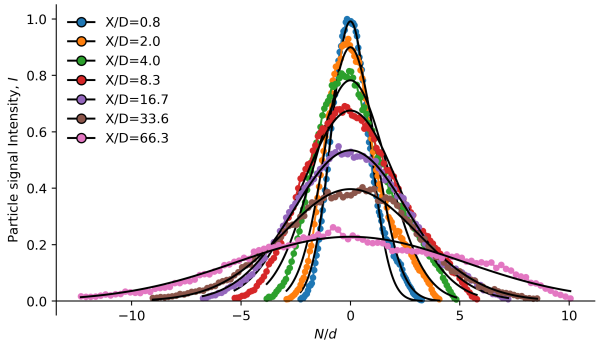

Figure A.4 Particle intensity and Gaussian fits evaluated on normal axes N/d, for $J = 80$.

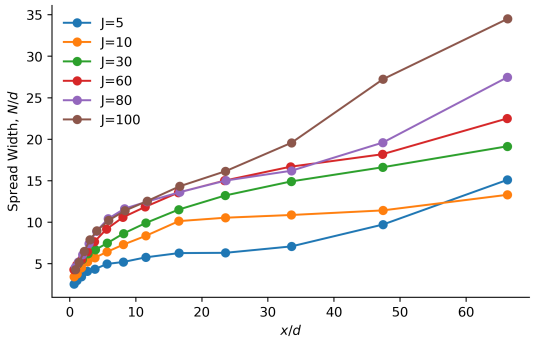

Figure A.5 JICF Spread along the centerline at different axial distance x/d and J

temporal mixing and low particle number density variations in time. Note that the regions that appear well-mixed very close to the bottom wall are due to a lack of laser illumination.

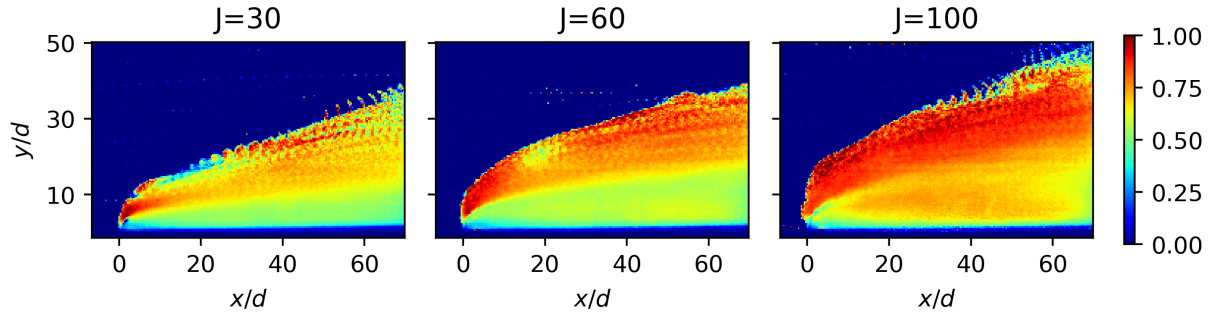

Figure A.6 Temporal unmixedness maps for a momentum flux ratio J equal to 30, 60, and 100

When following the unmixedness map along the jet centerline, values are seemingly constant at $U \approx 0.6$ in shades of green-yellow. This is likely caused by the definition of the unmixedness, where the denominator $\bar{I}(1-\bar{I})$ removes the effect of decreasing average particle signal along the x-axis. This leaves the effect of temporal fluctuations, showing that the least mixed areas are above the jet centerline for all values of J.

Notably, across all unmixedness maps of Figure A.6, the shear layer of the jet encountering the crossflow is the worst temporal mixing region. Local values of unmixedness in this region often reach unity. This is thought to be caused by jet instabilities and vortices roll-up. When observing the raw images over time, this shear layer region varies greatly in signal intensity. The jet shear layer line moves up and down due to global instabilities, and vortices are also shed along this upper delimitation. This causes areas along the shear layer to remain void

of particles for many frames, thus having a value of $\bar{I} = 0$, but after a momentary vortex or streamline deviates and enters these regions, the signal increases to a higher value near $\bar{I} = 1$. This flow unsteadiness causes the shear layer to have a high particle number standard deviation I' and a lower average signal intensity $\bar{I}$. This observation is even more visible for strong momentum flux ratios above $J = 30$, where the unmixedness of the shear layer is near unity and increases in value. In the case of higher J, the jet has more momentum to penetrate deeper, reaching higher turbulent crossflow velocities, causing an increase in temporal unmixedness.

APPENDIX B VORONOI CELL TESSELLATION OF SEEDED JETS IN CROSSFLOW

Voronoi Tessellation technique

An alternative Voronoi diagram technique was developed to quantify the mixing the DEHS seeded particles into the JICF. This technique was not used in the submitted works because of lengthy processing time and unresolved calibration procedures, but still represents interesting future research potential.

The voronoi cell diagram, or tessellation, is a method for partitioning a plane into regions surrounding each seed points. Each region, called a Voronoi cell, consists of all points closer to its seed point than to any other. This creates a tessellation where the edges of the cells are equidistant from neighboring points.

In the context of particle distributions, the inverse of the area of a Voronoi cell is proportional to the local particle concentration. This means that smaller cells correspond to higher concentrations of particles, as the density of particles in a region increases the number of seed points and reduces the size of the corresponding cells. Additionally, Voronoi diagrams can provide real-time analysis of particle concentrations, as the method directly relates the inverse of cell area to particle density.

Voronoi diagrams offer several benefits compared to the more complex Laser-Induced Fluorescence (LIF) concentration measurement technique. This simplicity reduces the need for specialized equipment associated with LIF, like molecular seeding and dye lasers. This technique was very recently used to infer the particle concentration in PIV seeded images [65]. It does not take account for molecular diffusion, which is a critical part of mixing for hydrogen fuel. This technique most likely undervalues the mixing occurring.

The python code used to calculate the Voronoi cells can be calibrated by generating multiple grid layers where the density of points increases from the top to the bottom, as shown in figure B.1. Each subsequent grid layer has a linear increase in the number of points along both the width and height of the grid. A Voronoi cell study case in visible in figure B.1, for perfectly spaced particles, and in figure B.2 for particles subject to molecular diffusion modeled by Brownian motion. The second case is what will be seen in a real particle laden low density gas flows. Brownian motion is modeled as a random walk where each point moves by a small, normally distributed random amount in both the x and y directions.

The concentration of points in this test case are still well detected even with randomness added. Table B.1 shows the parameter of the test case to compare it with the randomized case.

Table B.1 Voronoi tessellation Point Density and Total Points per Layer for calibration

Layer	**Density (points/unit area)**	**Total Points**	**Layer Area (units²)**
Layer 1	0.04	5	16.00
Layer 2	0.16	20	16.00
Layer 3	0.36	45	16.00
Layer 4	0.64	80	16.00
Layer 5	1.00	125	16.00

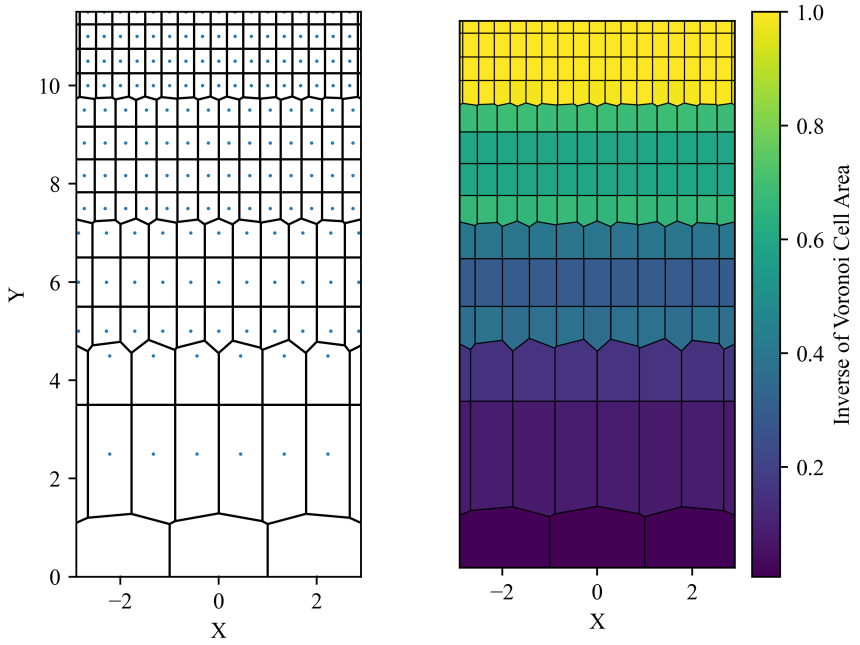

Figure B.1 Voronoi cell tessellation and corresponding particle number density colormap for a perfect particle grid

This technique can be used to evaluate the seeded particle number density from an illuminated JICF image. Results of the Voronoi tessellation are shown in figure B.3. The intricate system of cells and polygons is visible. When calculating the inverse area of each cell, the local particle concentration can be approximated. This method is displayed in figure B.4, where the jet exit shows increased concentration compared the downstream sections. The main drawbacks of this technique is the computational time needed for analysis of thousands of images, in the order of hours for each test recording of 1000 images each, when evaluated on an Intel i7-10510U CPU with 8 logical processors.

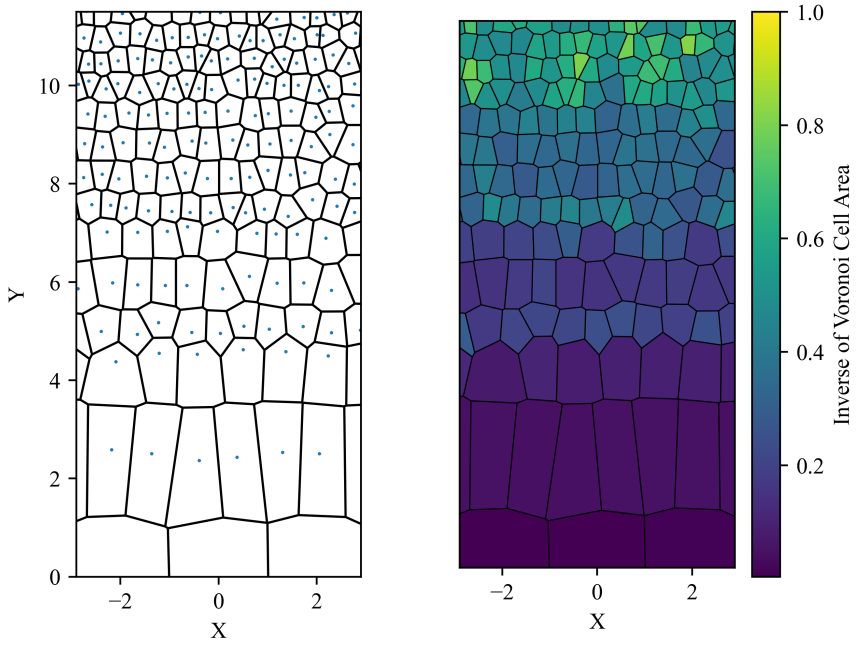

Figure B.2 Voronoi tessellation and corresponding particle number density colormap for particles affected by Brownian motion

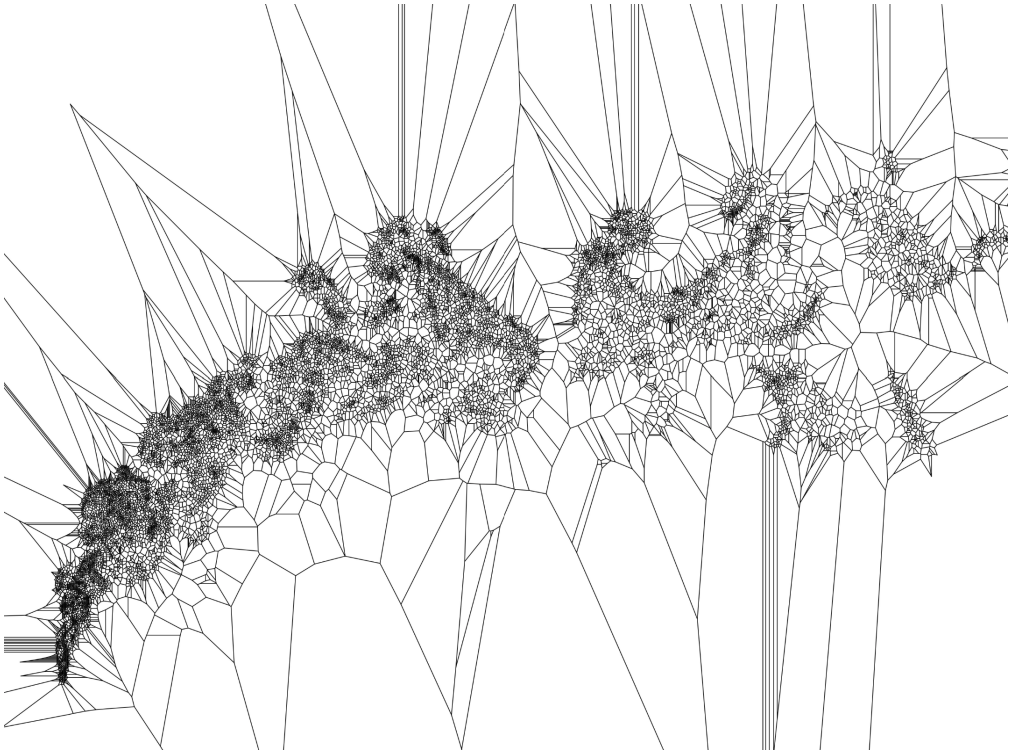

Figure B.3 Raw Voronoi tessellation from a JICF image

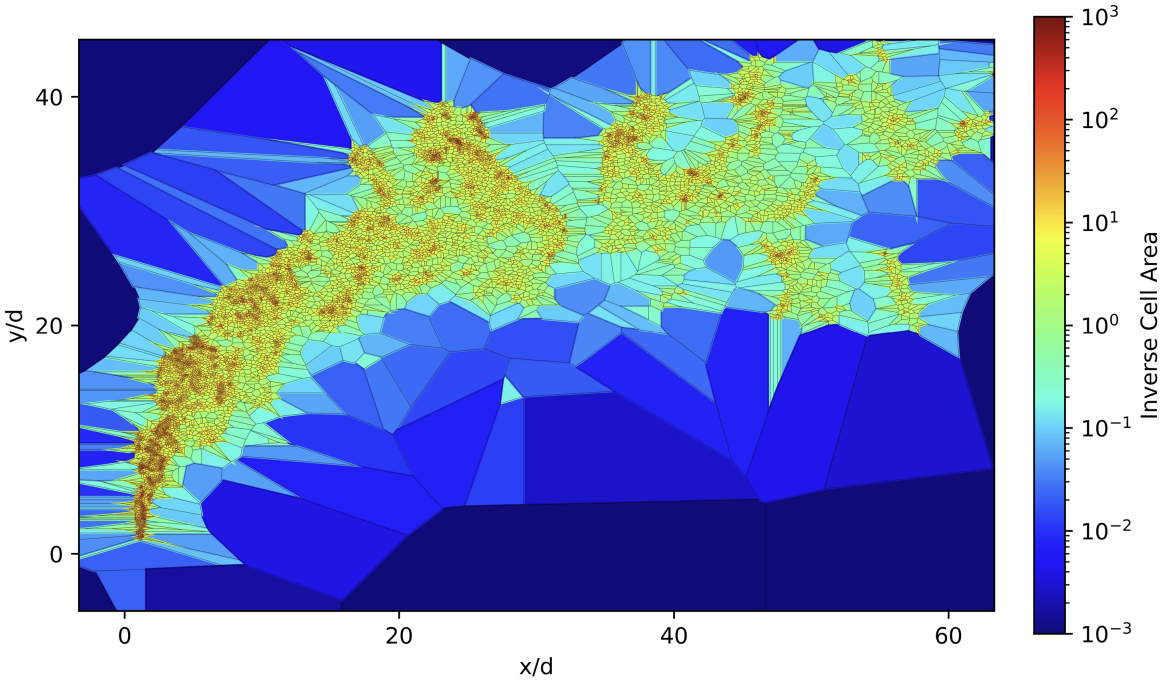

Figure B.4 Particle number density of a JICF evaluated with inverse cell area of a Voronoi tessellation